Pontifícia Universidade Católica
do Rio de Janeiro

Thais da Silva Rocha

SHORT- AND LONG-TERM PULLOUT BEHAVIOR OF MACRO SYNTHETIC FIBERS

Tese de Doutorado

Thesis presented to the Programa de Pós-Graduação em Engenharia Civil of PUC-Rio in partial fulfillment of the requirements for the degree of Doutor em Engenharia Civil.

Advisor: Prof. Daniel Carlos Taissum Cardoso
Co-advisor: Prof. Luís Antônio Guimarães Bitencourt Júnior

Rio de Janeiro
April 2024

Pontifícia Universidade Católica
do Rio de Janeiro

Thais da Silva Rocha

SHORT- AND LONG-TERM PULLOUT BEHAVIOR OF MACRO SYNTHETIC FIBERS

Thesis presented to the Programa de Pós-Graduação em Engenharia Civil of PUC-Rio in partial fulfillment of the requirements for the degree of Doutor em Engenharia Civil. Approved by the Examination Committee.

Prof. Daniel Carlos Taissum Cardoso
Advisor
Departamento de Engenharia Civil e Ambiental – PUC-Rio
Prof. Luís Antônio Guimarães Bitencourt Júnior
Co-advisor
Departamento de Engenharia de Estruturas e Geotécnica - USP
Prof. Pablo Augusto Krahl
Escola de Engenharia - Universidade Presbiteriana Mackenzie
Profª. Renata Monte
Departamento de Engenharia de Construção Civil - USP
Prof. Ricardo Pieralisi
Departamento de Construção Civil - UFPR
Prof. Dimas Alan Strauss Rambo
Universidade São Judas Tadeu

Rio de Janeiro, April 29, 2024

Thais da Silva Rocha

Graduated in Civil Engineering from the Universidade Estadual do Norte Fluminense Darcy Ribeiro (UENF) in 2014 and Master in Civil Engineering from the same institution in 2017. Research developed in the area of structures, with main areas of interest in: Concrete structures, cement-based composites and experimental research.

Bibliographic data

Rocha, Thais da Silva

Short- and long-term pullout behavior of macro synthetic fibers / Thais da Silva Rocha ; advisor: Daniel Carlos Taissum Cardoso ; co-advisor: Luís Antônio Guimarães Bitencourt Júnior. – 2024.
115 f. : il. color. ; 30 cm

Tese (doutorado)–Pontifícia Universidade Católica do Rio de Janeiro, Departamento de Engenharia Civil e Ambiental, 2024.
Inclui bibliografia

1. Engenharia Civil e Ambiental - Teses. 2. Arrancamento. 3. Fluência. 4. Macro fibras sintéticas. I. Cardoso, Daniel Carlos Taissum. II. Bitencourt Júnior, Luís Antônio Guimarães. III. Pontifícia Universidade Católica do Rio de Janeiro. Departamento de Engenharia Civil e Ambiental. IV. Título.

CDD: 624

Acknowledgment

To my husband Rafael, for being my safe haven and providing all the help I needed during all these years.

To my family, my mother Dulcélia, my father Gilberto and my sister Taiana, for all their encouragement and support.

To my advisor Daniel Carlos Taissum Cardoso, for teaching me so much, supporting me in moments of great uncertainty, encouraging me when I didn't believe I could do it, but mainly for being an example of a professional, professor and human being.

To my co-advisor Luís Antônio Guimarães Bitencourt Jr., for his kindness in pointing out all the improvements that could be made, for believing in me and always encouraging me.

To all the employees at the Structures and Materials laboratory at PUC-Rio, Rogério, Euclides, Jhansen, José and Marques, who never spared any effort to help me with whatever I needed.

To Jessé Beserra, for teaching me almost everything I know about 3D printing and being such a dear and encouraging friend.

To Vitor Monteiro, for helping with practically all the tests I did with great goodwill.

To Natália Victoria, who helped me with the most beautiful drawings for my thesis, taught me a lot about 3D printing, but mainly because she was always someone I could count on and a friend for life.

To Cássio Gaspar, for all the help and support in the creep tests.

To Janine and Elaine (UFF) for helping me with the microtomography tests, with a lot of patience and dedication.

To all my colleagues in the laboratory, who were always available to help.

To Rita and Luana, for their goodwill and dedication to helping me and all the students throughout the course.

To all the professors who provided me with nothing less than excellent teaching.

To Capes and PUC-Rio for the financial support, without which this research could not be carried out.

This study was financed in part by the Coordenação de Aperfeiçoamento de Pessoal de Nível Superior - Brasil (CAPES) - Finance Code 001.

Abstract

Rocha, Thais da Silva; Cardoso, Daniel Carlos Taissum (Advisor); Bitencourt Júnior, Luís Antônio Guimarães (Co-advisor). **Short- and long-term pullout behavior of macro synthetic fibers**. Rio de Janeiro, 2024. 144p. Tese de Doutorado – Departamento de Engenharia Civil e Ambiental, Pontifícia Universidade Católica do Rio de Janeiro.

The creep phenomenon in fiber-reinforced composites is particularly important when macro synthetic fibers are used, due to their low modulus of elasticity, exhibit pronounced viscoelastic behavior even at room temperature, which can lead to changes in the cracking control over time. Pullout tests are commonly used to predict fiber–matrix interactions and in this work were conducted for short- and long-term on three types of polymeric macro fibers. Different levels of long-term loads (20, 30, 40 and 50% of the maximum short-term pullout load) and fiber orientation angles (15°, 30°, and 45°) with respect to the direction of the load were considered to investigate the influence of these parameters on the interaction between macro synthetic fibers and matrix. Macro fibers with crimped surfaces and higher modulus of elasticity achieved higher bond stresses and lower creep deformations. In short-term tests, optical microscopy images were obtained on the pulled-out fibers to correlate the surface degradation of the fibers with the stress versus strain curves. In quasi-static pullout (short-term), small reductions in pullout strength were observed for all fibers and angles, in addition to an intensive degradation of their surfaces owing to the significant snubbing effect of this type of fiber. In contrast, for the long-term tests, a creep reduction was observed with increasing fiber inclination angle caused by the creep reduction of the fiber due to non-axial loading and additional force components produced by the deviation of the axial force. The Burgers viscoelastic model was applied and showed good agreement with the experimental creep curves, therefore consisting of a promising alternative for modeling the long-term behavior of individual fibers. Microtomography and scanning electron microscopy images showed that a large portion of the strain in tension, under sustained load, can be attributed to the creep of the fiber itself, thus making it challenging to estimate the

creep of this type of composite, given the considerable variability of fiber configurations.

Keywords

Pullout; creep; macro synthetic fibers.

Resumo

Rocha, Thais da Silva; Cardoso, Daniel Carlos Taissum (Orientador); Bitencourt Júnior, Luís Antônio Guimarães (Coorientador). **Comportamento de arrancamento em curta e longa duração de macro fibras sintéticas.** Rio de Janeiro, 2024. 144p. Tese de Doutorado – Departamento de Engenharia Civil e Ambiental, Pontifícia Universidade Católica do Rio de Janeiro.

O fenômeno de fluência em compósitos reforçados com fibras é particularmente importante quando são utilizadas macro fibras sintéticas, que devido ao seu baixo módulo de elasticidade, apresentam comportamento viscoelástico pronunciado mesmo em temperatura ambiente, o que pode levar a alterações no controle de fissuração ao longo do tempo. Testes de arrancamento são comumente usados para prever interações fibra-matriz e neste trabalho foram realizados para cargas de curto e longo prazo em três tipos de macro fibras sintéticas. Diferentes níveis de cargas de longo prazo (20, 30, 40 e 50% da carga máxima de arrancamento em curta duração) e ângulos de orientação das fibras (15°, 30° e 45°) em relação à direção da carga foram considerados para investigar a influência desses parâmetros na interação entre macro fibras sintéticas e matriz. Macro fibras com superfícies onduladas e maior módulo de elasticidade alcançaram maiores tensões de aderência e menores deformações por fluência. Em testes de curto prazo, imagens de microscopia óptica foram obtidas nas fibras arrancadas para correlacionar a degradação superficial das fibras com as curvas de tensão *versus* deformação. No arrancamento quase estático (curto prazo), foram observadas pequenas reduções na resistência ao arrancamento à medida que o ângulo foi aumentado para todas as fibras, além de uma intensa degradação de suas superfícies devido ao significativo efeito de polia. Em contraste, para os testes de longo prazo, foi observada uma redução da fluência com o aumento do ângulo de inclinação da fibra causada pela redução da fluência da fibra devido ao carregamento não axial e componentes de força adicionais produzidos pelo desvio da força axial. O modelo viscoelástico de Burgers foi aplicado e apresentou boa concordância com as curvas de fluência experimentais, consistindo, portanto, em uma alternativa promissora para modelar o comportamento de longo prazo de fibras

individuais. Imagens de microtomografia e microscopia eletrônica de varredura mostraram que uma parte da deformação em tração, sob carga sustentada, pode ser atribuída à fluência da própria fibra, tornando desafiador estimar a fluência deste tipo de compósito, dada a considerável variabilidade de configurações de fibra.

Palavras-chave

Arrancamento; fluência; macro fibras sintéticas.

Sumary

List of figures

List of tables

1. INTRODUCTION

1.1. Motivation

Fiber-reinforced concrete composites have diverse applications in civil engineering, with steel fibers and synthetic fibers being the two most commonly used types of fibers. It is known that steel fibers do not experience creep and can even restrict the deformation of concrete due to this property. On the other hand, when polymeric fibers are used, their long-term behavior must be taken into account as these materials are highly sensitive to creep, that is, they deform significantly under sustained loads and this can be a property that limits their use, as the widening of cracks in service of this type of composite becomes a concern.

Several studies have investigated the tensile [1–5] and flexural [5–13] behavior of these composites under sustained loads to clarify the phenomena associated with the increase in cracking over time; however, the mechanisms that occur at the fiber scale, such as pullout and stretching of the fiber itself, still need to be further investigated. Pullout tests are commonly used to study fiber-matrix interactions, as they can measure the force required to extract fibers from the matrix. But the response to pullout is influenced especially by the type of fiber, fiber orientation, matrix characteristics, among others.

Studies with pullout tests [5,7,14,15] were used to evaluate the behavior of the composite at the fiber level; however, several variables could interfere with the results obtained, especially the type and fiber orientation. More studies at the fiber scale with pullout tests are necessary as there is a wide variety of synthetic fibers available with different raw materials, geometry and surface corrugations, which influence their response to pullout, and although the behavior of plain concrete under sustained loading has already been investigated and can be predicted, creep deformations resulting from fiber-matrix interactions and the fiber itself can significantly affect the performance of this type of composite. Furthermore, studies have reported that the displacement obtained in the pullout tests of macro synthetic fibers under creep is basically due to the creep of the fiber itself [16–18].

In this way, this work seeks to investigate the complex mechanism during the short and long-term pullout of synthetic fibers aligned and not aligned with the

loading direction, contributing to a better comprehension of these cementitious composites.

1.2. Objectives

Investigate the mechanisms involved in short- and long-term pullout tests of macro synthetic fibers, with the main variables being the loading levels and the angle of inclination of the fibers, in order to contribute to a better understanding of the behavior at the fiber level. To achieve this, the following specific objectives are outlined:

- Investigate the short- and long-term pullout behavior of three different macro synthetic fibers aligned with the loading direction, understanding the mechanisms involved through X-ray microtomography (microCT) and scanning electron microscopy (SEM) and developing viscoelastic models.
- Investigate the influence of the fiber orientation on the short- and long-term pullout behavior of three different macro synthetic fibers, studying the mechanisms and developing models that account for the fiber orientation.
- Develop an analytical model to determinate the contributions of interface on the pullout response.

1.3. Work organization

This work is outlined in the form of five chapters, the last three of which refer to the contributions and objectives outlined. In Figure 1, a graphical abstract is shown with the main tests carried out in the final three chapters, in addition to the results found and the general outline of each of them. Descriptions of each of the chapters and their contributions are summarized below.

Chapter 1: *Introduction*

This chapter describes the motivation for carrying out the thesis, objectives and the organization of the chapters.

Chapter 2: *Literature Review*

This chapter presents a literature review on the main concepts covering the pullout behavior of fibers in cementitious composites, the angle effect of the fibers in the pullout response, the long-term pullout behavior of synthetic fibers and the viscoelastic rheological models that can be applied.

Chapter 3: *Macro Synthetic Fiber Pullout Behavior on Short- And Long-Term Tests*

This chapter presents pullout tests on macro synthetic fibers and discusses the pullout behavior based on X-ray microtomography and scanning electron microscope tests.

Chapter 4: *Influence of Fiber Orientation on The Behavior of Macro Synthetic Fiber in Short- And Long- Term Pullout Test*

This chapter presents pullout tests of macro synthetic fibers inclined in relation to the loading direction and discusses the influence of this inclination. Burger's viscoelastic model is applied to all experimental curves, and approximate equations for its parameters are presented.

Chapter 5: *Analytical Model for the Pullout Creep Behavior of Macro Synthetic Fibers*

This chapter presents short- and long-term tensile tests of the fibers evaluated. An analytical model is proposed to separate the contribution of fiber and interface to pullout with sustained load.

Chapter 6: *Conclusions and Suggestions for Future Works*

This chapter presents a general briefing on the issues discussed in the thesis and suggestions for future work.

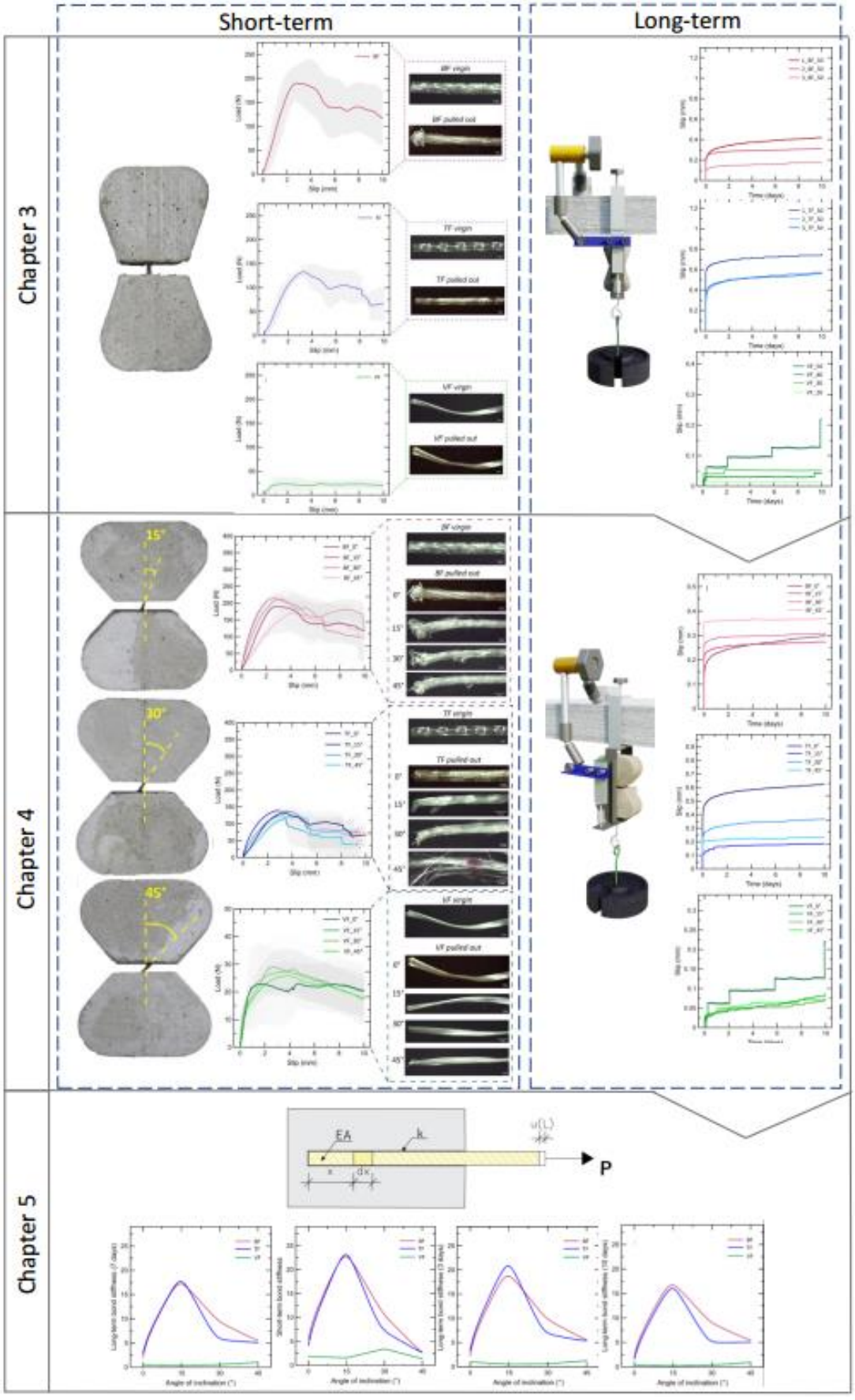

Figure 1. Graphical abstract of the thesis chapters.

2. LITERATURE REVIEW

2.1. Fiber-reinforced concrete composites

Fiber-reinforced composites are characterized by cementitious matrices reinforced with discontinuous, oriented, and randomly distributed fibers [19]. The fibers can act both in the interception of cracks to delay their propagation and prevent the coalescence of microcracks when added in adequate amounts. Yam and Mindess [20] pointed out that the reinforcement achieved by the insertion of fibers promotes the transfer of tension through the cracked sections, allowing the composite to retain some post-cracking resistance and resist deformations much greater than those resisted by the matrix. Therefore, the most significant contribution of fibers to cementitious matrices is to increase the energy absorption capacity [21].

Alwan *et al.* [22] stated that the energy absorption capacity or tenacity (represented by the area under the stress-strain curve) of a composite is due to the pulling out of fibers that connect one or more cracks and can be attributed to two mechanisms: the deformation of the material and the formation of new crack surfaces. The fibers that cross a crack can absorb energy, deform, and/or be pulled out depending on their adherence characteristics [22].

The properties of fiber-reinforced composites depend on both the cementitious matrix and the fibers, particularly the type, geometry, distribution, and volumetric percentage of the fibers, the adherence between the fiber and the matrix, and the mechanical characteristics of the fiber and matrix. Therefore, it is possible to control the mechanical properties of the composite by changing the proportions and characteristics of its constituents, mainly the fibers [19].

2.2. Pullout behavior

In fiber-reinforced composites, tensile forces are resisted by the fibers and the matrix, and the strength portions corresponding to each component are influenced by the transfer capacity across the fiber-matrix interface. Pullout tests are commonly used to investigate fiber-matrix interactions because they measure the force required to extract a fiber embedded in a matrix.

There are three particularly important types of fiber-matrix interactions: (i) adhesion (or elastic adhesion) at the fiber-matrix interface, (ii) friction (or frictional

or frictional adhesion) that allows relative slips along the fiber-matrix interface, and (iii) mechanical interactions (resulting from a specific fiber geometry that creates localized load transfer points between the fiber and matrix) [23,24]. Banthia and Trottier [25] argued that the contribution of adhesion is very small, with failure occurring at the beginning of the pullout and slip resistance mainly guaranteed by friction, which adjusts to the anchoring process still under development.

The stress transfer mechanisms in fiber-reinforced composites are directly related to these interactions and must be considered in pre- and post-cracking stages. Bentur and Mindess [24] reported that, in the pre-cracking phase, before cracking occurs, the predominant stress transfer mechanism is elastic, and the longitudinal displacements of the fiber and matrix at the interface are geometrically compatible. The authors reported the occurrence of shear stresses at the fiber-matrix interface that distributed the external load between these two components such that the interface stress was only one, although the stresses in each material were different. This elastic shear transfer (non-uniform along the fiber/matrix interface) is the main mechanism for predicting the proportional limit and first crack stress. In the postcracking stage, the stress-transfer mechanisms are essentially the same as those presented for an uncracked composite: elastic adhesion (or adhesion), mechanical adhesion, and sliding owing to friction.

To understand how the interactions between the fiber and matrix promote gains in the energy absorption capacity compared with conventional concrete, it is necessary to understand the stress transfer mechanisms acting at the fiber level. A typical pullout curve for a single straight steel fiber oriented parallel to the load direction is shown in Figure 2. Two stages can be distinguished during the extraction process: the loss of adhesion and slippage [26]. The resistance mechanism in the ascending AO stretch is the elastic adherence or adhesion. At point A, gradual debonding of the fiber begins (loss of adhesion with the matrix), and the stress transfer across the detached interface gradually becomes frictional, with relative displacements between the fiber and the matrix [24]. After reaching the peak load for very low displacements, an abrupt load drop can be observed, which is the milestone for the second pullout stage. Detachment begins when the elastic shear stress at the interface exceeds the shear strength of the matrix and progresses to complete detachment at point B [24]. The fiber is plucked into the B-C interval, and the only resistance is offered by friction. With fiber sliding, friction is reduced owing to the progressive loss of length at the fiber-matrix interface and the wear and compaction of the matrix around the fiber [26]. The pullout energy

increases with increasing fiber embedding length; if the length is too long, the fiber breaks instead of being pulled out.

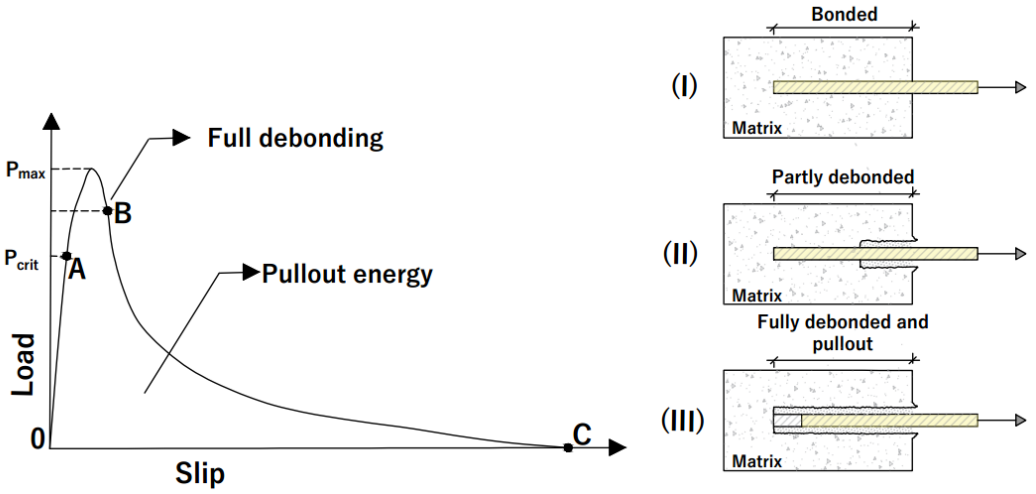

Figure 2. Load *versus* displacement curve typical of a single straight steel fiber pullout (Adapted from ALWAN *et al.* [22] and DENG *et al.* [27]).

In general, fiber failure occurs mainly due to surface wear. In the case of fibers with a modified geometry (deformed fibers), there is a great dissipation of energy due to alignment and plastic deformation during pullout. Although the deformations caused in the fibers along their lengths are necessary to increase their resistance to pullout, they are only effective when a complete pullout occurs [28]. The possible failure modes are complete fiber pullout, matrix fracture, fiber separation/detachment, and fiber fracture. According to Banthia [28], among the failure possibilities, the one that generally causes the greatest reduction in terms of pullout energy is fiber fracture. Regardless of whether the fiber is straight or deformed, sliding is the failure mode that leads to the greater energy absorption capacity, followed by a complete fiber pullout. According to Isla *et al.* [29], when the fibers fracture outside the cementitious matrix or at the beginning of the incorporated part of the fiber, the failure can be considered total because the pullout stress can no longer be transferred to the matrix. If the fracture occurs in the part still embedded, the failure is considered partial because, although part of the embedded length has been lost, the remaining portion continues to transfer load to the matrix. The deformation and conformation of the fibers during pulling directly contributed to the total deformation of the composite [22].

The predominant mechanisms depend on the properties of the fiber and matrix. Bentur and Mindess [24] stated that, if the tensile strength of the matrix is high, interface separation can occur before matrix cracking; otherwise, cracking

may precede fiber detachment. When the adhesion is very low, the dominant mechanism is friction, because the energy that causes fiber detachment is practically negligible.

The pullout curves are influenced by several characteristics of the fibers and matrix. In the case of the pullout of a single fiber, factors such as fiber geometry, angle of inclination in relation to the loading direction, and matrix characteristics can change the previously described behavior, which is valid for a single straight fiber oriented parallel to the direction of loading. According to Bentur *et al.* [30], fibers with changes in their geometry have a pullout response different from that of smooth fibers and cannot be described by the same models; the flow mechanisms and stress distribution along the fiber must be considered simultaneously to determine the failure mode and general pullout behavior. Although it is a relatively easy test to perform and requires important information to be extracted, many variables must be considered when comparing these data with the composite real behavior.

2.3. Influence of fiber orientation on pullout

The orientation of the fibers within a cementitious matrix is essential for determining the overall efficiency of the composite because it influences the strength and pullout energy. In real composites, the distribution and orientation of the fibers are generally random in relation to the possible crack planes. This distribution is mainly influenced by the casting technique, location within concrete member, element geometry, and use of vibrators. Fibers often assume angles other than 90° relative to the cracked surface. When this occurs, effects are triggered that can either increase or reduce the strength of the composite.

Ding *et al.* [31] stated that if fibers are inserted to form bridges between cracks, the bridging efficiency can be maximized when the fibers are perpendicular to the plane of the crack. An increase in the orientation angle causes a reduction in the efficiency and, consequently, a reduction in the pull-out resistance. However, Lee *et al.* [32] and Cao and Yu [33] stated that the effect of the fiber inclination angle on the load and pullout energy depends considerably on the proportion, geometry, and properties of the fibers, including whether the fiber material is metallic or synthetic.

When the fiber is inclined in relation to the fracture plane, it is necessary to consider fiber bending due to local geometric restrictions [30], as shown in Figure

3. Bentur *et al.* [30] claimed that a complex state of stress is formed in the fiber and matrix due to local bending and that the general behavior depends on the stiffness of both. Bentur *et al.* [30] explained that, if the fiber is ductile and has a low modulus, it will easily bend, inducing dowel action, which can lead to an increase in pullout resistance, compensating for the reduced efficiency associated to the fiber inclination. However, if the fiber is brittle and has a high modulus of elasticity, local bending may occur, which, superimposed on axial tensile stress, may lead to premature failure of the fiber.

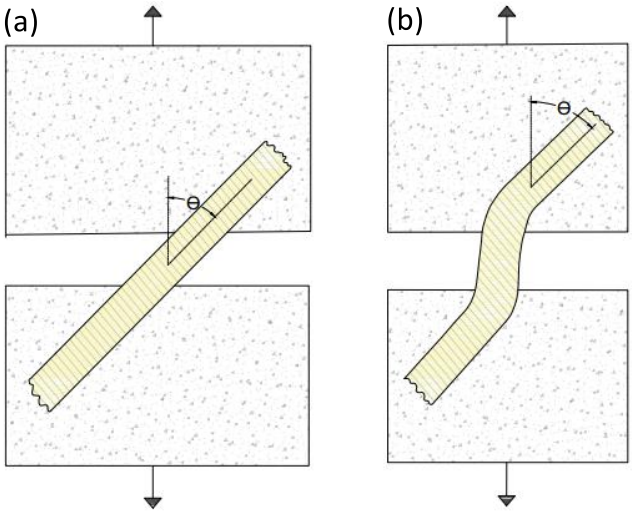

Figure 3. Pullout of a fiber at an angle θ from the direction of loading: (a) fiber before deformation; (b) inclined fiber being pulled out and undergoing local bending (Adapted from BENTUR AND MINDESS [24]).

The fiber slope influences the pullout performance owing to matrix fragmentation and the snubbing effect. According to Tai and El-Tawil [34], as soon as a pullout load is applied, the fibers tend to separate from the matrix, the adhesion is lost, and the fibers begin to slip. At that instant, the frictional resistance mechanism is mobilized, and an upward pressure is induced in the matrix around the exit point, locally increasing the frictional resistance (snubbing effect). Depending on the tensile strength of the matrix, load rate, and fiber geometry, increasing the pressure in the matrix can cause localized damage and local fragmentation at the exit point, as shown in Figure 4. The damage zone forces the fiber to move through the radius of curvature, causing permanent plastic deformation of the fiber. As the fiber is pulled out completely, permanent deformations force the originally straight fiber to assume a different shape. In general, the probability of fiber breakage increases with the inclination angle.

According to Lee *et al.* [32], as the fiber orientation angle increases, the fragmentation length of the matrix increases because a larger portion of the matrix is crushed, resulting in a decrease in the pullout load and an increase in the crack opening.

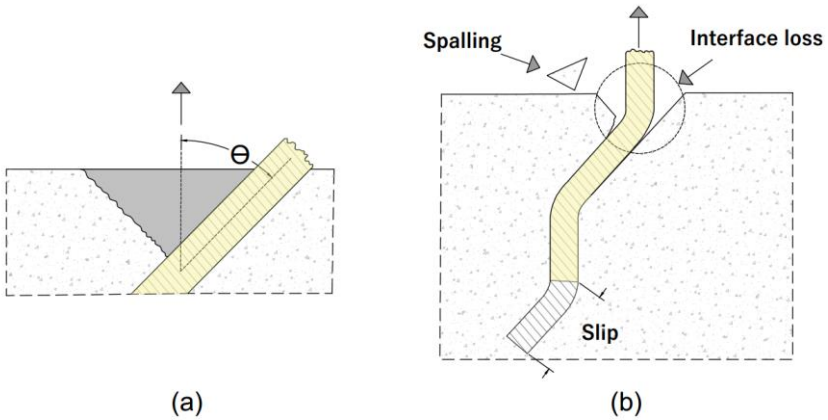

Figure 4. Inclined fiber suffering the effects of fragmentation: (a) before matrix fragmentation; (b) after matrix fragmentation (Adapted from ISLA *et al.* [29]).

Tai and El-Tawil [34] stated that matrix failure at the fiber exit point limits the ability of the fiber to transmit loads to the matrix. This behavior is accentuated in the case of twisted fibers, possibly because of their particular structure, which induces higher localized stresses. In the case of inclined fibers that fail outside the matrix, the load-transfer capacity is abruptly lost, resulting in total failure [29]. Tai and El-Tawil [34] observed that the rupture of inclined fibers occurred more frequently in the case of fibers with hooks at the ends and twisted at large angles of inclination and/or high load rates.

During pullout, bent fibers behaved differently from aligned fibers, especially those with a deformed geometry. This difference is mainly due to the failure of the surrounding matrix, which allows fiber rotation and further displacement without slipping, in addition to reducing the embedded length. This shows that the performance of fibers in fiber-reinforced cementitious composites cannot be evaluated solely based on the aligned fiber results, and the effects of cement damping and matrix fragmentation that occur for inclined fibers must be considered when modeling the pullout behavior of the composite.

2.4. Creep pullout behavior

Fiber-reinforced cementitious composites can be applied as structural members, flooring materials, or tunnel linings. In all cases, they are usually

subjected to sustained static mechanical loads in service and may experience a deformation called creep, which can be permanent and time-dependent deformation when subjected to a constant load or tension [35]. This deformation is observed in several materials, especially polymers, and can affect their applications because of the reduction in their service life.

In the case of composites reinforced with steel fibers, creep does not appear to be a problem [7,36] and may even restrict this deformation [36]. However, when synthetic polymeric macro fibers are used, creep deformation may play an important role in the opening of cracks over time. The mechanisms involved in the opening of creep cracks are not yet fully understood; although few studies have been conducted at the fiber level using pullout tests for macro synthetic fibers fibers [1,7,14,37,38], much still needs to be studied owing to the great sensitivity of the tests and lack of standardization.

Vridaghs *et al.* [15] presented the results of 15 pullout tests under sustained load on two types of synthetic polypropylene macro fibers (embossed type) with different loading levels (25, 40, 50, 60%, and 75%) and with 15 mm of embedding to evaluate the behavior at the fiber level over time (Figure 5). They reported that the behavior was strongly dependent on the charging rate, with heavier loads decreasing the time to failure (complete startup).

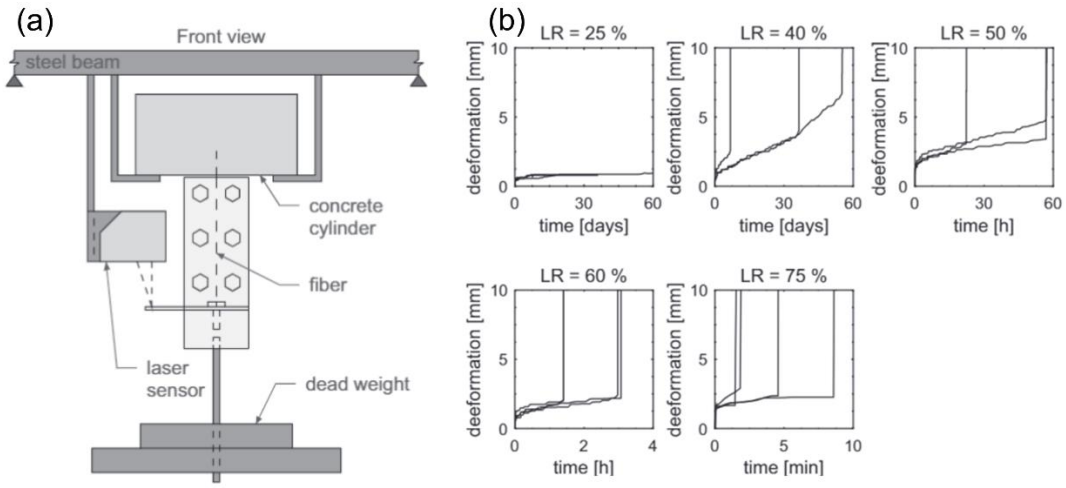

Figure 5. (a) Pullout test setup [15]; (b) pull-out creep results for 5 different considered load ratios for samples with embedding length 15 mm and θ = 0° [15]. Note the different time scales.

Babafemi *et al*. [14,38] performed creep pullout tests on three types of macro synthetic fibers – two embossed and one crimped – varying in length between 48 and 54 cm (Figure 6). Fifty percent of the short-term pullout load was used in the

tests for 30 days, with a fixed embedment length of 20 mm in the three fibers. They reported that the time-dependent pullout response could be influenced by the fiber type, especially the type of surface corrugation, with the embossed fibers showing better performance, reaching the test time limit without being pulled out, whereas the crimped fiber was completely ripped out at 22 days. Microtomography images suggested that the instantaneous deformation measured shortly after applying the creep load was purely due to the stretching of the free section and along a detached section. Isolated fiber elongation has been reported to be more prominent than creep pull-out.

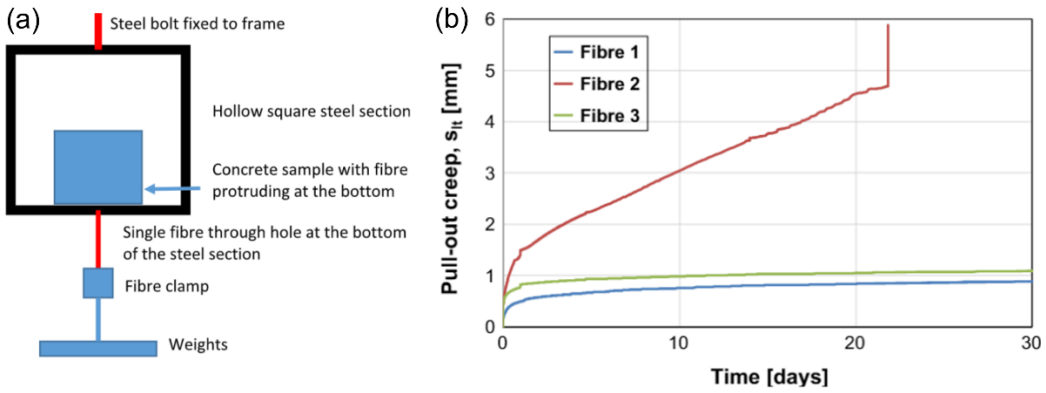

Figure 6. (a) Pullout test setup [14,38]; (b) pull-out creep response of macro synthetic fibers under sustained loadings [14,38].

Lima *et al.* [7] conducted pullout tests on two types of fibers: a smooth polypropylene fiber with a deformed geometry measuring 40 mm in length and a 35 mm steel fiber with a hook (Figure 7). The embedded length of the polypropylene fibers was 10 mm, whereas that of the steel fibers was 9 mm. The tests were conducted for 7 days at load levels of 50 and 75% of the maximum short-term pullout load. They reported that the mechanisms involved in the pullout process of polypropylene fibers played a primary role in creep deformation, whereas steel fibers did not exhibit significant creep deformations in an environment with controlled temperature and humidity. Furthermore, they reported that the smooth nature and low modulus of elasticity of the fibers imply less adhesion to the matrix, which makes them more susceptible to creep deformations, especially at higher loads, such as 75%, reaching the tertiary creep stage (complete pull-out).

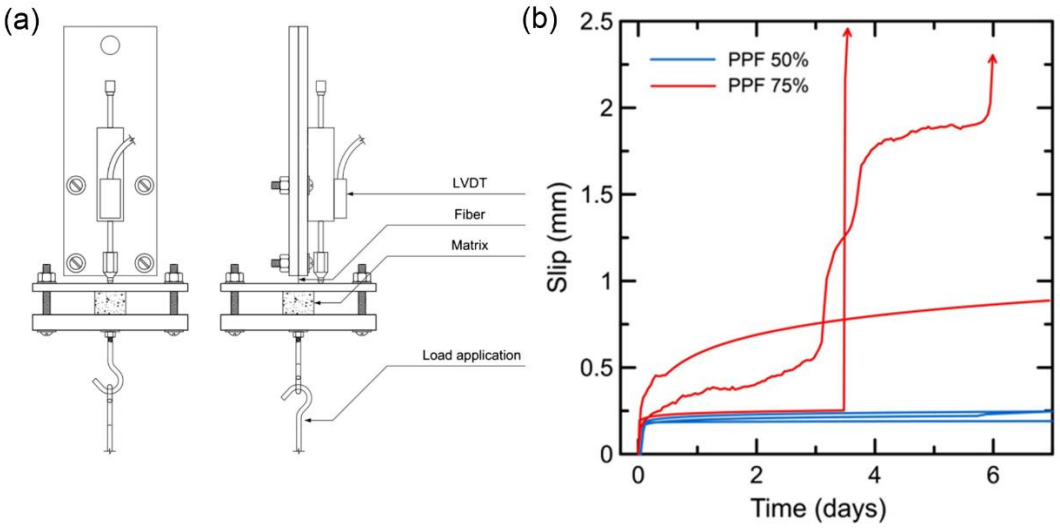

Figure 7. (a) Pullout test setup [7]; (b) results from pullout creep tests [7].

Few studies have reported the long-term behavior at the fiber level in pullout tests. Furthermore, other variables, such as the angle of inclination in relation to the loading direction, must be considered. As there are many types of synthetic fibers in the market, establishing standards for their responses is a goal that will only be completed with extensive research.

2.5. Rheological Burgers model

The creep behavior of the material under environmental conditions depends mainly on the applied stress levels and time [39]. The typical creep curve, i.e., strain *versus* time, is divided into three stages: (I) stage transient (primary), where the strain rate (or creep rate) decreases with time and corresponds to the slope of the curve, occurs in a relatively short period at the beginning of the test (after loading) and progressively decreases until reaching the next stage [40]; (II) steady state (secondary) of longer duration, interrupted by the beginning of the tertiary stage; (III) tertiary state, the deformation increases continuously until the material ruptures [41]. The tertiary creep phase is never reached during the lifetime of the structure [41]. The typical creep curve is shown in the Figure 8.

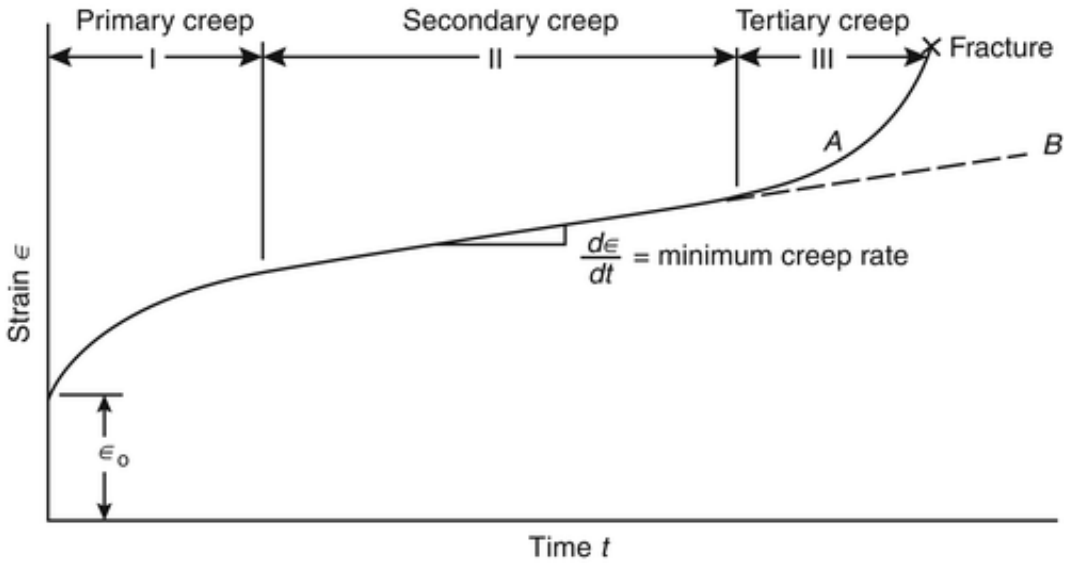

Figure 8. Creep stages [42].

The total deformation at time *t* is therefore composed of an instantaneous elastic deformation and a creep deformation [41]. Creep models that approximate time-dependent behavior from a combination of elastic springs and viscous components (dashpots) are called rheological models. In these models, the elastic element, described as a spring, represents a perfect elastic body obeying Hooke's law (ideal solid) [43], that is, stress is proportional to strain. The viscous element, described as a dashpot, represents a perfectly viscous body obeying Newton's law (perfect liquid) [43], that is, the force is proportional to the strain rate. The Figure 9 shows the representation of these elements.

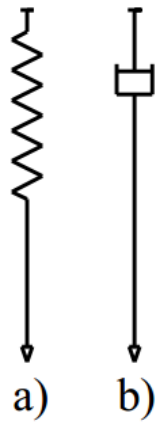

Figure 9. The representations of the basic mechanical models: a) spring for Hooke and b) dashpot for Newton [43].

When tertiary creep is not analyzed, Burgers 4-parameter rheological model can be used to simulate the creep behavior of polymeric materials and their composites [44,45]. In this model, the constitutive equations can be derived by considering the strain response under constant stress of a spring, a dashpot, and a Kelvin unit connected in series [39,41], as shown in Figure 10. The Burgers creep model is composed of the Maxwell model and the Kelvin-Voigt model in series, where the Kelvin model is adopted to describe the transient stage (i.e., the primary creep), while the Maxwell model is mainly to describe the instantaneous deformation and the secondary creep stage [46]. Then, the total deformation at time *t*, noted $\varepsilon(t)$, is equal to the sum of the deformations for these three elements:

$$\varepsilon(t) = \varepsilon_1 + \varepsilon_2(t) + \varepsilon_3(t) \tag{1}$$

where

$$\varepsilon_1 = \frac{\sigma_0}{E_1} \tag{2}$$

$$\varepsilon_2(t) = \frac{\sigma_0}{E_2}\left[1 - exp\left(\frac{-E_2}{\eta_2}t\right)\right] \tag{3}$$

$$\varepsilon_3(t) = \frac{\sigma_0}{\eta_1}t \tag{4}$$

where σ_0 is the constant applied stress, E_1 (or R_1) and E_2(or R_2) are the modulus of elasticity of the springs, and η_1 and η_2 are viscosities of the dashpots in this model. Equation (2) results from the Hooke's law, ε_1, $\varepsilon_2(t)$, and $\varepsilon_3(t)$ represent, respectively, the elastic strain of the Maxwell spring, the delayed elastic strain of the Kelvin unit, and the viscous strain of the Maxwell dashpot [41]. Thus, the total strain can be expressed as follows:

$$\varepsilon(t) = \sigma_0\left[\frac{1}{E_1} + \frac{t}{\eta_1} + \frac{1}{E_2}\left(1 - exp\left(\frac{-E_2}{\eta_2}t\right)\right)\right] \tag{5}$$

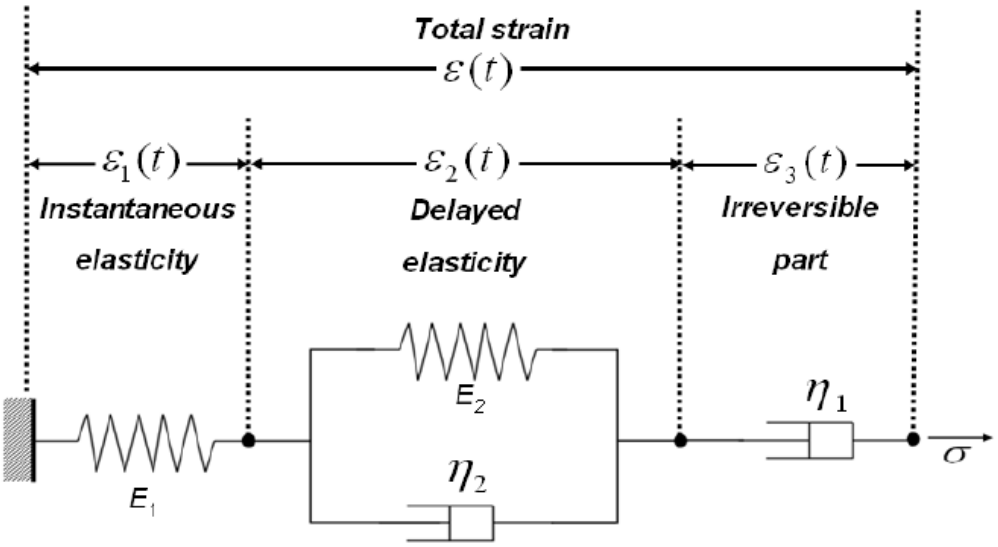

Figure 10. Schematic description of Burger's rheological model [41].

The parameters of the Burgers model can be obtained from experimental curves of deformation *versus* time, as described in Figure 11. This is generally done by applying curve fitting techniques to all available experimental results to obtain different sets of model parameters [46], and these can be used to describe creep behavior. Good fits can be found between experimental results and model formulations; however, the established model cannot be used for conditions different from those tested [46].

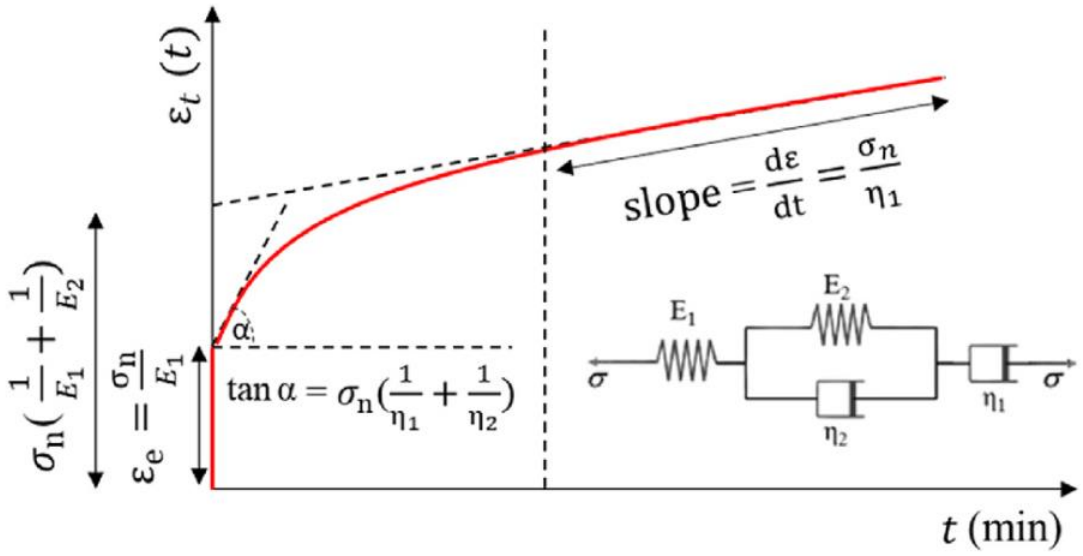

Figure 11. Burgers model parameters from the curve features and rheological representation [39].

3. MACRO SYNTHETIC FIBER PULLOUT BEHAVIOR ON SHORT- AND LONG- TERM TESTS

This chapter was published under the reference:

T. da S. Rocha, D.C.T. Cardoso, L.A.G. Bitencourt, Macro synthetic fiber pullout behavior in short- and long-term tests, Constr Build Mater. 384 (2023). https://doi.org/10.1016/j.conbuildmat.2023.131491.

3.1. Introduction

In fiber-reinforced concrete (FRC), toughness increases with fiber pullout because fibers absorb energy as they are deformed or pulled out, depending on their bond characteristics [22]. Given that structural applications of FRC are subject to sustained loading over time, the study of the creep effect becomes quite relevant, especially when using macro synthetic fibers, because polymers are particularly sensitive to creep, which is generally an undesirable phenomenon that may limit the material's use [35].

Researches have been conducted on cement-based composites reinforced with macro synthetic fibers to assess compressive [7,36,47–49], tensile [1–4,37,38,50], and flexural [6–12]strengths under sustained loading. Some studies have already assessed pullout mechanisms under sustained loading [7,14,36–38]. It has been reported that polymer FRC cracking mechanisms account for slowly deforming stretches of fibers and their interfaces [3,15], indicating that fiber creep is the determining factor in pullout under sustained loading [14].

Polymer fibers undergo significant elongation before controlling crack propagation [9,10]. This shortens their transverse section owing to the Poisson effect. As shown by Babafemi and Boshoff [3], the load transfer between the fiber and matrix when the matrix is cracked depends on the frictional bond and mechanical interlock between the fiber and matrix. The frictional bond may weaken when the fiber contracts laterally, resulting in partial fiber pullout. This process will continue until debonding stabilizes or the fiber pulls out completely. The pullout process is intensified by fiber deformation and the resulting loss of friction resistance in slip [7].

Fibers with a modulus of elasticity higher than plain concrete (such as steel fibers) restrict concrete creep deformation. In contrast, fibers with a modulus of

elasticity lower than that of plain concrete (such as polymer fibers) may increase [36] or only slightly restrict (2%) [12] this deformation. Zhao *et al.* [36] concluded that fibers with a low modulus of elasticity could only dissipate energy and increase the ductility of concrete when the expansion of concrete cracks is relatively large (owing to their high deformation performance), albeit without improving the long-term deformation of concrete under a low-stress level. Because stresses are transferred from concrete to fibers only after the formation of cracks, the percentage of post-cracking resistance under loading that can be sustained over time remains unknown [3].

FRCs with macro polymer fibers have been increasingly used, thus requiring research on their performance over time. The behavior of plain concrete under sustained loading has already been investigated and can be predicted, but creep deformations resulting from fiber-matrix interactions and the fiber itself may significantly affect the material performance. Although a few studies on fiber-matrix interactions have already been published, there needs to be guidelines and/or protocols for regulating the design of these composites for sustained loading. In addition, polymeric fibers produced from different raw materials and with varied geometric configurations and surface corrugations are available on the market. The complexity in simulating the behavior of these composites under sustained loading is explained by difficulties in separating fiber creep from interface creep because each type of fiber has distinct characteristics. Therefore, a comprehensive study should be conducted to predict the typical creep behavior of polymer FRCs.

In this study, three different macro synthetic fibers were investigated to identify the characteristics that stand out in their performance. For this purpose, quasi-static pullout tests under 20, 30, 40, and 50% sustained loading were performed. This range of loading percentages was selected to represent the different service conditions. Furthermore, to confirm the responses to mechanical tests, imaging tests such as X-ray microtomography and scanning electron microscopy were also performed on some of the samples tested under sustained loading to help clarify some of the mechanisms involved in the long-term pullout.

3.2. Material and methods

3.2.1. Materials and concrete mix

The dosage used in this study was the same as that reported by Souza *et al*. [51], who produced polyvinyl alcohol (PVA) fiber reinforced concretes and studied their behavior for applications to industrial concrete flooring. The composition, alongside the dosage, is outlined in Table 1. The matrix was produced using Portland CPV ARI PLUS cement manufactured by Lafarge Holcim (equivalent to ASTM Cement type III). The water/cement factor used in all mixtures was 0.42, with a minimum cement content of 380 kg/m³. The superplasticizer chemical additive ADVA® 753, produced by GCP Applied Technologies, was used to ensure workability. Gravel 0, with 12.5-mm maximum particle size and gravel 1, with 19-mm maximum particle size were the coarse aggregates used in this study. Natural quartz sand with 2.40-mm maximum particle size and 2.58-fineness modulus determined according to the Brazilian National Standard NBR 17054 [52] (equivalent to ASTM C136-01[53]) was used as fine aggregates.

Table 1. Mixture proportions.

Material type	*Volume (kg/m³)*
Cement (CPV ARI)	380
Quartz sand	811
Coarse aggregate (maximum diameter of 12.5 mm)	250
Coarse aggregate (maximum diameter of 19 mm)	650
Water	160
Superplasticizer	3.80

The mixing procedure was previously described by Souza *et al.* [51]; fine aggregates, gravel 0 and gravel 1 were added (dry and in this order) to a concrete mixer along with 70% water. After 60 seconds of mixing, cement was added and mixed for another interval of 60 seconds. Subsequently, the remaining volume of water (30%) was added and mixed again for 60 seconds. In the final step, the superplasticizer was added and then mixed for 5 minutes. Because all tests were performed for a single fiber, no more fibers were added to the concrete. The slump-flow test was performed to assess the workability and flowability of the fiber-free

matrix. The test followed the criteria specified by NBR 16889 [54] (equivalent to ASTM C143/C143M-12 [55]) and indicated a slump of approximately 60 mm.

The matrix was characterized using 100-mm-wide and 200-mm-long cylindrical concrete specimens, which were cast in a mold and kept in a wet chamber for 28 days after demolding to assess the compressive strength (NBR 7215 [56], equivalent to ASTM C39/C39M-01 [55]) and to determine the initial tangent modulus of elasticity (NBR 8522-1 [57], equivalent to BS EN 12390-13 [58]). The tests were performed at a rate of 0.35 MPa/s on a Controls MCC8 servo-controlled testing machine with 2000-kN loading capacity. The axial compressive strength of four matrix samples at 28 days was 47.32 ± 6.24 MPa. The modulus of elasticity of the 4 samples was 27.98 ± 1.97 GPa. The evaluated matrix properties are summarized in Table 2.

Table 2. Matrix properties.

Properties	*Value*
Axial compressive strength (MPa)	47.32 ± 6.24
Modulus of elasticity (GPa)	27.98 ± 1.97
Slump (mm)	60

3.2.2. Macro synthetic fibers

Three macro synthetic fibers were used in this study, namely Barchip54, manufactured by Elasto Plastic Concrete®, TamFib SP54, manufactured by Normet®, and Tuf-Strand-SF, manufactured by Viapol®. According to the manufacturers' datasheets, the fibers and their main characteristics are shown in Figure 12 and outlined in Table 3. The following nomenclature will be used for these fibers: *BF* for Barchip54, *TF* for TamFib SP54, and *VF* for Tuf-Strand-SF fibers.

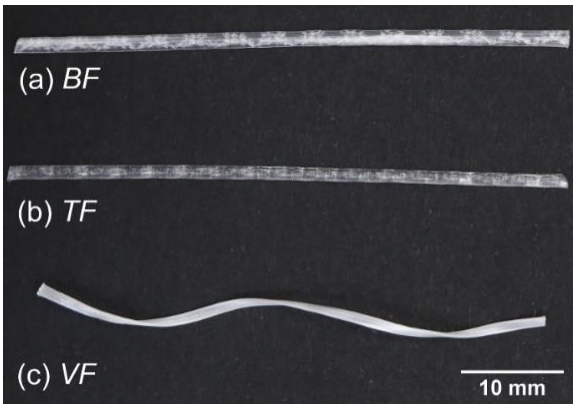

Figure 12. Macro synthetic fibers.

BF and *TF* fibers have the same length, straight geometry, and anchoring provided by the relief of the surface. Conversely, *VF* fibers are slightly shorter and have a twisted geometry and smooth surface consisting of three wires bundled together. To identify the geometric characteristics of the fibers, the equivalent diameter and the aspect ratio were determined by measuring the cross-sectional areas of 10 samples of each type of fiber from images acquired using an optical microscope and the software FIJI [59]. Because none of the fibers had a circular cross-section, their mean equivalent diameters were determined from the diameter of a circle with the same area as their cross-section. The aspect ratio was calculated by dividing the length by the equivalent diameter of each fiber. Figure 13 shows cross-sections of each fiber.

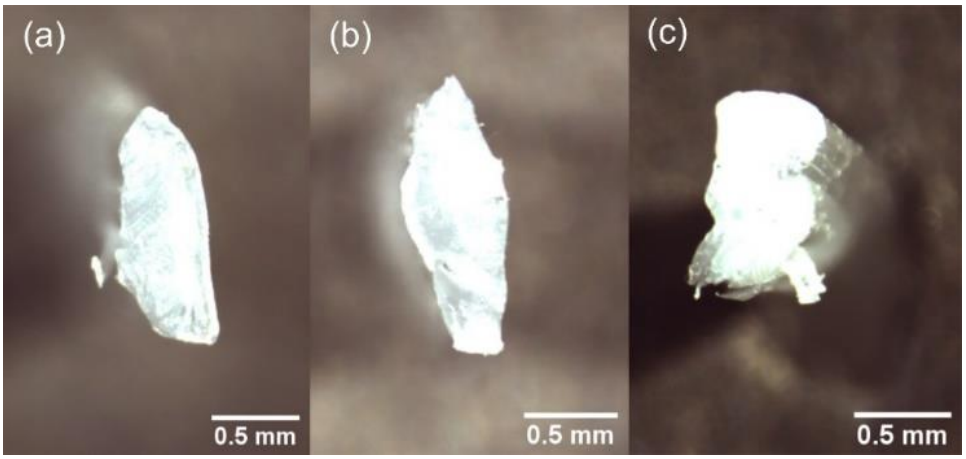

Figure 13. Cross section of the fibers: (a) *BF*; (b) *TF*; (c) *VF*.

Table 3. Properties of the fibers.

Properties	*BF*	*TF*	*VF*
Fiber type	*Barchip54*	*TamFib SP54*	*Tuf-Strand-SF*
Manufacturer	*Elasto Plastic Concrete®*	*Normet®*	*Viapol®*
Fiber material [a]	*Virgin polypropylene*	*Polyolefin*	*Polyethylene/ Polypropylene*
Fiber length (mm) [a]	*54*	*54*	*51*
Equivalent diameter (mm)	*0.862 ± 0.022*	*0.809 ± 0.043*	*0.797 ± 0.047*
Aspect ratio (l_f/d)	*62.7 ± 1.6*	*66.9 ± 3.4*	*64.2 ± 3.8*
Specific gravity (g/cm³) [a]	*0.90*	*0.91*	*0.92*
Tensile strength (MPa) [a]	*640*	*540*	*600-650*
Modulus of elasticity (GPa) [a]	*12*	10.4	*9.5*
Cross-section	*Irregular*	*Irregular*	*Irregular*
Fiber shape	*Embossed surface*	*Embossed surface*	*Twisted*

[a] *information provided by the manufacturer* [60–62].

3.2.3. Preparation of pullout samples

The specimens were cast in a mold manufactured using a 3D printer to optimize their geometry for fiber placement and leak-free closure. The 3D-printed mold is shown in Figure 14 (a) and consists of two symmetrical sides and a latch that seals the fiber vertically and laterally. In addition, because the cast was 3D printed, a hole with a diameter very close to the diameter of the fiber was included to serve as a side lock and to perfectly center the fibers. The final specimen is shown in Figure 14 (b).

The samples were cast first in the two symmetrical sides of the mold, which were closed using a screw, subsequently placing the fiber and latch. One side was then filled with the mortar described in Section 2.1 (without the gravels). After waiting for at least 6 h to ensure hardening on this side, the other side was then filled with mortar. The specimen was demolded 24 h later. A schematic representation of the casting steps is shown in Figure 15. A caliper was used to measure the side without mortar, aiming at measuring the actual length of the side filled with mortar. After demolding, the samples were kept in a room with controlled

relative humidity and temperature (50 ± 5% and 20 ± 1°C, respectively) until the testing date, i.e., 28 days later.

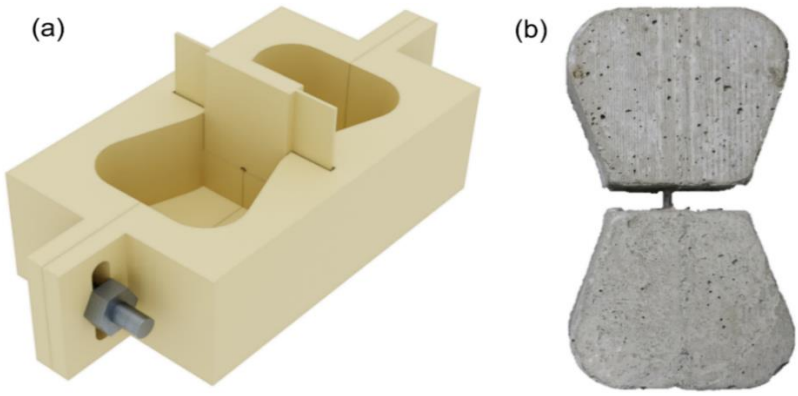

Figure 14. a) Mold for pullout test manufactured by 3D printing; b) Specimen after demolding.

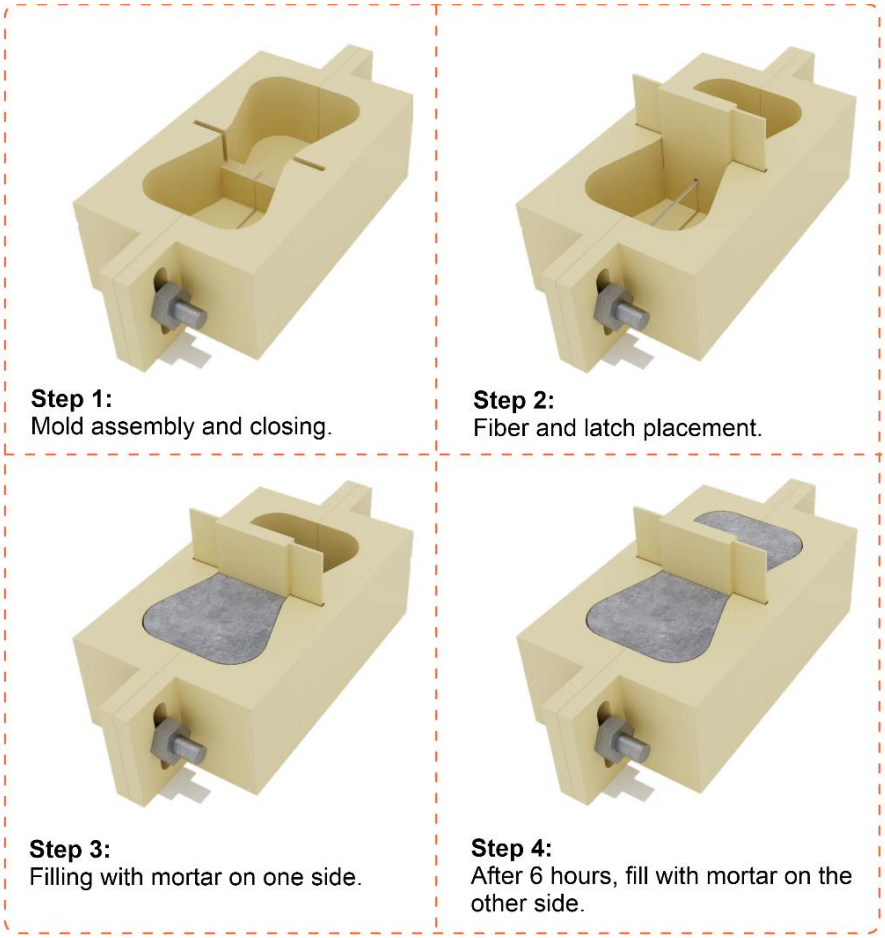

Figure 15. Sample molding steps using the printed molds.

3.2.4. Single-fiber pullout test

Pullout tests were performed to determine fibers' pullout behavior and assess force transfer through the fiber-matrix interface. Each test was performed with a single fiber cast on both sides, and the embedment length (L_c) was 20 mm. This length should be shorter than half the total fiber length to ensure that the interface behavior is governed by the side with the smallest shear area [24]. Because the fibers were 54- and 51-mm long, setting the embedment length at 20 mm enabled the comparison of different fibers and promoted preferential sliding on one side.

The pullout tests were performed on an MTS Series 809 axial/torsional test system with a hydraulic actuator, a servo-valve, and a load-frame maximum–axial-force capacity of 250 kN. A 5-kN load cell was coupled to the experimental setup, and the test was controlled by displacement at a rate of 1.5 mm/min. The samples were fixed in grips specially manufactured to hold them under a fixed boundary condition. A linear vertical displacement transducer (LVDT) was also positioned on a base coupled to the grip to measure deformation during load application. For each of the three fibers, six specimens were tested. The experimental setup and a test in progress are shown in Figure 16.

The maximum shear stress (τ_{max}) was calculated from the force measured by the load cell divided by the approximate lateral surface area as follows:

$$\tau_{max} = \frac{P_{max}}{2\pi r L_c} \quad (6)$$

where P_{max} is the maximum load, r is the equivalent radius (for non-circular fibers) calculated from the area of the transverse section of the fiber, and L_c is the embedment length (20 mm).

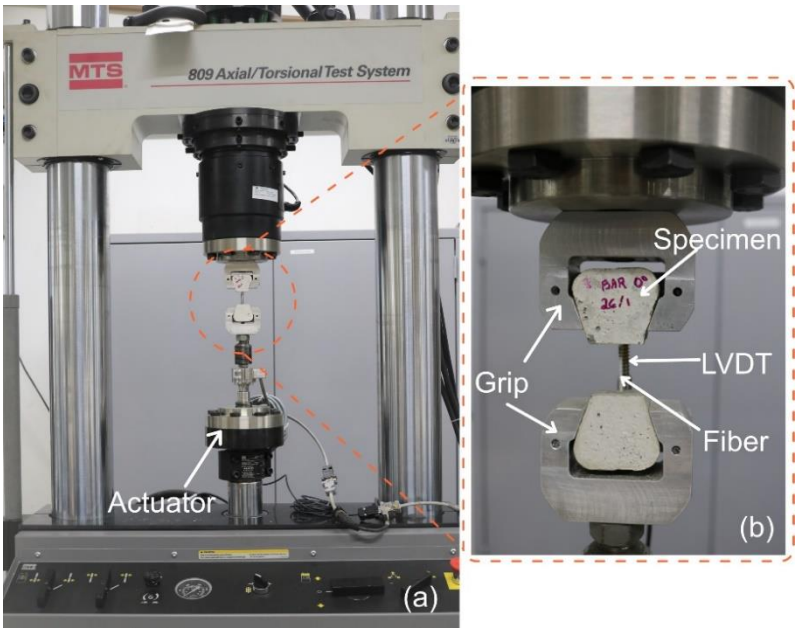

Figure 16. (a) Machine for axial/torsional tests (MTS 809); (b) Detail of the pullout test.

3.2.5. Single fiber pullout creep test setup

To assess the creep behaviors in pullout tests with sustained loading, a simple experimental setup was prepared using the same types of samples as those used in short-term tests. Given that both ends of the fiber were embedded in cement mortar, the test setup consisted of fixing the two halves of the sample in the shape of a “dog bone” and fixing the entire system to the rigid load frame with a clamp. The loading system was based on the distribution of free suspended weights on hooks attached to the set, properly aligned with the fiber. This ensured that, during assembly and testing, the faces of both sides of the sample remained parallel to represent the cracking plane. A steel plate was welded to the upper (fixed) hook that held the sample and extended to the halfway point of the lower (free) hook for specimen rotation constraint around the y-axis (indicated in Figure 17). Because this plate and the clamp holding the sample were in direct contact, their contacting surfaces were sanded and lubricated with oil to reduce friction. The pullout displacement was measured using a displacement transducer supported on a steel plate attached to the lower part of the clamp. Details of the proposed experimental setup and a test in progress are shown in Figure 17. Data were collected using an HBM 1615 data acquisition system and the software Catman Easy at a frequency of 0.02 Hz. The displacement acquisition software was activated before starting the test to measure the initial loading. The weights were placed gradually, starting from the largest weights, until all samples were loaded,

completing the process within 5 min. Given that the system resembled a pendulum, to avoid dynamic effects, the weights were carefully placed, and the environment was isolated to restrict external interference.

The tests were conducted in a room with controlled temperature and relative humidity of 20±1°C and 50±5%, respectively. Sustained loading was performed at 20, 30, 40, and 50% of the maximum average load assessed in the short-term pullout tests. Three samples were tested for each of the three loading percentages. These loading percentages were chosen because they represent the load fractions usually applied in service. At all loading percentages, the samples remained loaded for 10 days when they were unloaded. This setup found difficulties in measuring recovery after unloading due to the setup instability (pendulum behavior).

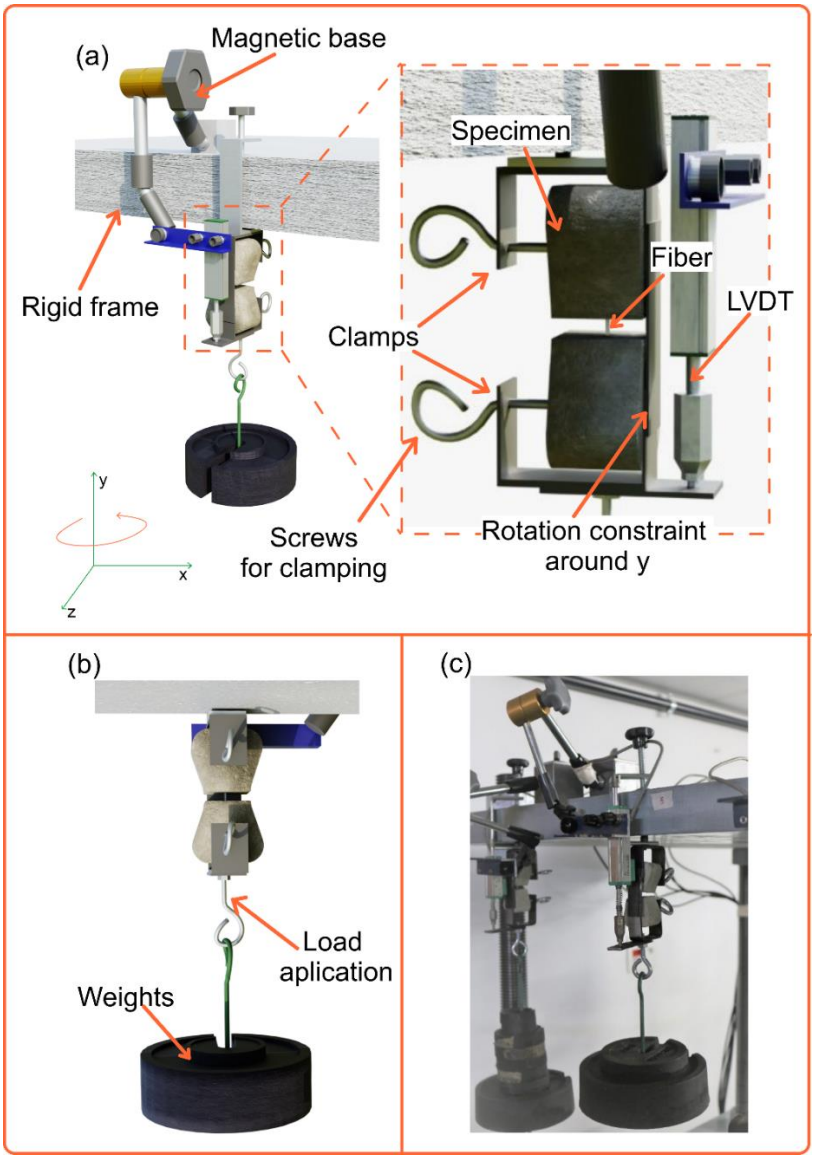

Figure 17. (a) Proposed creep pullout setup test with detail of its parts; (b) front view of the creep pullout setup; (c) actual test in progress.

3.2.6. Pullout creep mechanism using CT scan images

In addition to pullout tests with sustained loading, X-ray computed tomography scans were performed on one of the tested samples of each fiber at 50% loading of the quasi-static pullout tests. These images can provide additional information about the underlying mechanisms by enabling visualization and measurement of the actual slip at the unloaded tip of the fibers and, therefore, a comparison of the data with values measured by vertical displacement transducers during pullout tests with sustained loading.

Acquiring the CT scans required carefully preparing samples (Figure 19 (b)) as prismatic as possible so that the distances traversed by X-rays were approximately equal, thereby reducing artifacts (more uniform intensity and transmission). Once they were cut, the samples were glued with tape to a sample holder, as shown in Figure 18 (b).

The images were acquired on the Zeiss Xradia 510 Versa 3D X-ray Tomography System of the Department of Civil Engineering, Fluminense Federal University (*Universidade Federal Fluminense* – UFF), as shown in Figure 18 (a), using the acquisition software of this system, termed Scout-and-Scan™ Control System. The parameters adopted in the CT scans are outlined in Table 4. The CT scans lasted approximately 40 min and were acquired at 160-kV stress and 10-W power, with the sample rotating 360º. The distance from the source to the sample was 60 mm, whereas the distance from the sample to the detector was 78 mm. No filters were used.

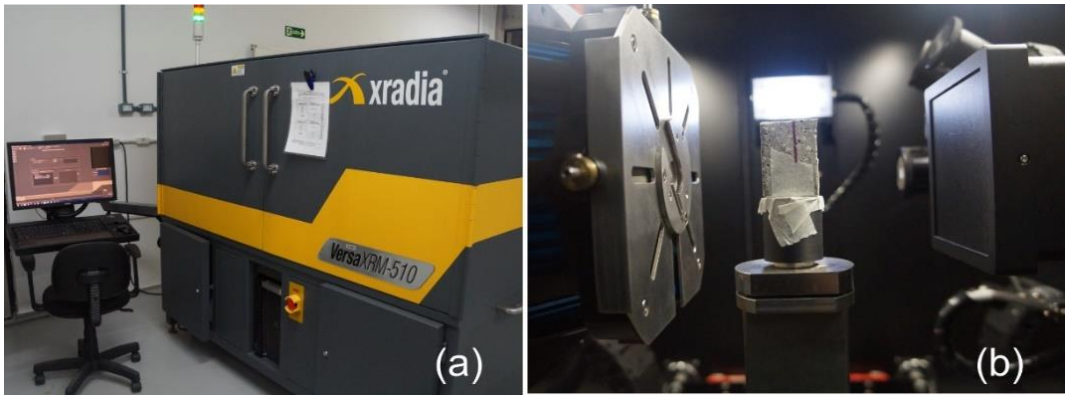

Figure 18. (a) Microtomograph model ZEISS Xradia 510 Versa; (b) Specimen positioned between the X-ray source and detector.

Table 4. Microtomography parameters.

Exposure time (s)	*Objective lens*	*Binning*	*Pixel size (μm)*	*Number of projections*	*Scan time*
2s	0.4X	1	15.0105	401	40 min

X-ray computed tomography images were automatically reconstructed by the software Reconstruction Scout and Scan [63]. The images generated in this software had approximately 15-μm³ voxel volumes. Image processing consisted of identifying the projection that contained the tip of the fiber using the software Dragonfly [64] (Windows 2022 version) and then extracting a single image of interest, which was then treated by applying the edge-preserving non-local-means filter [65]. This filter is available as a plugin of the software FIJI [59] for image denoising.

3.2.7. Pullout creep mechanism using electronic scanning microscopy (SEM)

SEM images were acquired to assess the debonding of the interface between the fiber and cement matrix and hence the slip of the fiber during the pullout tests with sustained loading. Given that the embedment length was 20 mm and SEM samples must have a volume of approximately 1 cm³, the sample previously tested and analyzed by microtomography was cut at 10 mm from the face of the fictitious crack while centering the sample (Figure 19 (c)). Thus, in addition to the displacement transducer values assessed during the test and the slip values at the unloaded tip assessed by microtomography, the slip was also assessed at an intermediate section between the loaded tip and the unloaded tip of the fiber.

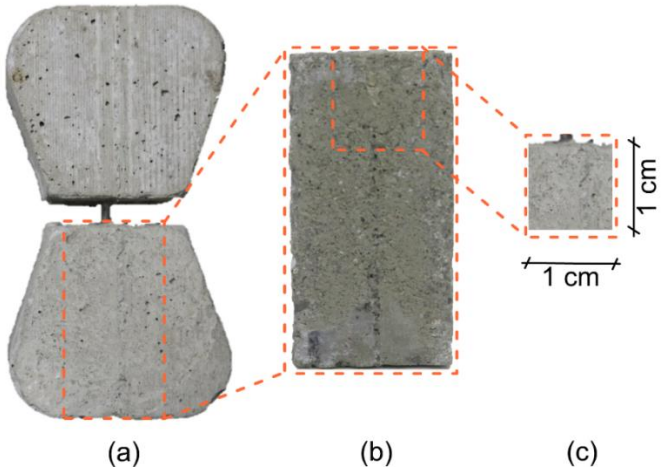

Figure 19. (a) Pullout sample; (b) identification of the sections made in the samples for microtomography; (c) scanning electron microscopy.

The analyses were performed on a TESCAN CLARA field-free analytical ultra-high resolution (UHR) SEM, operated by the Rheology Research Group (*Grupo de Reologia* – GReo) of the Department of Mechanical Engineering at Pontifical Catholic University of Rio de Janeiro (*Pontifícia Universidade Católica do Rio de Janeiro* – PUC-Rio). The samples previously cut for microtomography were then longitudinally cut into sections smaller than 1 cm³ at 10 mm from the loaded tip of the fiber, an intermediate height between the loaded tip and the final fiber tip, which had already been assessed by microtomography. The samples were dried in an oven at 50 °C for 48 h and kept in a desiccator for 72 h to remove their moisture as much as possible.

3.3. Results and discussion

3.3.1. Single fiber pullout test

Figure 20 shows the curves of the pullout tests performed for the three fibers studied at the same embedment length of 20 mm. The curves refer to the mean value of six samples, and the greyish shade represents the standard deviation. The mean values of real embedding length (the length measured after casting one side of the mold) and maximum load (P_{max}), and bond stress (τ_{max}) are outlined in Table 5, alongside the standard deviation of each series of tests. A significant standard deviation was observed, which may be explained by slight changes in the embedded lengths due to vibration and manual insertion of the fibers.

Table 5. Maximum load and bond strength of the pullout test

Fiber type	*Embedment length (mm)*	P_{max} *(N)*	τ_{max} *(MPa)*
BF	19.3 ± 0.829	189.4 ± *36.8*	3.85 ± *0.917*
TF	20.5 ± 1.47	132.5 ± *11.5*	2.66 ± *0.378*
VF	21.1 ± 1.24	22.7 ± *14.6*	0.559 ± *0.132*

In macro synthetic fibers, the low modulus of elasticity and hydrophobicity accounts for the low frictional bond between the fiber and the matrix. Under these conditions, pullout resistance is primarily promoted by friction, resulting in a typical failure due to a complete fiber pullout with significant surface abrasion [3,15,24,66,67]. In *BF* and *TF*, five of the six samples showed complete fiber pullout, and only one broke during the test. However, in *VF*, all fibers were completely pulled out. This is the desired outcome because this failure mode allows high deformation before the composite breaks.

In addition, fibers with surface corrugation (*BF* and *TF*) showed a higher bond strength than smooth fiber (*VF*). In fibers, this corrugation increases the bond to the matrix and explains the waveform shape of the curve after the peak. The wavy shape of the curve results from surface degradation in fibers with relief, promoted by the pullout process, which increases friction between the fiber and the matrix [14,68,69]. The number of waves may vary linearly with the embedment length, as suggested by Vrijdaghs *et al*. [37] and Li *et al.* [69]. In smooth fibers (*VF*), the debonding process starts with the nonlinearity of the curve (after reaching the maximum load P_{max}), followed by an approximately constant stretch (where the pullout behavior is governed by friction alone) until the complete pullout. The optical microscopy images shown in the before-and-after insets of pullout fibers in Figure 20 helped to corroborate the higher bond stress of *BF* fibers*,* which were notably degraded after the tests. In contrast, *TF* and *VF* fibers showed few signs of wear. High energy dissipation occurred through surface abrasion, increasing pullout resistance when the fiber was completely pulled out [28].

Babafemi *et al.* [14] found similar results when analyzing three fibers, one of which was *BF*, which showed a maximum mean load (P_{max}) of 174 N and a maximum bond stress (τ_{max}) of 3.26 MPa. The author also explained that *BF* showed the best pullout performance because this fiber had the largest equivalent diameter (0.85 mm versus 0.74 mm for the second-best result) and the strongest constituent material (with polyolefins outperforming polypropylene fibers). This hypothesis could also be valid for the fibers analyzed in this study.

Castoldi *et al.* [70] and Lima *et al*. [7] conducted pullout tests with *VF* fibers and reported bond stresses (τ_{max}) of 0.30 and 0.52 MPa. In the study by Castoldi *et al.* [70], the fiber was the same, albeit with an embedment length of 25 mm. Conversely, in the study by Lima *et al*. [7], the fiber was a slightly smaller version of *VF* with a length of 40 mm and an embedment length of 10 mm. Monteiro [71] tested the pullout of *BF* and *TF* fibers, reporting bond stress (τ_{max}) values of 3.0 and 2.24 MPa, respectively. In all cases, the shape of the curves and the values match those of the fibers *BF*, *TF,* and *VF* tested in this study.

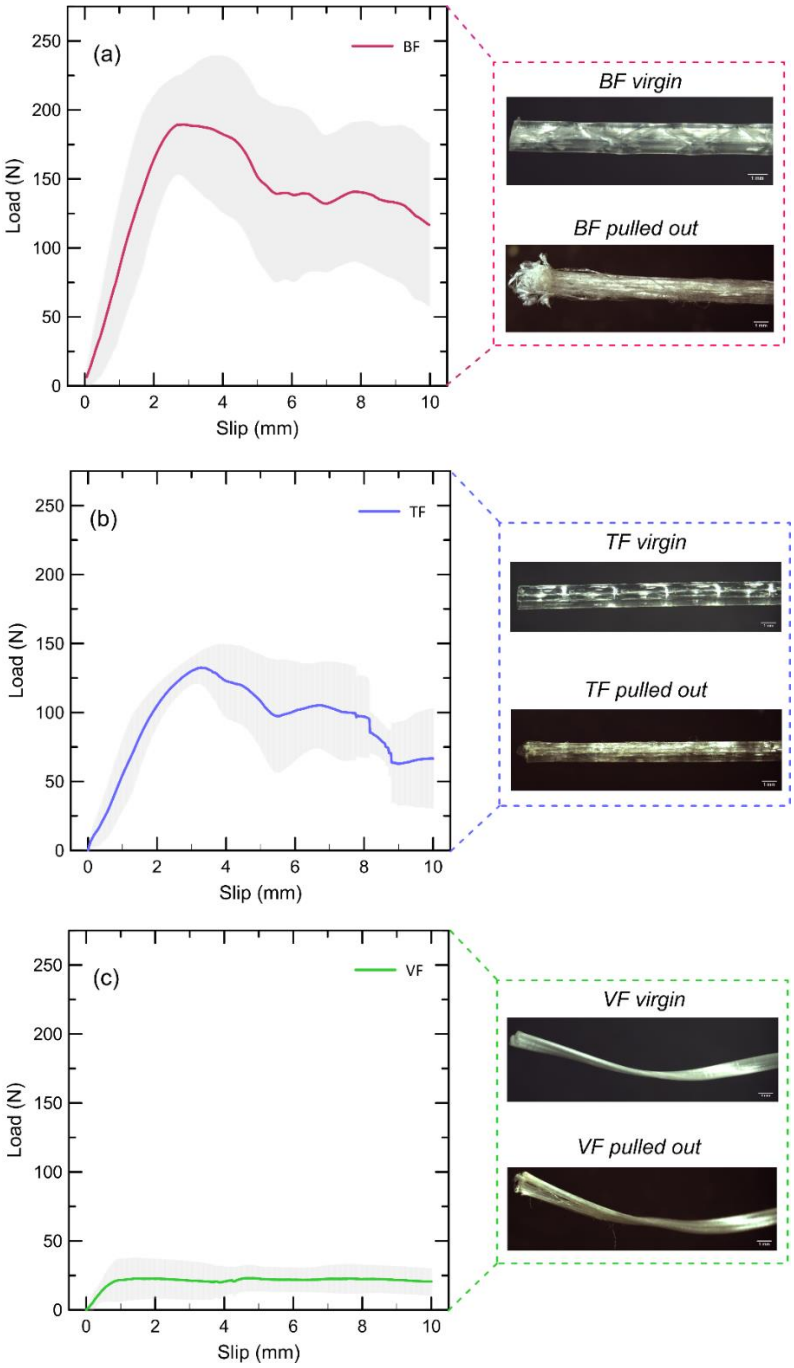

Figure 20. Curve of pullout force *versus* slip of the fiber (a) *BF*; (b) *TF*; (c) *VF*.

3.3.2. Single fiber pullout creep test

The curves of slip as a function of time are shown in Figure 21, Figure 22 and Figure 23. The curves in (a) show the results of three samples subjected to the same level of load (50%), whereas the curves in (b) show the mean values of the three curves at 50% load and of a sample at each of the other load levels normalized according to Eq. (2).

All fibers showed an instantaneous pullout displacement (δ_{inst}) (essentially elastic [35]) immediately after applying the load. According to Babafemi *et al.* [14], once the load is applied, an initial displacement occurs around the fiber, a few mm from the entry point of the matrix into the fiber. The experimentally measured instantaneous displacement (δ_{inst}) reflects the instantaneous elongation of the fiber along the free length [14,15], but some portion of instantaneous pullout can also be considered. In this case, given that both sides of the fiber are embedded in the matrix, a portion of displacement can be assigned to the non-preferred side of the pullout (longer embedded length). At a 50% load level, the fiber *TF* showed the highest initial displacement; if assumed as a fiber elongation, this initial displacement may be related to the stiffness of the material.

In *BF* and *TF* fibers, the pullout continued to increase at a decreasing rate over time during the test, whereas two of the three samples of *VF* fibers tested at a 50% load level were completely pulled out within 48 h, as shown in Figure 23 (a), reflecting a state of tertiary creep with sudden fiber pullout. In all other cases, the fibers experienced a secondary creep stage, with a decrease in the slip rate over time. The final mean pullout displacement at 10 days and under 50% load was 0.301 mm for *BF*, 0.624 mm for *TF,* and 0.219 mm for *VF* (considering that only one of the three fibers tested reached 10 days without breaking). For the VF fibers, the shape of the observed displacement versus time curve was different from the other fibers. The curve in the form of steps can be justified due to the intense porosity of this sample, which may have facilitated an abrupt pullout in regions with pores at the fiber-matrix interface. A more detailed explanation along with the micro-CT images are shown in Section 3.3.

The instantaneous displacement (δ_{inst}) and creep coefficient (φ_{creep}) in pullout are shown in Figure 21 (b), Figure 22 (b), and Figure 23 (b). The creep coefficient is defined as follows:

$$\varphi_{creep}\,(t) = \frac{\delta_{creep}(t)}{\delta_{inst}} \tag{7}$$

where *t* is the time at which $\varphi_{creep}\ (t)$ is determined. For the ages of 3, 7 and 10 days, these parameters of the three fibers are summarized in Table 6.

The creep coefficient ($\varphi_{creep}\ (t)$) increases over time at all load levels, albeit at a decreasing rate. The stiffness and strength of polymer fibers are sensitive to changes in temperature and humidity, and even in a controlled environment, as in this study, significant deformations were observed within 10 days. Because polymer fibers are weakly bonded to the matrix, even at low load levels (such as 20%), slip creep occurs in all three fibers tested. However, the values assessed in this study cannot be attributed only to pullout creep. The creep of the fiber itself can be considered the main mechanism of composites reinforced with macro polymer fibers[14,15], as discussed in more detail in Section 3.4.

In the three types of fiber under study (*BF*, *TF,* and *VF*), the curves at a 20% load slightly deviate from the other three curves shown in Figure 21 (b), Figure 22 (b), and Figure 23 (b). In these normalized graphs, the results are closer, although a significant variation can also be observed.

Among the results published in the literature, Babafemi *et al*. [14] reported a creep displacement of 0.760 mm for *BF* versus 0.298 mm assessed in this study for the same 10-day period. For *VF*, Lima *et al.* [7] succeeded in recording results at a 50% load level but only reached tertiary creep in samples subjected to 75% load, even for the slightly shorter *VF* fiber (40 mm) with an embedment length of 10 mm. In addition, the authors reported an average displacement of 0.034 mm at 6 days and a 50% load level versus 0.219 mm at 10 days assessed in this study. For *TF*, no reports were found in the literature.

It is important to emphasize that the results obtained do not represent the real situation of the composite since other factors, such as fiber orientation, influence the pullout behavior and were not considered in the results. The fiber orientation is an extremely important parameter since in a real composite the fibers are randomly dispersed and this orientation can either increase or reduce the composite strength [32,72–74]. However, this article aims to understand the pullout behavior with fibers aligned with the loading direction and the understanding of the behavior when the orientation is different from 0°, although it is of paramount importance, it is not addressed.

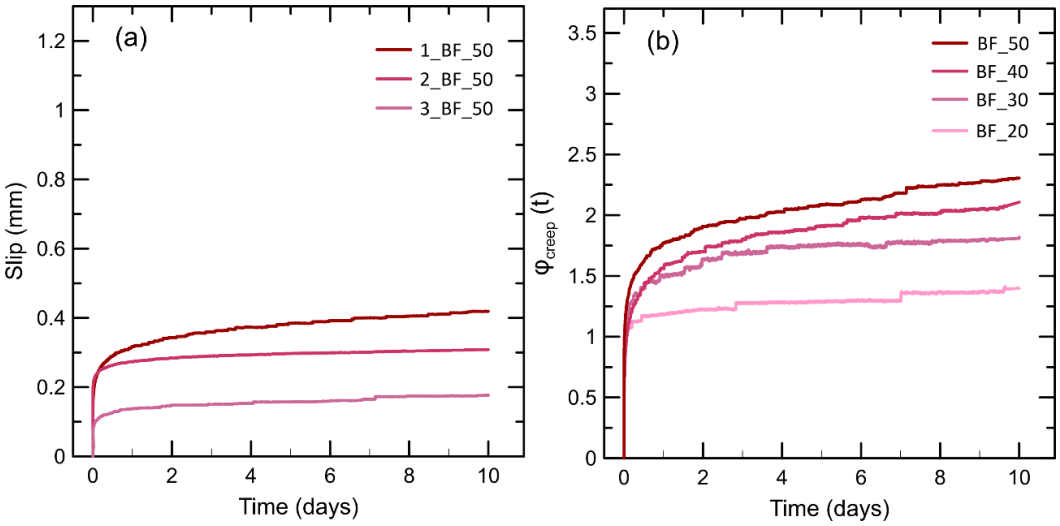

Figure 21. (a) Slip *versus* time curves for the *BF* fiber loaded at 50% of its pullout resistance load; (b) creep coefficient ($\varphi_{creep}\ (t)$) over time for all loading levels tested.

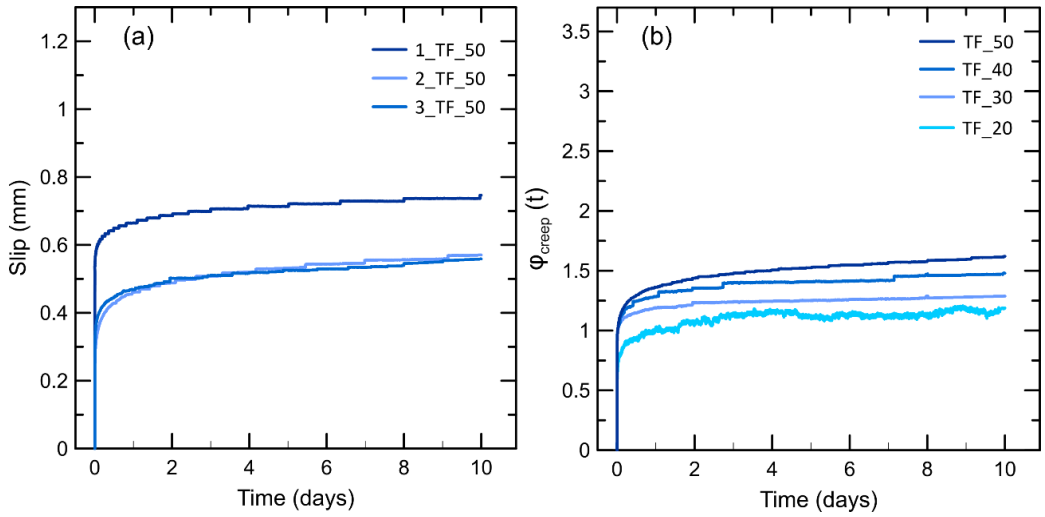

Figure 22. (a) Slip *versus* time curves for the *TF* fiber loaded at 50% of its pullout resistance load; (b) creep coefficient ($\varphi_{creep}\ (t)$) over time for all loading levels tested.

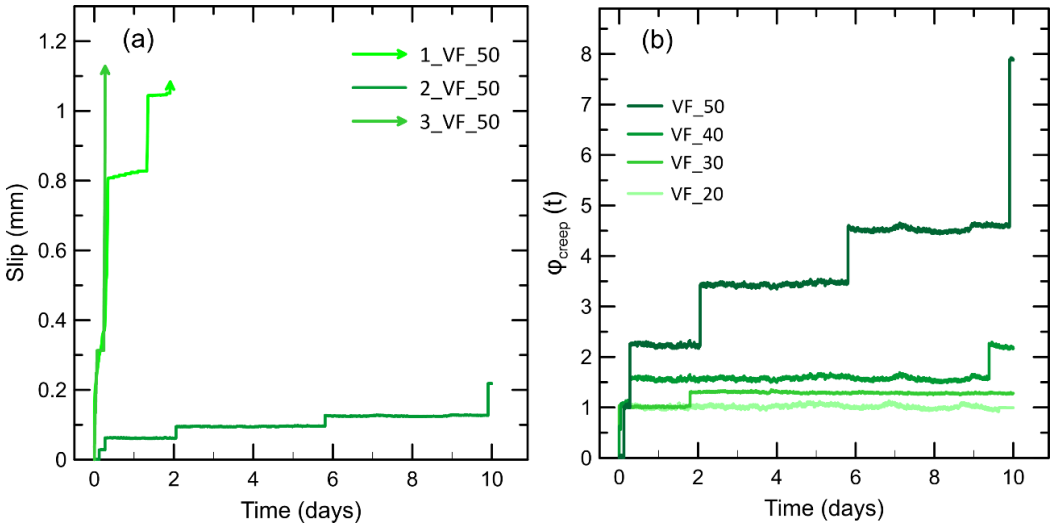

Figure 23. (a) Slip *versus* time curves for the *VF* fiber loaded at 50% of its pullout resistance load; (b) creep coefficient (φ_{creep} *(t)*) over time for all loading levels tested. **Note the different creep coefficient scale, compared to the same graphs of the other fibers studied.

Table 6. Summary of the parameters obtained from the pullout tests under sustained load.

Fiber type	δ_{inst} *(mm)*	φ_{creep}		
		3 days	*7 days*	*10 days*
BF_20	*0.066 ± 0.031*	*1.28 ± 0.491*	*1.30 ± 0.428*	*1.40 ± 0.394*
BF_30	*0.052 ± 0.002*	*1.37 ± 0.049*	*1.44 ± 0.046*	*1.48 ± 0.041*
BF_40	*0.144 ± 0.033*	*1.80 ± 1.14*	*2.01 ± 1.43*	*2.11 ± 1.56*
BF_50	*0.364 ± 0.064*	*1.97 ± 0.174*	*2.18 ± 0.213*	*2.31 ± 0.191*
TF_20	*0.999 ± 0.027*	*1.42 ± 0.553*	*1.43 ± 0.624*	*1.49 ± 0.706*
TF_30	*0.245 ± 0.134*	*1.24 ± 0.587*	*1.26 ± 0.556*	*1.29 ± 0.723*
TF_40	*0.146 ± 0.143*	*1.40 ± 0.147*	*1.42 ± 0.136*	*1.48 ± 0.131*
TF_50	*0.396 ± 0.139*	*1.49 ± 0.226*	*1.59 ± 0.275*	*1.64 ± 0.287*
VF_20	*0.010 ± 0.005*	*0.996 ± 0.005*	*1.08 ± 0.152*	*0.994 ± 0.594*
VF_30	*0.038 ± 0.049*	*1.29 ± 0.268*	*1.29 ± 0.120*	*1.28 ± 0.181*
VF_40	*0.037 ± 0.036*	*1.57 ± 1.759*	*1.58 ± 1.540*	*2.17 ± 1.537*
VF_50[a]	*0.027 ± 0.08*	*3.43* [a]	4.53 [a]	7.89 [a]

[a] *No standard deviation as only one sample reached age without breaking.*

A 4-parameter rheological Burgers model is used to evaluate the viscoelastic behavior of composites and predict the pullout behavior over time. In an adaption of the original equation that correlates strain, stress and time, in this work, the

model will be adopted to correlate the pullout displacement, bond stress and time, as follows:

$$\delta(t) = \frac{\tau_0}{R_1} + \frac{\tau_0}{R_2}\left(1 - exp\left(\frac{-R_2 t}{\eta_2}\right)\right) + \frac{\tau_0}{\eta_1} t \quad (8)$$

where δ(t) is the pullout displacement at a given time t, τ_0 is the bond stress, R_1 is the instantaneous elastic stiffness of the Maxwell unit, R_2 is the elastic stiffness of Kelvin–Voigt representing the contribution of the retarded elastic region, η_1 is the dashpot of the Maxwell element that represents the residual viscosity, and η_2 is the dashpot related with Kelvin–Voigt that represents the internal viscosity.

The parameters of this model were determined from regression of the mean experimental data obtained in the creep tests and are reported in Table 6, along with the coefficient of correlation R^2. In addition, a comparison of the experimental curves and models for the three types of fibers at 50% loading level is depicted in Figure 24.

Table 7. Burgers model parameters for the three fibers at all their sustained loading levels.

Fiber type	*Loading level*	*Burgers model parameters*				*R²*
		R_1 (MPa/mm)	*R_2 (MPa/mm)*	*η_1 (MPa.s/mm)*	*η_2 (MPa.s/mm)*	
BF	50%	13.1	22.5	2.37×10^7	8.59×10^5	0.99
	40%	11.1	40.6	5.91×10^7	1.91×10^6	0.98
	30%	23.6	53.1	1.64×10^8	4.65×10^6	0.97
	20%	11.9	70.3	5.09×10^7	2.21×10^6	0.96
TF	50%	3.07	11.2	1.53×10^7	5.94×10^5	0.99
	40%	6.94	26.2	4.39×10^7	1.24×10^6	0.97
	30%	3.12	18.9	3.86×10^7	9.50×10^5	0.98
	20%	10.75	22.1	7.54×10^7	1.70×10^6	0.97
VF[a]	50%	8	20	2.16×10^6	1.35×10^5	0.79
	30%	4.67	10.6	3.80×10^{11}	1.54×10^6	0.72

[a] It was not possible to perform the regression with a correlation coefficient above 70% for stress levels 20% and 40% of the *VF*.

It can be observed that coefficients of correlation remained above 0.96 for *BF* and *TF* fibers at all load levels, demonstrating a good fit. On the other hand, due to the significant variation and 'steps' in the results for *VF* samples (Figure 24), lower coefficients of correlation were obtained, resulting in a poorer fit. For *VF* fibers at stress levels of 20% and 40%, the model could not be applied. According to the parameters obtained and presented in Table 7, the *BF* samples presented the highest values for R_1 (ranging between 11.07 and 23.61 MPa/mm), followed by the *TF* samples (ranging between 3.12 and 10.75 MPa/mm). The slightly higher stiffness attributed to the *BF* sample may be due to the better adhesion between the fiber and the matrix, demonstrated in the pullout tests. Parameter η_2 regulates how fast the curve enters the secondary creep stage. For all loading levels and all samples, the lowest values were found for the highest loading percentages (50%), indicating a primary creep characterized by longer periods of time. It is also important to highlight that the dependence of the elastic properties on the applied stress is characteristic of nonlinear viscoelastic behavior.

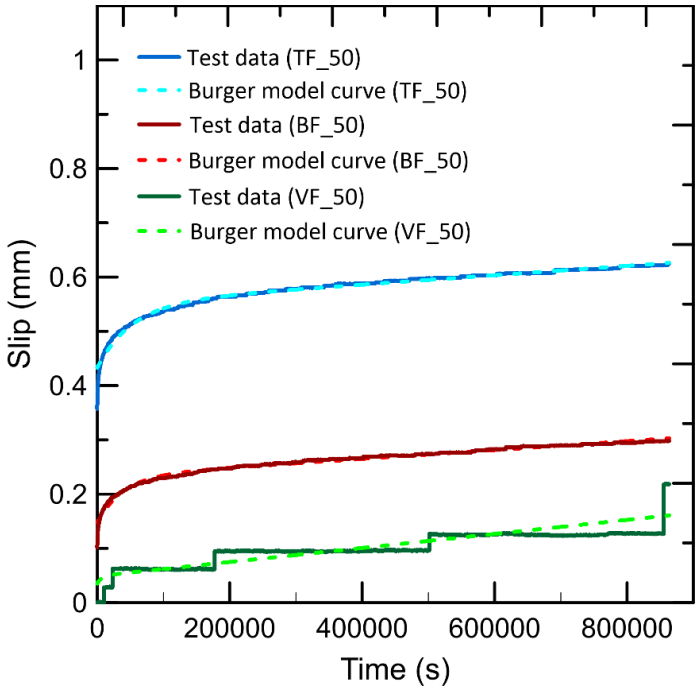

Figure 24. Comparison analysis between the experimental value and rheological Burgers model results.

3.3.3. Pullout creep mechanism using CT scan images

To avoid spending excessive time acquiring CT scans, a relatively low number of projections was used. Given the low density of polymer fibers, very little

difference was observed between fiber and matrix pores. Thus, only the displaced tip of the fiber could be identified, presenting approximately the same shade as the pores. We were unable to identify its slip along the length of the fiber and the lateral contraction of the fiber due to the *Poisson* effect, especially because the images were obtained after the test and in an elastic section where there is recovery.

BF showed no visible sign of tip slip after 10 days under a 50% load level, as shown in Figure 25. Babafemi *et al*. [14] also measured *BF*-fiber tip slip, establishing a sample load and a de-load process for imaging at some stages (1, 14, 21, and 24 days), subsequently subjecting the samples to a new load. Their objective was to analyze the mechanisms that occurred over time and to compare the findings with displacement results measured by displacement transducer. In the first three stages (up to 22 days), microtomography images did not show any tip slip, whereas displacement transducer readings indicated displacements, initially identified as creep. Only after the fourth load cycle (at 24 days), when they increased the load level to 60%, were the authors able to measure tip slip, recording a value of 0.35 mm, whereas the displacement transducer indicated 1.5 mm. In conclusion, the instantaneous strain measured in these tests is nothing more than fiber elongation, and fiber creep is the dominant factor in pullout under sustained loading.

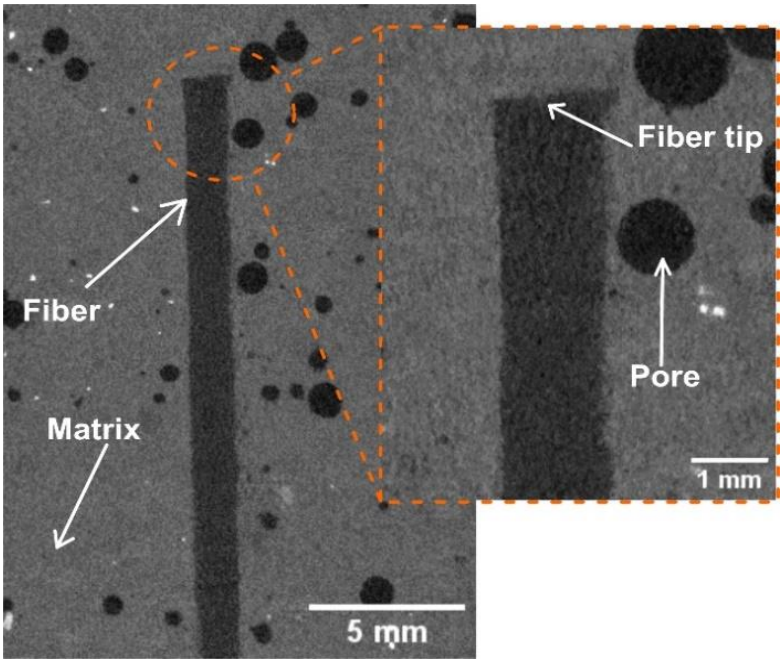

Figure 25. X-ray microtomography image of the sample containing the *BF* fiber tested to pullout with sustained loading for the 50% loading level.

Conversely, *TF* showed a tip slip consistent with displacement transducer values recorded in the pullout test with sustained loading, as shown in Figure 26. Because the tip was not regular, two orthogonal measurements were performed. In one of them, the slip was 0.330 mm, whereas, in the other measurement, the slip was 0.188 mm. *VF* also displayed tip slip, as shown in Figure 27. In this case, the microtomography value was higher than that displacement transducer value, with tip measurements of 0.301 mm and 0.291 mm, respectively. The microtomography and displacement transducer values are outlined in Table 8.

An important observation is that matrix porosity was more visible around the *VF* fiber because all specimens had the same dosage and were molded in exactly the same way. This result can be explained by the bonding difficulty of fibers with a twisted geometry, which increased the porosity and further weakened the interface. This behavior was observed by Peled *et al*. [67] in crimped fibers, which prevented an efficient packing of cement particles, generating large voids around the fiber and at the interface. This high porosity, including a pore longer than 5 mm exactly between the fiber and the matrix (Figure 27), could be the reason why only one of the fibers at 50% load reached 10 days without being pulled out, which was precisely this fiber. In addition, creep pullout increased abruptly (Figure 23), creating steps in the graphs over time, possibly due to the high porosity of some regions of the fiber without interface with the matrix, thus facilitating the pullout. The overly porous matrix and these pores at the interface resulted in the premature pullout, impairing the overall performance of the composite. This type of fiber is also associated with the formation of bundles [69], which decrease the interaction between the matrix and the fiber because fibers must be uniformly distributed in the matrix to be effective. Furthermore, 0° orientation cannot be guaranteed, as the fiber is extremely deformable.

These bond problems and the high porosity might have been why *VF* showed a tip displacement measured in microtomography images higher than that measured by displacement transducer. Because the bond was weakened, the demolding and assembly of the creep test might have caused some displacement in the fiber, given that a pore larger than 5 mm was present at the interface between the fiber and the matrix. These results might have been significantly affected by the high sensitivity of the test and by the fiber in question.

Figure 28 also shows microtomography images of *TF* and *VF* fibers tested at 40% load level. At this load percentage, the fibers did not show tip displacement and thus did not require imaging lower loads. Both fibers were damaged, including

split in half, a behavior that is commonly observed even in fibers that were not used in the test.

The findings reported by Babafemi *et al.*[14] on *BF* are similar to the results found in this study, corroborating the hypothesis of the key role that fiber creep plays in the overall behavior of the composite, especially for macro synthetic fibers with a higher modulus of elasticity. In the same testing period, the *TF* and *VF* fibers showed different behaviors, with a significant tip slip. Babafemi *et al*. [14] also tested the creep pullout of another fiber (with a modulus of elasticity exceeding half the value reported for *BF*), reporting tip slip in the first stage (1 day) assessed in microtomography images. Because *VF* had bond problems, the *BF* and *TF* fibers were compared. Both fibers with the same length, very similar surface relief and equivalent diameter showed significant differences in creep. Thus, the modulus of elasticity and possibly the shape of the transverse section (as discussed in Section 3.5) may affect the final performance under sustained loading.

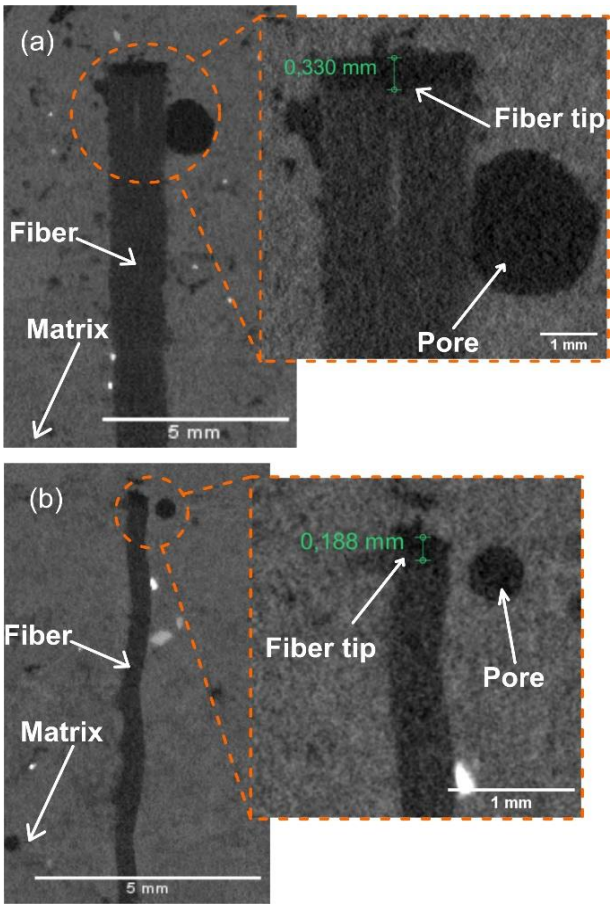

Figure 26. X-ray microtomography image of the sample containing the *TF* fiber tested to pullout with sustained loading for the 50% loading level, where (a) x-y view and (b) z-y view.

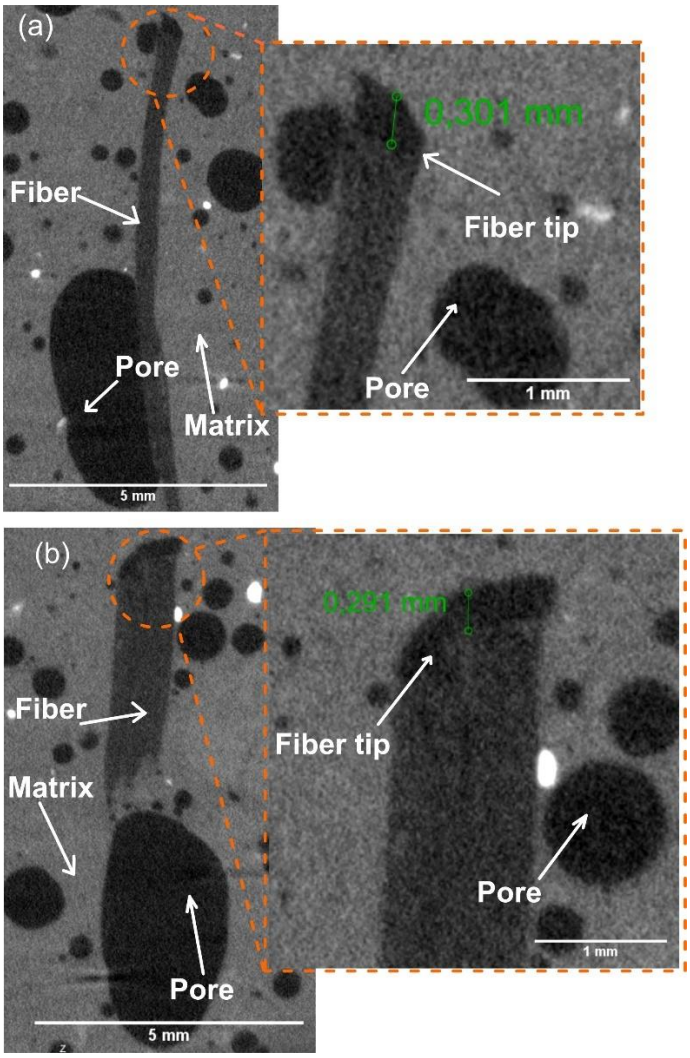

Figure 27. X-ray microtomography image of the sample containing the *VF* fiber tested to pullout with sustained loading for the 50% loading level, where (a) x-y view and (b) z-y view.

Table 8. Summary of values measured by microtomography and displacement transducer.

Measurement	*3_BF_50*	*2_TF_50*	*2_VF_50*
At pullout (mm)	0.177	0.570	0.219
At microCT (mm)	0	0.330	0.301

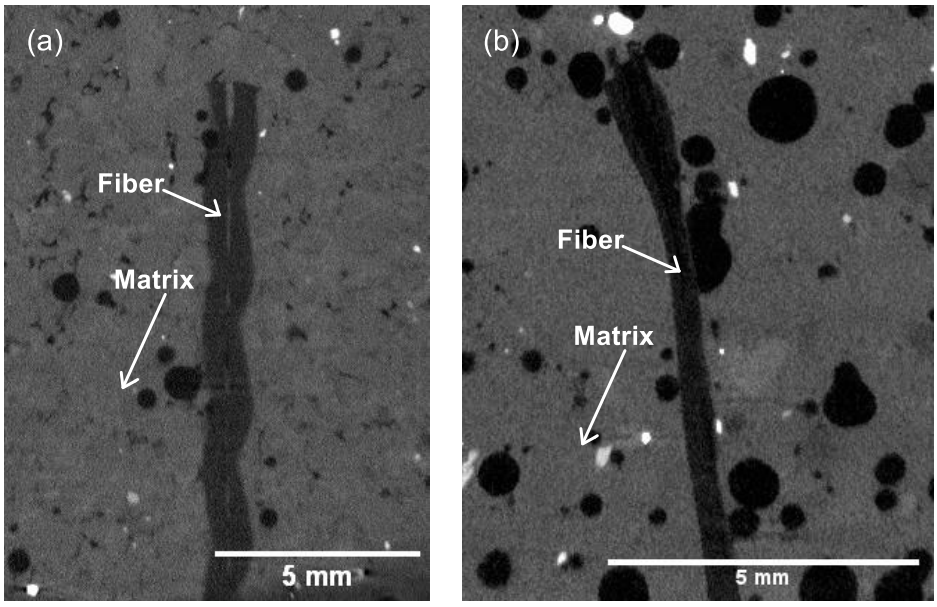

Figure 28. X-ray microtomography image of (a) the sample containing the *TF* fiber tested to pullout with sustained loading for the 40% loading level and (b) the sample containing the *VF* fiber tested to pullout with sustained loading for the 40% loading level.

3.3.4. Pullout creep mechanism using electronic scanning microscopy (SEM)

SEM made it possible to identify, in this case, the loss of bond along the embedded length. As shown in the previous section, for the specific case of the *BF* fiber, we were unable to identify the slip at the fiber tip by microtomography. Thus, the displacement measured in this fiber could have basically reflected fiber elongation without pullout *per se*. However, as shown in the images of Figure 29, a significant loss of bond occurred in the intermediate section, where the entire fiber perimeter was detached from the matrix. This finding suggests that, after stretching, the fiber lost its bond to the matrix and that some slip may have occurred, especially in the loaded tip, which is the most used area, initially. At the loaded tip, the inset in Figure 29 (b) shows that a part of the fiber perimeter was still well bonded to the matrix, whereas another portion had already lost the bond. These results indicate a non-uniform fiber pullout. However, we cannot disregard the possibility that the fiber has lost bond as a result of the manipulation to cut the sample and the temperature change experienced, which could cause it to contract.

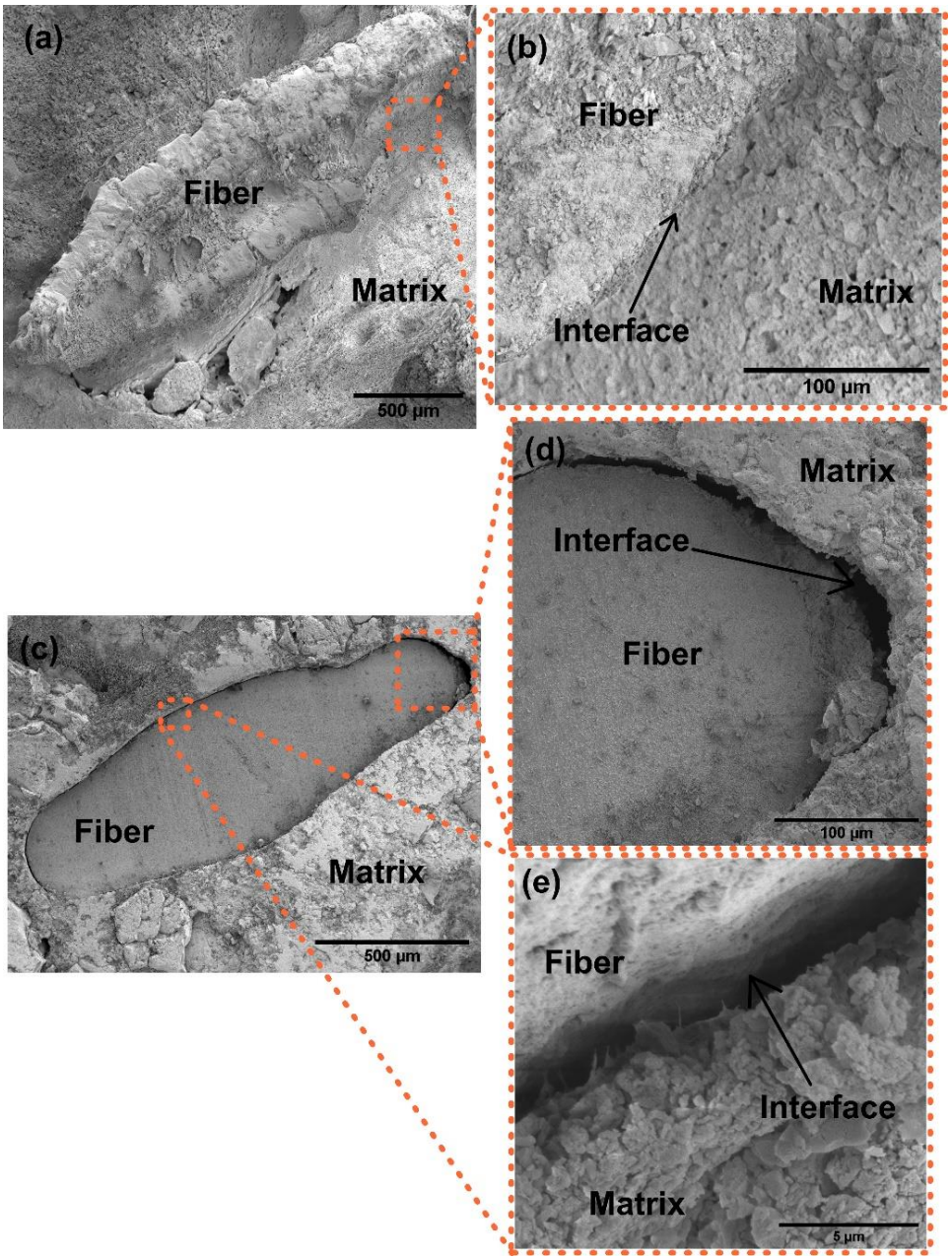

Figure 29. SEM images of the *BF* fiber: (a) tip loaded 130x; (b) tip loaded 2000x; (c) intermediate section 200x; (d) intermediate section 1000x; (e) intermediate section 10000x.

SEM images of *TF* fibers are shown in Figure 30. In both the loaded tip and mid-section of the fiber, loss of bond is observed virtually along the entire perimeter. An important detail shown in Figure 30 (e) is the degradation of the fiber, which is split in two. This separation is even observed in fibers not yet used, which can interfere with the final performance of the composite and with the bond to the matrix. Another issue that must be stressed is the shape of the transverse section of this fiber, which had the same size, the same material, and approximately the same equivalent diameter as the *BF* fiber, but considerably differed in

performance, especially in pullout. Among the possible explanations, this difference may be attributed to the shape of the transverse section, with sharp corners and angles smaller than 90°. During pullout, these corners can concentrate tensions, favoring bond loss in these regions and, therefore, fiber pullout.

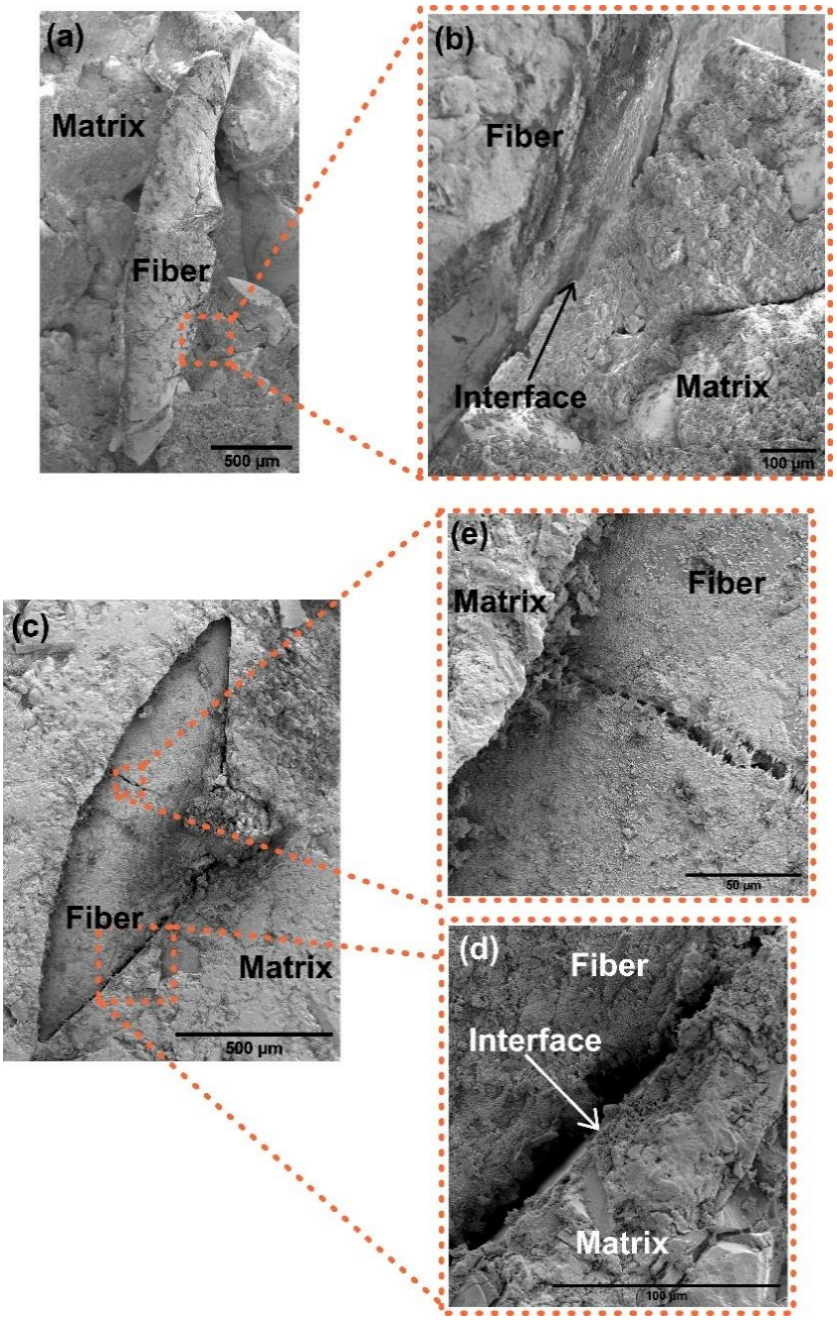

Figure 30. SEM images of *TF* fiber: (a) tip loaded 100x; (b) tip loaded 400x; (c) intermediate section 200x; (d) intermediate section 2000x; (e) intermediate section 2000x.

The images of the *VF* fiber are shown in Figure 31. In this specific case, it was only possible to image the loaded tip because the fiber was twisted. When cutting, and obtaining a 1-cm³ sample, the part containing the fiber was ultimately

cut, and the sample was lost. However, the loaded tip of this fiber showed a much more porous matrix than those of the other fibers, albeit with the same matrix. Very large pores were observed around the fiber, which may have contributed to the final pullout performance. Given that the matrix in this fiber was the same as in the other samples, we hypothesize that the twisted fiber required higher bonding energy because it underwent exactly the same casting procedure, but the density was insufficient, creating bubbles (pores) around the fiber. In addition, polypropylene is hydrophobic, which prevents a well-consolidated bond and can lead to high porosity when the constituent materials are not homogeneously mixed.

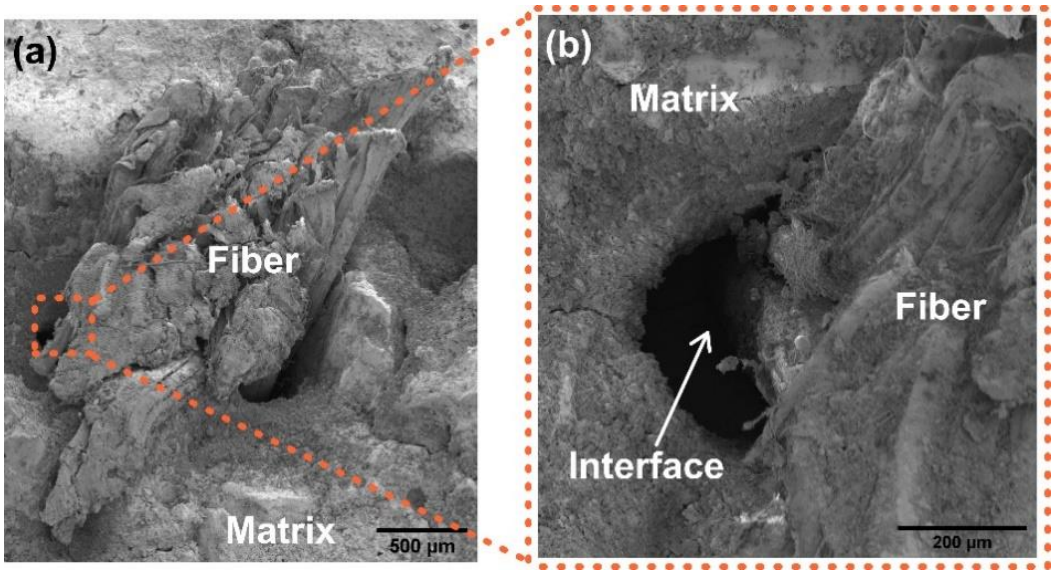

Figure 31. SEM images of the *VF* fiber: (a) tip loaded 100x; (b) tip loaded 400x.

3.4. Conclusions

Short- and long-term pullout tests were conducted to clarify the mechanisms behind the creep of composites reinforced with polymeric macro fibers, particularly in the portion referring to creep at the matrix–fiber interface. As a result, the following conclusions can be drawn:

1. In pullout tests under short-time loading, the typical failure mode was complete fiber pullout. The crimped fibers (*BF* and *TF*) showed higher bond strength and marked surface degradation, whereas the twisted fibers (*VF*) were pulled out almost exclusively due to friction, without

any signs of abrasion. Geometric properties seem to have a significant impact on these results.

2. The Burgers model was applied to the experimental curves and resulted in a good fit for all load levels of the *BF* and *TF* samples. On the other hand, the regression for *VF* samples resulted in lower correlation coefficients due to the ‘steps’ (discontinuities) present in the pullout curves. The parameters can be important for modeling cementitious composites in fiber scale.
3. Microtomography images of the fiber ends were obtained after the pullout tests were performed under a sustained load of 50% to compare the displacements measured by the transducer. The results indicate that the *BF* fiber did not exhibit a displacement at the end; thus, the displacement measured by the transducer may have resulted from the creep of the non-embedded part of the fiber and interface creep of the part embedded in the matrix. Concerning the *TF* fiber, approximately 58% of the strain measured was related to the end displacement shown in the microtomography images. In contrast, the *VF* fiber exhibited an end displacement greater than that measured by the transducer, exhibiting a much more porous matrix than the other samples, with pores greater than 5 mm at the fiber-matrix interface, significantly impacting the fiber-matrix bond, while the sample handling itself may have resulted in larger fiber displacement.
4. Images obtained by scanning electron microscopy (SEM) in an intermediate section along the embedded length showed that all fibers had lost bond with the matrix, with the interface degraded. An important observation about the cross-section of the *BF* fiber is that it has sharp corners with angles smaller than 90°, which can impact its pullout performance, given that these are regions that concentrate stresses.
5. Therefore, it can be concluded that the final pullout creep is largely attributed to the creep of the fiber itself. The characteristics and properties of the different fibers considerably influence the final response under sustained load, making it difficult to predict the creep of this type of composite.

4. INFLUENCE OF FIBER ORIENTATION ON THE BEHAVIOR OF MACRO SYNTHETIC FIBER IN SHORT- AND LONG-TERM PULLOUT TEST

4.1. Introduction

Macro synthetic fibers have been widely used in cementitious matrix reinforcement applications. However, some of their characteristics and effects have yet to be elucidated. Notably, polymeric materials tend to respond to short-term loads elastically, although they present a viscous behavior with sustained loads over time, deforming indefinitely [75]. As structures need to be designed for a specific working life, the creep behavior of these materials should be investigated, considering that the structural life span is limited by the time to creep failure [75].

Pullout tests are commonly used to investigate fiber–matrix interactions, as they can measure the force required to extract embedded fibers. The pullout and flexural strength curves of the composite, although extremely representative of the real behavior, are influenced by various fiber and matrix characteristics, such as the angle of inclination of the fiber concerning the direction of the load. In real composites, the distribution and orientation of fibers are generally random with respect to possible fracture planes, primarily influenced by factors such as the placement point and direction, element geometry, and the use of vibrators [76]. In addition, fibers often tend to assume angles other than 0° with respect to the direction of the load, affecting the overall composite strength.

The angle of inclination of the fibers can influence the pullout behavior in several ways. However, these responses are primarily dependent on fiber shape and properties, mainly whether the fiber is steel or synthetic [69]. The pulling process, as suggested by Li *et al*. [69] and Wu and Li [77], is analogous to a cable passing over a friction pulley. A concentration of stresses occurs on the pullout surface, close to the support point, increasing the frictional resistance due to the high contact pressures (snubbing effect) [69,74]. Owing to the tensions applied to the matrix at the fiber exit point, a local fragmentation may occur as the angle increases [34,69]. The snubbing effect is more significant in polymeric fibers than in steel fibers owing to premature matrix fragmentation caused by the high stiffness and elastic resistance of steel fibers [69]. In addition, the fibers are obliged to slip

through this fragmented region, causing plastic deformations in the fiber [34] and increasing its probability of failure [31], especially in the case of deformed fibers with superficial corrugation [34].

The pullout behavior under a sustained load can also depend on the angle of inclination of the fibers. Considering steel has negligible creep at ambient temperature [75,78], its long-term load-carrying capacity is not a concern. However, owing to their viscoelasticity, polymeric materials exhibit high deformations over time [14,15,75,78]. Therefore, some studies have extensively investigated the pullout mechanisms of polymeric macro fibers under a sustained load [3,7,14,15,36]. Their results show that pullout creep is caused by a combination of fiber creep and pullout creep [3,14,15], with the shape, surface corrugation of the fiber and its modulus of elasticity [36] being the main parameters that govern the behavior under sustained load. However, none of these studies considered the effects of fiber orientation over time.

The mechanical behavior of fiber-reinforced composites is significantly related to the pullout behavior of an individual fiber. If inclined fibers behave differently from aligned fibers during the pullout, the performance of these composites cannot be evaluated solely based on fiber-aligned results. As the fibers are embedded into the matrix to bridge the cracks, an inclination concerning the direction of the load can impair the overall toughness of the composite. Therefore, the snubbing and matrix fragmentation effects for inclined fibers must be considered when modeling the pullout behavior under sustained load, especially when polymeric fibers are used.

This study performed pullout tests with fibers inclined at angles at 15°, 30°, and 45° for three different macro synthetic fibers. First, a quasi-static test was conducted. Then, using the results, a sustained load of 50% of the maximum peak load was applied for 10 days. Finally, the influence of fiber orientation on the pullout test under sustained loading with inclined fibers was investigated and correlated with the quasi-static pullout mechanisms already established in the literature. In addition, a four-parameter Burgers rheological model that correlates pullout displacement, apparent bond stress, and time is used to predict pullout behavior over time. Expressions to obtain the rheological model parameters as a function of fiber orientation are also proposed and can be applied to simulate the behavior of these composites in mesoscale models.

4.2. Experimental program

4.2.1. Materials

The materials used in this Chapter are the cement matrix described in the Section 3.2.1 and the three macro synthetic fibers studied so far and with their properties described in the Section 3.2.2.

4.2.2. Preparation of pullout samples

A mold was developed using a 3D printer, an updated version initially described in Rocha *et al.* [79] and in the Section 3.2.3. The mold has two symmetrical parts closed transversely by two screws at their ends. A lock was inserted at half the height of the test specimen to enable the fiber to be positioned before molding it. For this updated mold, a hole with a diameter slightly greater than that of the fiber was introduced for locking and centralization of the fiber. The hole position was defined to meet the desired fiber angles (15°, 30° and 45°). The printed pattern and fibers positioned for each orientation are shown in Figure 32.

The process of assembling and molding the printed mold can be seen in Rocha *et al*. [79] and in the Section 3.2.3. The mortar corresponding to the concrete described in section 3.2.1 was used, but without the gravel. The specimens were demolded 24 h later and kept in a controlled room (relative humidity of 50 ±5% and temperature of 20 ±1°C) until 28 days of age, when they were tested. Samples after demolding for each angle of inclination are shown in Figure 33.

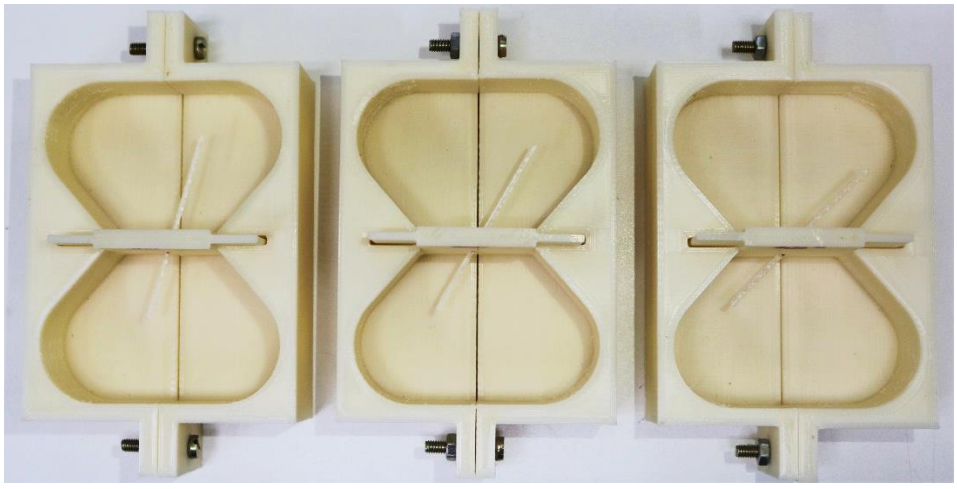

Figure 32. 3D printed pullout molds with fibers inclined to (a) 15°, (b) 30°, and (c) 45°.

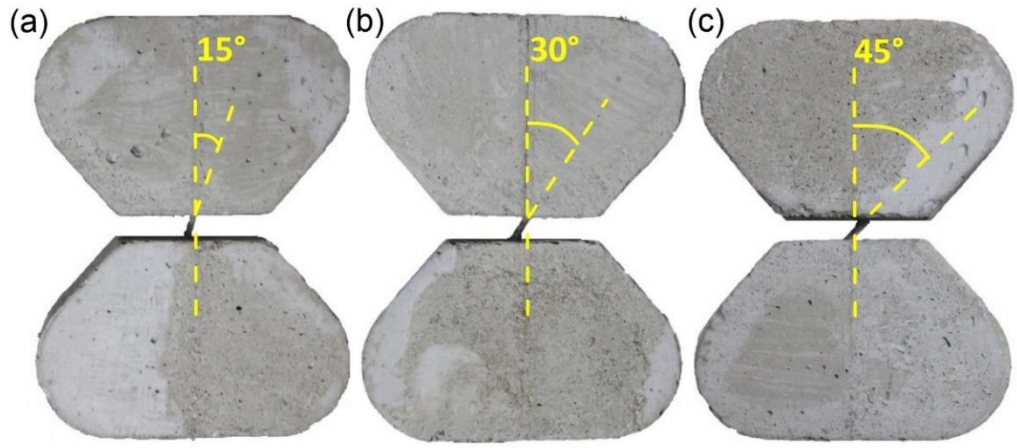

Figure 33. Specimen after demolding with fibers inclined to (a) 15°, (b) 30°, and (c) 45°.

4.2.3. Short-term single-fiber pullout test with inclined fibers

Pullout tests were performed to determine the pullout behavior of the fibers at different angles of inclination. The tests were carried out with a single fiber embedded on both sides of the specimen with an embedded length (L_c) of 20 mm. To ensure pullout on a critical side with a smaller interfacial area [24], an embedment length of 20 mm was adopted for the shortest side. This setup was designed so the concrete faces remained approximately parallel during the test.

Samples were inserted into specially designed grips and a displacement rate of 1.5 mm/min was adopted. The following were attached to the system: a 5 kN load cell and a linear vertical displacement transducer (LVDT) positioned on a base coupled to the grip to measure deformation during load application. Five specimens were tested for each of the three fibers and four angles. The experimental setup is shown in Figure 34 and the maximum shear stress (τ_{max}) was computed as equation (6) describes in section 3.2.4.

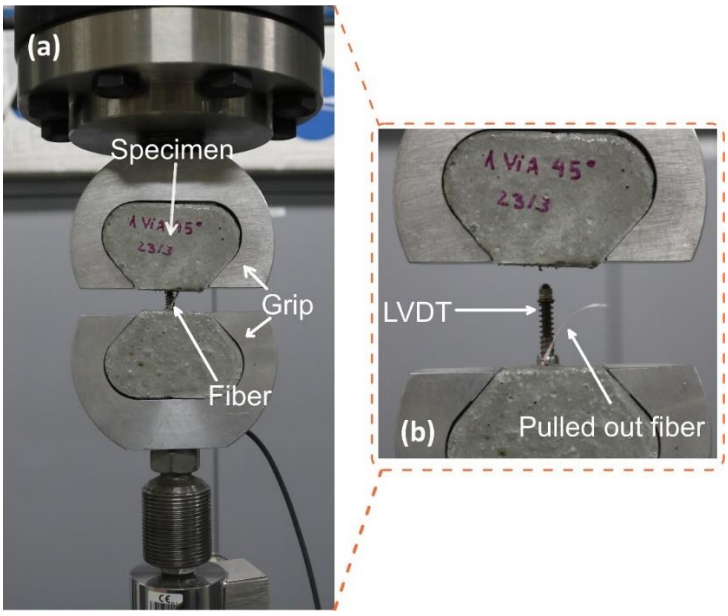

Figure 34. Details of the pullout test: (a) before and (b) after the test.

4.2.1. Single fiber pullout creep test setup with inclined fibers

To evaluate the pullout behavior under sustained load, an experimental setup was developed, as described in section 3.2.5. Generally, as the fiber was embedded on both sides of the sample, with the largest embedded side being 20 mm, the chosen solution was to fix the sample with a hook attached to each of its ends, where one side would be fixed to a rigid structure and therefore free from displacement, and at the other end a hook that allowed loading with suspended free weights. Care was taken to ensure alignment of the system and that both sides of the sample remained parallel, thus simulating the crack opening phenomenon. A steel plate was welded to the upper (fixed) hook, which held the sample and extended halfway to the lower (free) hook to restrict the rotation of the sample around the y-axis (indicated in Figure 35). An update to this setup was the insertion of two other plates welded to the system to prevent the sample from translating around the x and z-axis (both indicated in the Figure 35-a). The bottom slides through a tongue-and-groove fitting. The plates and the clamp that held the sample, which were in direct contact, had their contact surfaces sanded and lubricated with oil to reduce friction. Details of the proposed experimental setup are shown in Figure 35. Data was acquired automatically with an HBM 1615 at a frequency of 0.02 Hz. The weights were placed gradually to avoid dynamic overload and to achieve the final load within 5 min.

The tests were conducted in a controlled room (temperature of 20 ±1 °C and relative humidity of 50 ±5%). Three samples for each selected angle were tested at 50% of the average maximum load evaluated in the short-term pullout tests (Table 9). The samples remained loaded for 10 days, when loads were removed. Unfortunately, this setup could not efficiently measure recovery after unloading due to instability issues (pendulum behavior).

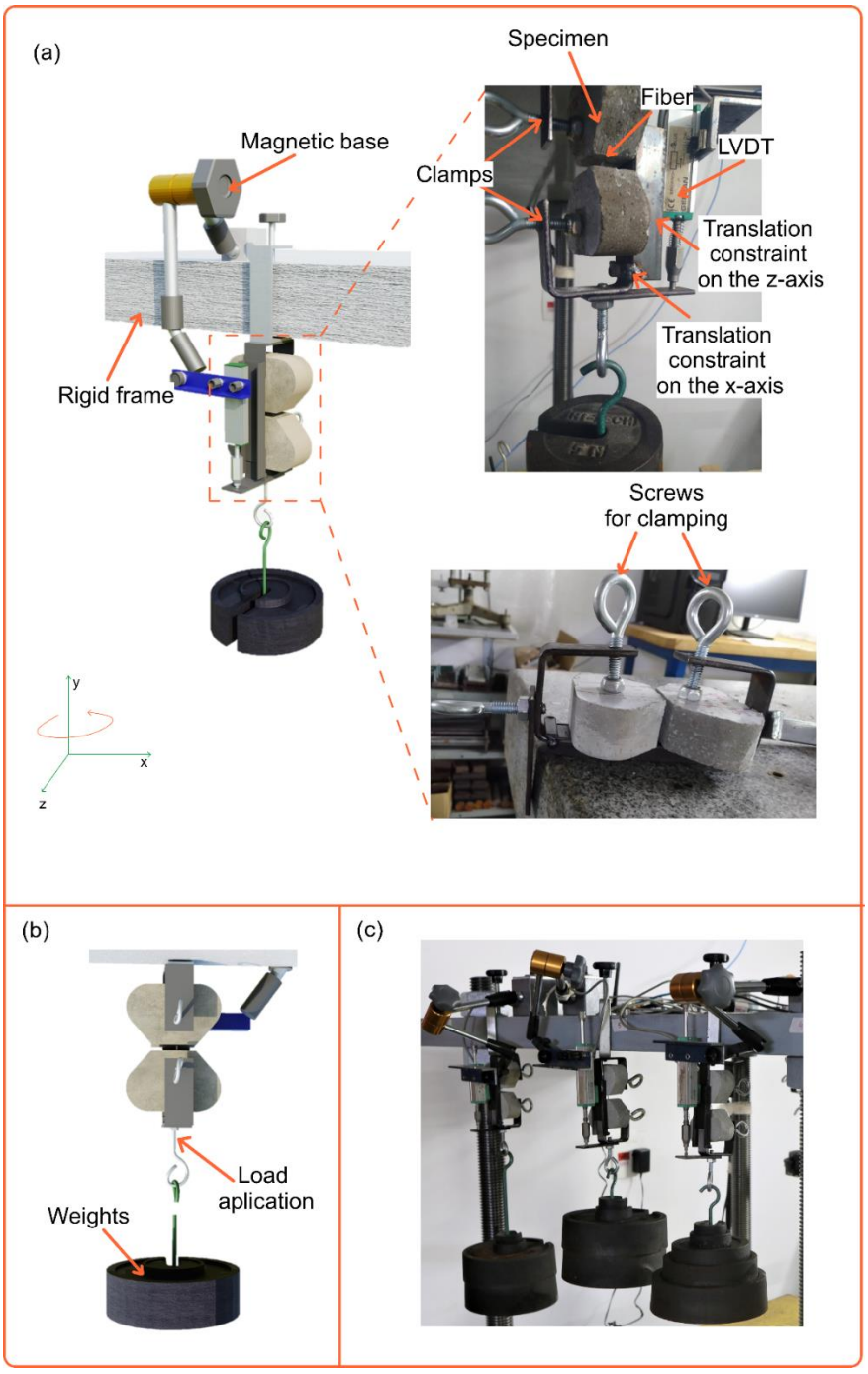

Figure 35. (a) Schematic with the proposed creep experimental setup and real images of the details; (b) Schematic of the arrangement of the weights suspended in the claws attached to the lower end of the sample; (c) image of the actual test in progress.

4.3. Results and discussion

4.3.1. Short-term single fiber pullout test with inclined fibers

Figure 36, Figure 37 and Figure 38 show the pullout curves for the type of fibers and angles investigated at the same specified embedment length of 20 mm. As the LVDT used had a 10 mm full range, the curves show the displacements up to this value. However, the pullout tests were performed until failure or when the fibers were fully pulled out. Each curve represents the mean response of each group, whereas the grey shade represents the envelope of results. Table 9 summarizes the mean values of the real embedment length (measured after casting one side due to small variations from the pre-established 20 mm, as explained in section 4.2.2), maximum load (P_{max}) and bond stress (τ_{max}), along with their corresponding standard deviations. A significant variation was observed, which may be explained by small changes in the embedded lengths due to vibration and manual insertion of the fibers. The inclined fibers had embedded lengths exceeding the initially specified 20 mm.

Increasing the angle of inclination (θ) of the fibers about the direction of the load significantly influences the maximum load (P_{max}), slip at the peak load, and probability of fiber rupture before pullout. For *BF* fibers, an increase of 13.4% and 12.4% in P_{max} was found for angles of 15° and 30°, respectively; for *TF* fibers, a 5.1% increase in P_{max} was observed for the 15° angle. However, as the embedded lengths varied, a comparison in terms of the maximum shear stresses (τ_{max}) was necessary for reliability. Therefore, the values of the angle of inclination (θ) versus the maximum shear stresses (τ_{max}) for all fibers are plotted in Figure 39. In this case, none of the fibers experienced higher τ_{max} mean values than those from the results of the fibers at 0° as reported by Rocha *et al.* [79] and describes on Section 3.3.1. Moreover, with an increase in the angle of inclination, the efficiency of this behavior and the pullout resistance were reduced. Although different angles of inclination were tested, the shapes of the curves are similar with only minor variations. Considering the standard deviation, small differences of τ_{max} were observed for all the tested angles, especially for *VF* fiber. During the pullout test, when the bond had already been lost, the frictional resistance mechanism was mobilized, generating an upward pressure in the matrix around the exit point, increasing the friction and consequently the force necessary to pullout the fiber [34,74]. This additional resistance to the pullout force can compensate for the

reduced efficiency when considering only the angle of inclination [69,73], resulting in not pronounced changes in τ_{max}.

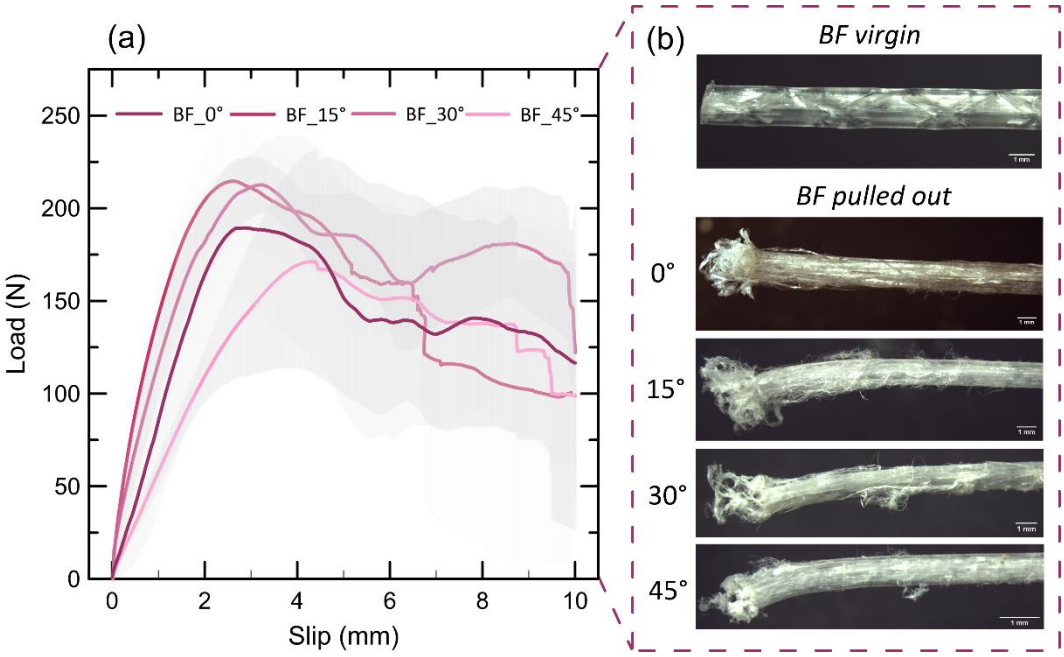

Figure 36. (a) Load *versus* slip curve of *BF* fiber pullout test at 0°, 15°, 30°, and 45° angles; (b) optical microscopy images of the fibers after pulling out at the different tested angles.

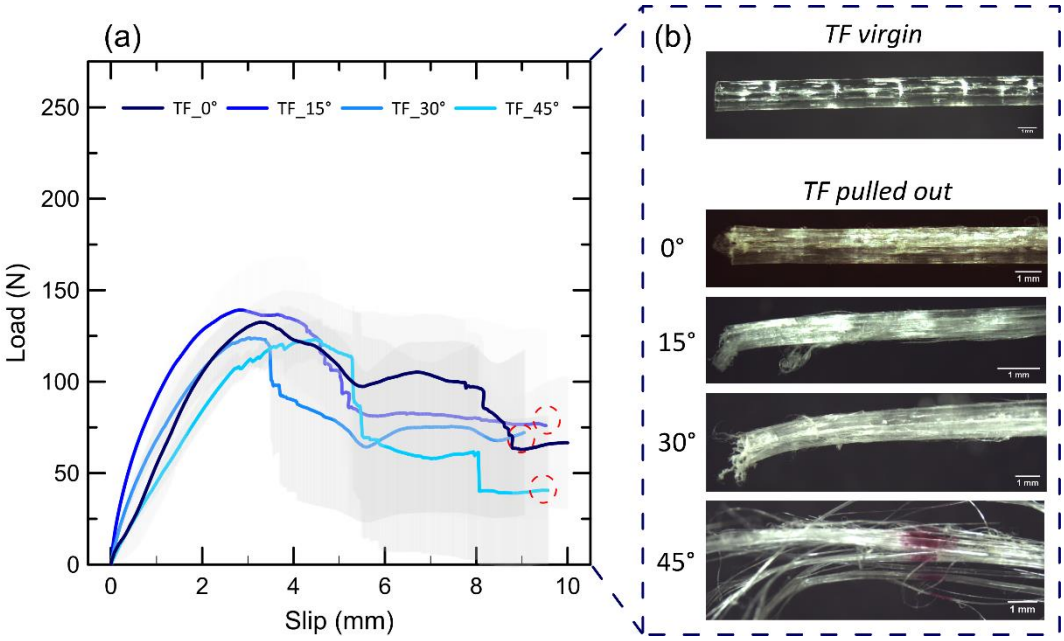

Figure 37. (a) Load *versus* slip curve of *TF* fiber pullout test at 0°, 15°, 30°, and 45° angles; (b) optical microscopy images of the fibers after pulling out at the different tested angles.

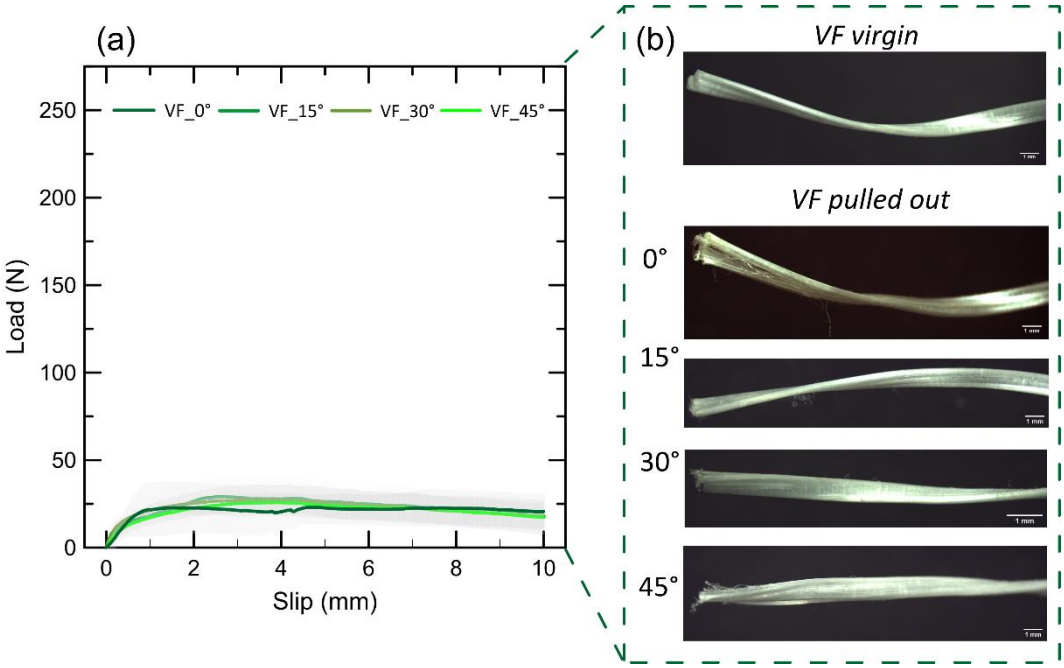

Figure 38. (a) Load *versus* slip curve of the *VF* fiber pullout test at 0°, 15°, 30°, and 45° angles; (b) optical microscopy images of the fibers after pulling out at the different tested angles.

Table 9. Pullout test parameters.

Fiber type	*Embedment length (mm)*	*Slip at peak load (mm)*	P_{max} *(N)*	τ_{max} *(MPa)*
BF_0°	19.3 ±0.829	2.85 ± 2.8x10^{-5}	189.4 ± *36.8*	3.85 ±0.917
BF_15°	24.3 ±1.49	2.64 ± 0.009	214.6 ± 28.1	3.33 ±0.528
BF_30°	23.5 ±1.35	3.23 ± 0.009	212.6 ± 14.2	3.36 ±0.228
BF_45°	24.8 ±0.37	4.35 ± 0.006	171.3 ± 59.6	2.63±0.719
TF_0°	20.5 ±1.47	3.28 ± 7.5x10^{-5}	132.5 ± 11.5	2.66 ±0.378
TF_15°	24 ±1.43	2.83 ± 0.005	139.2 ± 20.4	2.34 ±0.261
TF_30°	25.1 ±1.39	3.03 ± 0.005	124.1 ± 15.6	1.96 ±0.324
TF_45°	23.6 ±1.86	4.48 ± 0.007	123 ± 10.1	2.13 ±0.283
VF_0°	21.1 ±1.24	1.45 ± 3.6x10^{-5}	22.7 ±14.6	0.559 ±0.132
VF_15°	28.5 ±0.253	2.59 ± 0.009	29.2 ± 10.5	0.414 ±0.133
VF_30°	25.6 ±0.752	3.61 ± 0.008	27.4 ± 8.18	0.447 ±0.11
VF_45°	22.4 ±0.786	3.83 ± 0.009	25.7 ± 4.94	0.467 ±0.081

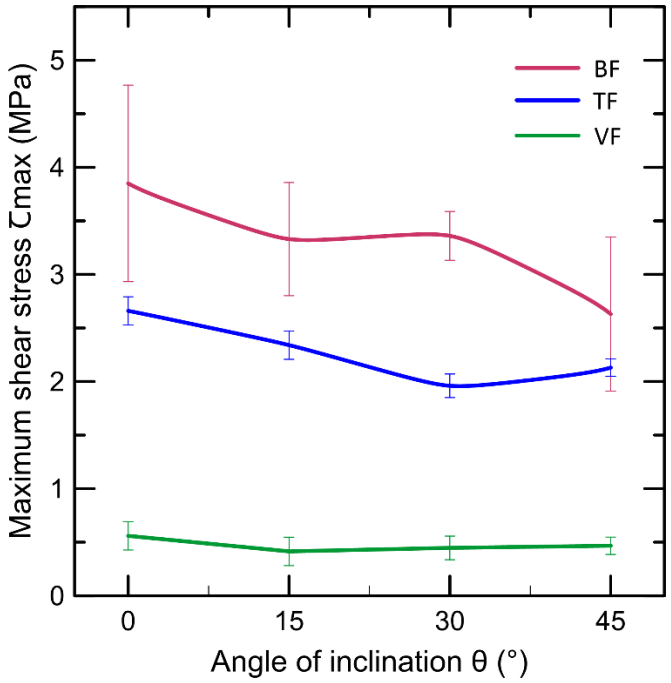

Figure 39. Fiber inclination angles *versus* maximum shear stresses for all fibers studied.

Localized pressure (snubbing effect) when θ ≠ 0 can cause plastic deformations in fibers and matrix fragmentation depending on the properties of the matrix and fiber stiffness [34,73]. When the fibers were completely pulled out, as the angle increased, fibers that were originally straight (*BF* and *TF*) exhibited a more curved shape, whereas the twisted (*VF*) ones became straighter, as shown in the optical microscopy images of the fibers after the pullout (Figure 36-b, Figure 37-b, and Figure 38-b). According to Robins *et al*. [23], provided the final tensile strength of the fiber is not reached during the test, an increase in θ will increase the tortuosity of the path along which the fiber is pulled, leading to a higher resistance to straightening and, therefore, an increase in τ_{max}. For *VF* fibers, although for all inclinations the value of τ_{max} was lower than that of the fiber at 0°, a progressive increase in τ_{max} occurred with increasing θ, reaching its maximum value at θ = 45°. Notably, the greater the value of θ, the greater the orientation of the *VF* fibers, which were initially twisted. At θ = 45°, the tortuosity of the pullout tunnel increased the shear stress by causing an alignment of the fibers. All these fibers were pulled out, with minimal fiber damage other than straightening. However, for straight fibers and with a corrugated surface (*BF* and *TF*), the angle of inclination increased fiber degradation, reducing its strength and favoring rupture, as reported by Li *et al*. [73] and Kanda and Li [80]. Notably, in the case of synthetic fibers, their surface abrasion during pulling is one of the phenomena responsible for the slip-hardening behavior of these fibers, promoted by the

increase in shear stress as the slip occurs. Thus, the more degraded the fiber, the greater the peak load in the stress versus slip diagram [69,73,81,82]. Furthermore, the mechanical component represented by the snubbing effect is responsible for reducing the variability of the results, although high variability will always exist in the evaluation of the fiber-matrix interface.

Fiber rupture was observed in one of the *BF*_0°, *BF*_30°, *BF*_45°, and *TF*_0° samples, two of the *BF*_15° samples, three of the *TF*_15° and *TF*_30° samples, and all the *TF*_45° samples. The fiber failure mode initially occurred with the consecutive rupture of the fiber's monofilaments until they could not resist pulling and broke, as reported by Deng *et al.* [81]. The ruptures observed were generally at fiber points initially embedded and for slippage close to or greater than 10 mm, as shown in Figure 37. The increase in fiber degradation and the probability of rupture of these fibers (*BF* and *TF*) can be explained by their corrugated surfaces that favor stronger matrix bond and, in the case of inclined fibers, induce higher localized stresses at the exit point than those of straight fibers. All the *TF*_45° fibers (P_{max}= 123 N; τ_{max}= 2.13 MPa) failed after reaching the maximum load but still exhibited a better performance in terms of bond stress than the *TF*_30° fibers P_{max}= 124.1 N; τ_{max}= 1.96 MPa), most likely owing to the combined effect of snubbing and fiber bending, resulting in exacerbated degradation of the fiber when pulled at this angle of inclination and consequently, premature rupture.

Small matrix fragmentations were observed, especially for fibers inclined at 30° and 45°. The response of the matrix to local bending stresses also influences the general efficiency of the fiber orientation, given that fragmentation will occur if the stresses exceed the tensile strength of the concrete matrix [15]. As the matrix had a compressive strength of 47 MPa and the tensile strength increased with the compressive strength, the disintegration of the exit point portion of the fiber was not as evident as it would have been in a weaker matrix or for a high modulus fiber such as steel.

Regarding the slip experienced at the point of maximum load, in the *BF* and *TF* fibers with angles of 15° (*BF* = 2.64 mm; *TF* = 2.83 mm) and 30° (*BF* = 3.23 mm; *TF* = 3.03 mm), accelerated slip occurred compared with fibers at 0° (*BF* = 2.85 mm; *TF* = 3.28 mm), whereas the slip was reduced at θ = 45° (*BF* = 4.35 mm; *TF* = 4.48 mm. In *VF* fibers, a behavior similar from that reported for steel fibers [83–86], which exhibit greater slip with an increase in the inclination angle. Particularly, for *BF* fibers, which have slightly higher moduli of elasticity than *TF* fibers and demonstrate better bond to the matrix in the samples at 0°, the slope of the stress versus slip curve increased for angles of 15° and 30°, with a reduction

in the slip at the peak load. According to Li *et al*. [69], the friction caused by both the normal force and relative movement between the fiber and matrix can be illustrated as a tensioned fiber attached to a virtual cylinder, similar to changes in direction in fibers with modified geometry, resulting in higher pullout resistance and toughness. The inclination of the fiber can increase the slopes of the load-slip curves in the ascending branch and improve the maximum pullout load and the corresponding slip [87]. As *VF* fibers are straight and have a weaker matrix bond, the considerable alignment experienced when pulled out may increase the slope of the curve and, consequently, reduce the slip at the maximum load point. This effect is observed by the increase in bond tension as the angle of inclination increases, although still lower than that experienced at the 0° angle.

4.3.2. Single fiber pullout creep test with inclined fibers

Polymeric fibers exhibit a considerable tendency to strain over time, even under room temperature, which can be a challenge for structural applications. Plots of the slip against loading time are shown in Figure 40, Figure 41 and Figure 42. The curves in (a) show the mean values of the three curves for each angle, whereas those in (b) show the mean values of the creep coefficient for each angle, defined as equation (7) describes in section 3.3.2. For the ages of 3, 7, and 10 days, these parameters for the three types of fiber and the standard deviation are summarized in Table 10.

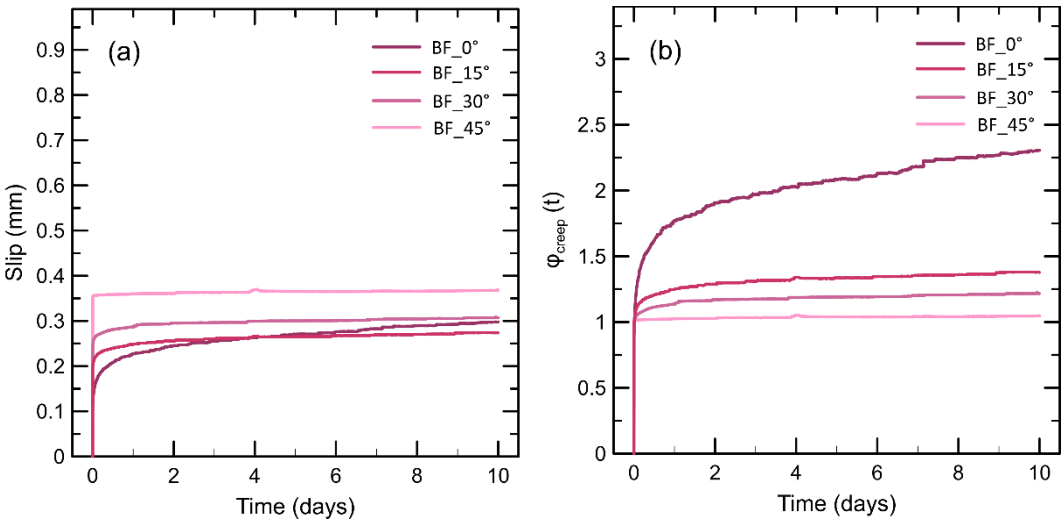

Figure 40. (a) Slip *versus* time curves of *BF* fiber for different inclinations; (b) creep coefficient ($\varphi_{creep}\ (t)$) over time for all inclinations.

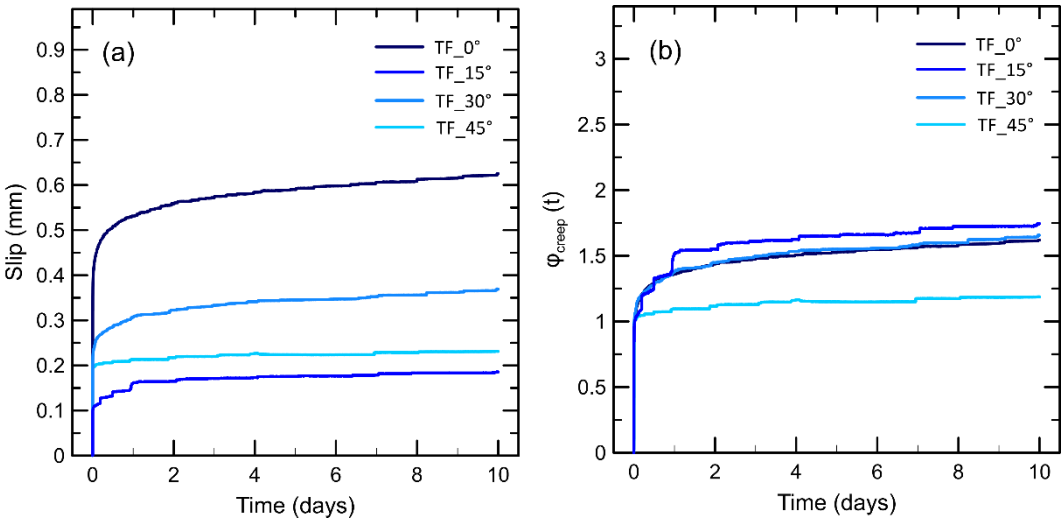

Figure 41. (a) Slip *versus* time curves of *TF* fiber for different inclinations; (b) creep coefficient ($\varphi_{creep}\ (t)$) over time for all inclinations.

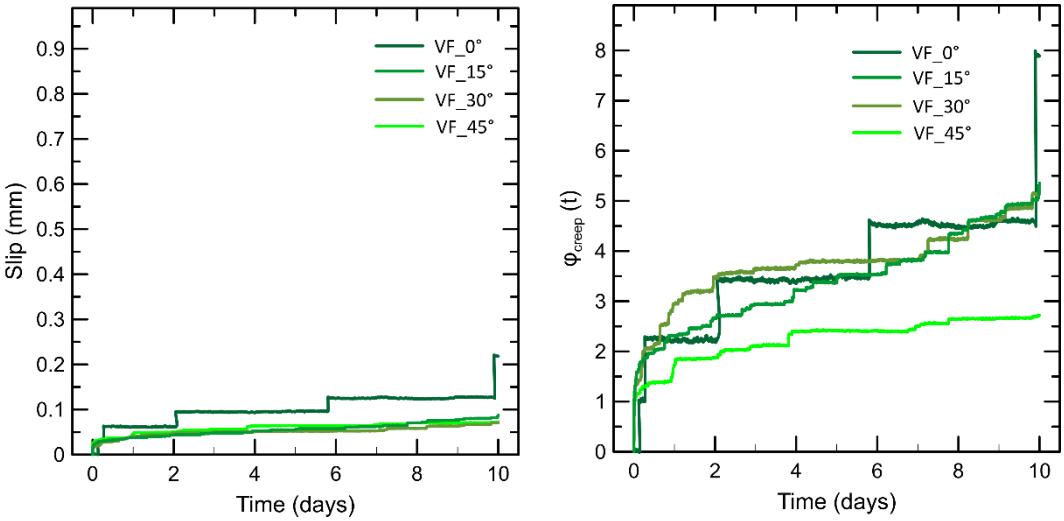

Figure 42. (a) Slip *versus* time curves of *VF* fiber for different inclinations; (b) creep coefficient ($\varphi_{creep}\ (t)$) over time for all inclinations. **Note the different creep coefficient scale, compared to the same graphs of the other fibers studied.

Table 10. Summary of instantaneous displacements and creep coefficients at ages 3, 7 and 10 days for all samples tested at pullout under sustained load.

Fiber type	δ_{inst} *(mm)*	φ_{creep}		
		3 days	*7 days*	*10 days*
BF_0°	*0.127 ±0.064*	*1.97 ±0.174*	*2.18 ±0.213*	*2.31 ±0.191*
BF_15°	*0.199 ±0.133*	*1.23 ±0.176*	*1.26 ±0.207*	*1.28 ±0.209*
BF_30°	*0.252 ±0.033*	*1.18 ±0.074*	*1.21 ±0.101*	*1.22 ±0.106*
BF_45°	*0.351 ±0.102*	*1.04 ±0.02*	*1.04 ±0.031*	*1.05 ±0.035*
TF_0°	*0.396 ±0.139*	*1.49 ±0.226*	*1.59 ±0.275*	*1.64 ±0.287*
TF_15°	*0.106 ±0.091*	*2.26 ±1.25*	*2.4 ±1.35*	*2.53 ±1.48*
TF_30°	*0.223 ±0.031*	*1.52 ±0.266*	*1.61 ±0.343*	*1.69 ±0.335*
TF_45°	*0.195 ±0.088*	*1.24 ±0.39*	*1.33 ±0.541*	*1.36 ±0.586*
VF_0°	*0.027 ±0.08*	*3.43*[a]	4.53 [a]	7.89 [a]
VF_15°	*0.016 ±0.003*	*2.98 ±0.532*	*3.84 ±0.515*	*5.19 ±1.28*
VF_30°	*0.014 ±0.016*	*3.38 ±1.14*	*3.87 ±1.31*	*5.53 ±0.528*
VF_45°	*0.027 ±0.007*	*2.16 ±0.281*	*2.67 ±0.856*	*2.92 ±1.13*

[a] *No standard deviation as only one sample reached age without breaking.*

For inclined fibers, as shown in the Figure 43, the matrix wedge on the pullout surface exerts a normal force N to allow the axial force on the fiber to change its direction [69], in other words, the friction generated at the fiber exit mitigate the stress existing in the embedded part and the creep can be basically attributed to the creep of the free length. However, when these fibers are arranged at 0°, only a direct pull is applied, with no bending. Therefore, the results demonstrate that fibers arranged at 0° are more likely to be pulled out under a long-term load than inclined fibers, since a good part of the embedded fiber also suffers creep, along with the interface. This behavior was also observed by Abrishambaf *et al.* [88], but for steel fibers. According to the creep coefficient graphs in Figure 40 to Figure 42, as the inclined angle increases, a lower creep rate is experienced due to the reduction in the creep portions relating to fiber creep in the embedded length and interface creep. When θ = 45°, for all fibers, it can be believed that the existing creep is basically the creep of the fiber itself. As the creep of the fiber is the primary deformation mechanism of composites reinforced with macro synthetic fibers under sustained load [14,15], available through pullout tests with straight fibers to lead to greater deformations over time.

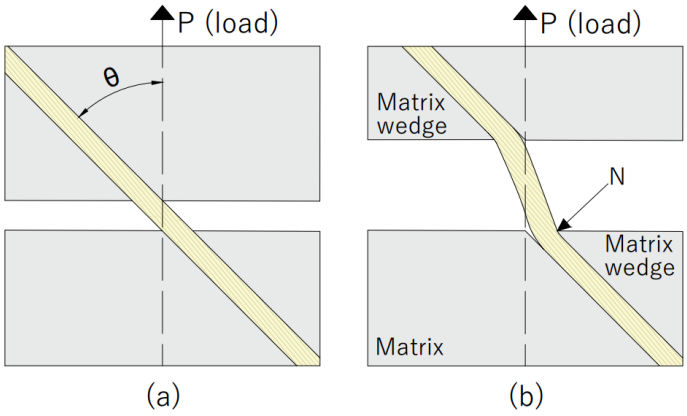

Figure 43. Schematic drawing of the inclined fiber inserted into the cementitious matrix (a) before the load is applied and (b) during pullout.

All the samples exhibited an instantaneous initial displacement (δ_{inst}) as soon as the load was applied due to the elongation of the fiber along the free length [14] and initial pullout. This initial displacement seems dependent on the type and properties of the fiber [14] in addition to the applied load. Because the applied loads are different for each angle, the most interesting comparison of δ_{inst} would be through the initial stiffness given by $K = {\delta_{inst}}/{P}$ (Figure 44). For *BF* fibers, a pattern can be observed with K increasing with angle, possibly resulting from its greater bending stiffness. A different response was observed for *TF* and *VF* fibers, which experienced an initial reduction of stiffness with θ, followed by an increase for θ = 30° and 45°.

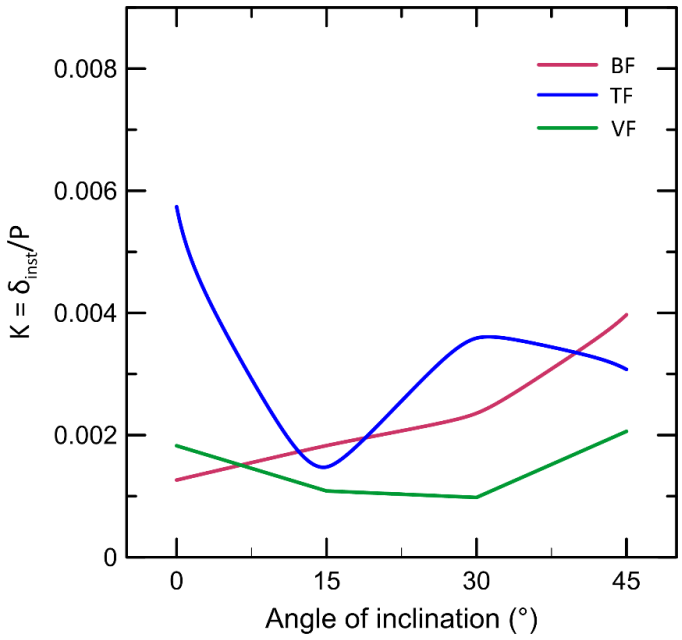

Figure 44. Initial stiffness *versus* fiber inclination angle.

For *BF* and *TF* fibers, the creep coefficient ($\varphi_{creep}\,(t)$) increases over time for all the analyzed angles, although at a decreasing rate. Incidentally, *BF* fibers (15°, 30°, and 45°) exhibit almost no difference between the 7- and 10-day tests, appearing to have reached the slip limit. In *BF* and *TF* fibers, $\varphi_{creep}\,(t)$ decreases as the angle θ increases, as show in the Figure 45. *BF* fibers exhibit a significant increase in slippage over time when the fibers are aligned with the direction of the load, i.e., θ = 0°. This is justified by the fact that inclined fibers basically have the creep resulting from the creep of the fiber in the free length and aligned fibers have other slip components over time, as already explained and shown in the Figure 43. As for *TF* fibers, this significant difference is only noticed when the angle is 45°.

VF fibers presented a low instantaneous initial displacement for all the angles investigated, although with a significantly higher creep growth rate than those of the other fibers, indicating that the slip continues to increase over time, justified by their smooth surfaces, which offer a lower pullout resistance than those of other fibers that have a superficial corrugation. Importantly, in the 10-day test, the creep coefficient is higher than in the 7-day test, indicating that the pullout is progressing. This shows that these fibers are so easily deformable that the deflection components caused by the change of direction at small inclination angles do not offer great resistance to slipping over time, to the point that the only significant creep is attributed to creep in the fiber itself, except for angles greater than 45°. Only one of the *VF*_0° fiber samples remained intact during the 10-day test, with all the others ruptured in less than 48 h, as explained in Section 3.3.2.

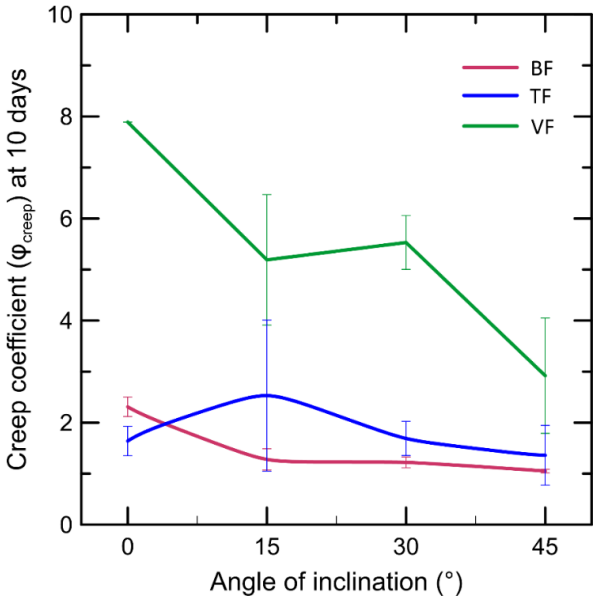

Figure 45. Creep coefficient at 10 days *versus* fiber inclination angle.

As the change in fiber inclination plays an important role, evaluation of viscoelastic behavior over time is performed by applying a four-parameter rheological Burgers model. The original equation correlates strain, stress and time, which will be replaced by pullout displacement, apparent bond stress and time as equation describes in section 3.3.2 as equation (8).

Table 11 presents the model parameters for all angles and fiber evaluated, which were obtained through regression of the mean experimental pullout curves under sustained load. The correlation coefficient R^2 is also reported for each analysis in order to prove the fit to the experimental curves. A comparison of the experimental curves and models for the three types of fibers and all the inclination angles are shown in Figure 46 to Figure 48.

Table 11. Burgers model parameters for the three fibers and all their inclinations.

Fiber type	*Loading level*	*Burgers model parameters*				*R^2*
		R_1 (MPa/mm)	*R_2 (MPa/mm)*	*η_1 (MPa.s/mm)*	*η_2 (MPa.s/mm)*	
BF	0°	13.1	22.5	2.37×10^7	8.59×10^5	0.99
	15°	7.65	44.7	7.12×10^7	2.45×10^6	0.99
	30°	6.45	53	9.18×10^7	2.32×10^6	0.99
	45°	3.93	51.7	1.36×10^8	1.23×10^4	0.76
TF	0°	3.07	11.3	1.53×10^7	5.96×10^5	0.99
	15°	11.2	18.8	5.19×10^7	1.04×10^6	0.98
	30°	3.99	13.6	1.59×10^7	7.91×10^5	0.99
	45°	5.34	57.9	6.81×10^7	5.43×10^6	0.96
VF	0°	8	20	2.16×10^6	1.35×10^5	0.79
	15°	13.1	12.8	3.55×10^6	1.23×10^5	0.98
	30°	18.3	7.31	6.47×10^6	2.48×10^5	0.87
	45°	8.14	8.53	1.25×10^7	1.19×10^6	0.97

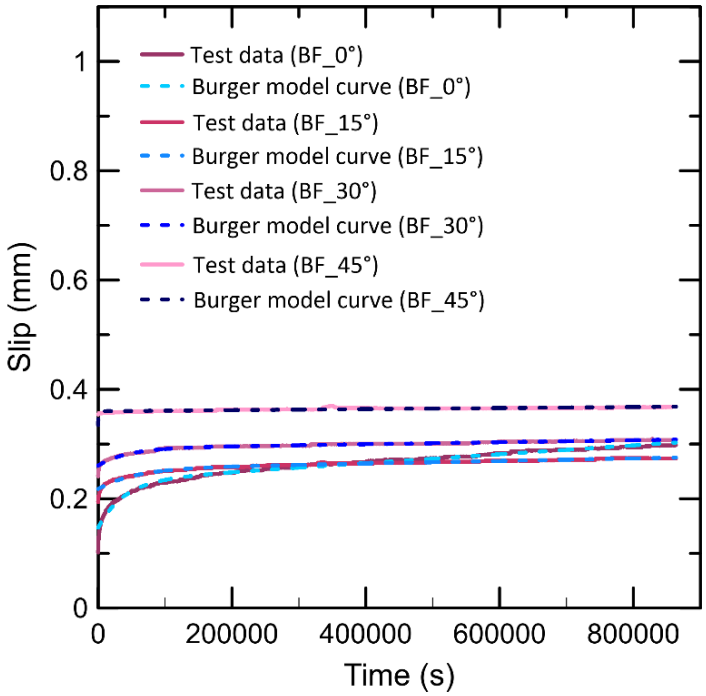

Figure 46. Experimental curves and rheological results of the Burgers model for the *BF* fiber.

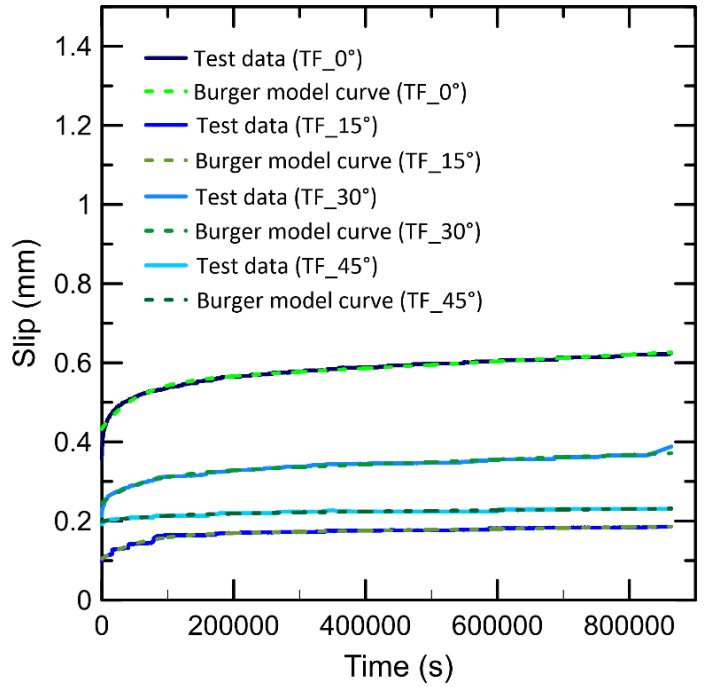

Figure 47. Experimental curves and rheological results of the Burgers model for the *TF* fiber.

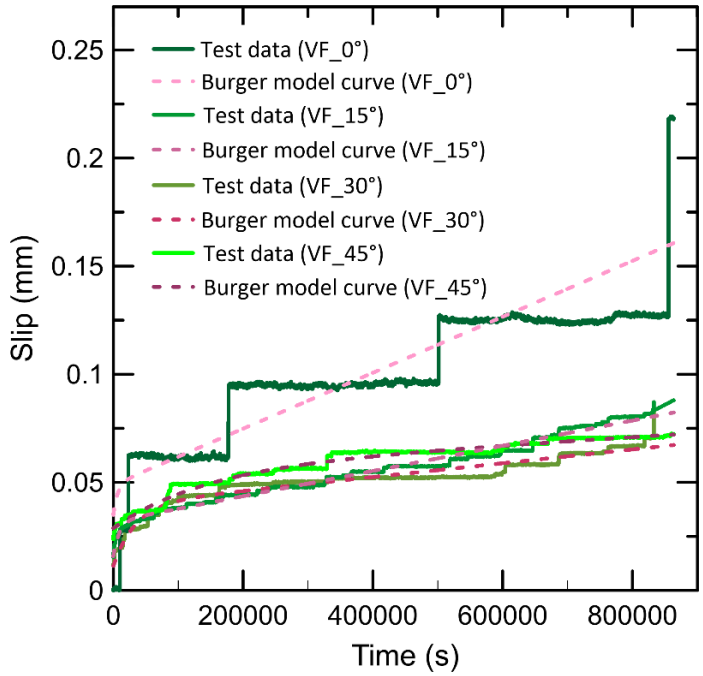

Figure 48. Experimental curves and rheological results of the Burgers model for the *VF* fiber.

A correlation coefficient greater than 0.75 was obtained for all angles of inclination, demonstrating a good fit for the model. The bond stiffness, represented by the parameter R_1, seemed to decrease as the angle increased for *BF* fibers (41.6% for 15°, 50.8% for 30°, and 70% for 45°) but increased for *TF* (259% for 15°, 30% for 30°, and 74% for 45°) and *VF* fibers (63.8% for 15°, 128.8% for 30°, and 1.8% for 45°). As the *BF* fiber has a slightly higher modulus of elasticity than the others, this reduction in stiffness may have been caused by the lateral bending of the fiber. Conversely, for *VF* fibers, the stiffening may have been promoted by the straightening process during the pullout.

In the case of the η_1 parameter, which represents the secondary creep rate, an increase in θ generated higher values of η_1 in all fibers, indicating a reduction in slip over time. As already discussed, the alignment of the fibers can favor the progression of the pullout.

The parameter η_2 regulates the speed with which the curve enters the secondary creep stage, i.e., the smaller the η_2, the faster the curve enters the secondary stage. For *BF* and *TF* fibers, an increase in η_2 was observed from 0° to 15° and then a decrease for angles of 30° and 45°. The interspersing of *VF* fibers increases with reductions. Generally, longer periods of primary creep were observed for all angles compared with their fibers at 0°, except for *BF* fibers at 45°.

Given the good fit of the curves to the Burger model, equations were proposed that represent each of its parameters ($\boldsymbol{R_1}$, $\boldsymbol{R_2}$, $\boldsymbol{\eta_1}$, $\boldsymbol{\eta_2}$) as a function of the angle θ for each fiber studied, as shown in Table 12. The functions are 2nd degree polynomials (with the exception of the coefficients $\boldsymbol{R_1}$ and $\boldsymbol{\eta_1}$ for the *TF* fiber which were better adjusted to 3rd degree polynomials) and allow you to define the parameters for any inclination angle between 0° and 45°. The vast majority of equations presented an excellent fit and can be used to feed numerical models to predict the long-term behavior of these composites.

The application of the Burgers model does not allow the separation of mechanisms, such as the snubbing effect, but represents the phenomenon globally. In the case of inclined fibers, the consideration made is that the fiber would be perpendicular to the crack surface, giving an equivalent response.

Table 12. Approximating equations of the parameters of the Burgers model as a function of the angle θ (for 0 < θ < 45°, θ in degrees) and the coefficient of correlation R^2.

Fiber type	*Equations*	*R^2*
BF	$R_1(\theta) = 0.003\theta^2 - 0.338\theta + 12.8 \quad (MPa/mm)$	0.966
	$R_2(\theta) = -0.026\theta^2 + 1.81\theta + 22.7 \quad (MPa/mm)$	0.999
	$\eta_1(\theta) = -3801\theta^2 + 3 \times 10^6\theta + 3 \times 10^7 \quad (MPa.s/mm)$	0.981
	$\eta_2(\theta) = -4329.6\theta^2 + 177078\theta + 835168 \quad (MPa.s/mm)$	0.997
TF	$R_1(\theta) = 0.001\theta^3 - 0.087\theta^2 + 1.58\theta + 3.07 \quad (MPa/mm)$	1.0
	$R_2(\theta) = 0.041\theta^2 - 0.936\theta + 14.3 \quad (MPa/mm)$	0.865
	$\eta_1(\theta) = 7941.8\theta^3 - 518667\theta^2 + 8x10^6\theta + 2 \times 10^7 \quad (MPa.s/mm)$	1.0
	$\eta_2(\theta) = 4667.1\theta^2 - 114934\theta + 874844 \quad (MPa.s/mm)$	0.904
VF	$R_1(\theta) = -0.017\theta^2 + 0.801\theta + 7.23 \quad (MPa/mm)$	0.833
	$R_2(\theta) = 0.009\theta^2 - 0.687\theta + 20.3 \quad (MPa/mm)$	0.987
	$\eta_1(\theta) = 5182.7\theta^2 - 6391.8\theta + 2 \times 10^6 \quad (MPa.s/mm)$	0.998
	$\eta_2(\theta) = 1059.1\theta^2 - 25755\theta + 168879 \quad (MPa.s/mm)$	0.971

4.4. Conclusions

Short- and long-term pullout tests were performed with angles of 15°, 20°, 30°, and 45° with respect to the direction of the load to investigate the influence of macro synthetic fibers orientation on fiber–matrix interactions. The following conclusions were drawn:

1. The embedded lengths were greater in the samples with inclined fibers. In the short-term tests, a comparison in terms of shear stress instead of the maximum pullout load revealed that in none of the fibers did the bonding stress exceed that experienced when the fibers were aligned with the direction of the load, even with minimal variation, especially for angles of approximately 30°.
2. Significant fiber surface degradation was observed as the angle of inclination was increased. In the specific case of twisted fibers (*VF*), they were practically aligned after the pullout. The tortuosity of the path in the pulling tunnel seems to have been responsible for this alignment, in addition to the increased slope of the tension versus slip curve for these fibers, considering the substantial challenge in pulling them out, when compared with the aligned samples.
3. Straight fibers and those with superficial corrugation (*BF* and *TF*) exhibited greater adherence to the matrix. Moreover, in the case of inclined samples, a greater probability of fiber rupture was observed. This behavior was attributed to their corrugated surfaces, which favored matrix bonds and induced even greater localized stresses than those due to the snubbing effect at the exit point, promoting an exacerbated degradation of the fiber and thus resulting in the rupture of some samples. This rupture was observed in all *TF* fibers inclined at 45°. Minimal fragmentation of the matrix was observed, possibly due to the low stiffness of the fiber compared with that of the matrix.
4. For straight fibers (*BF* and *TF*) the creep coefficient was reduced with an increase in the fiber inclination angle. Furthermore, an almost zero growth rate was obtained for the 10-day test compared with the 7-day test, indicating no further slippage. However, *VF* fibers increasingly deformed over time, possibly owing to the lower resistance imposed by their smooth surface.
5. The creep reduction with an increase in the fiber inclination angle could be explained by the snubbing effect that induced force components to promote axial force deviation, in addition to the reduction of fiber creep, which under inclined loading, reduced its capacity to deform. Given this, the greater the inclination angle, the lower the creep rate will be, as the portions relating to the fiber creep in the embedded length and the interface creep are severely reduced, leaving basically the fiber creep in the free length.

6. In long-term pullout tests, fibers with surface corrugation (*BF* and *TF*) had their sliding almost ceased after 7 days, which suggests that this is a sliding limit. However, the *VF* fibers continued to slide with a significant creep growth rate, possibly justified by their smooth surface and low adhesion to the matrix.
7. The Burgers model was applied to the experimental curves and resulted in a good fit for all the fibers and angles of inclination. Due to this good fit, approximate functions of the parameters were determined and these can be used to model fiber-scale cementitious composites.

5. SINGLE-FIBER TENSILE BEHAVIOR AND ANALYTICAL MODEL OF PULLOUT CREEP BEHAVIOR IN MACRO SYNTHETIC FIBERS

5.1. Introduction

Sustained load pullout tests are commonly used to evaluate the strength of the fiber-matrix interface. However, when polymeric fibers are used, the deformation of the fiber itself can be interpreted as slippage upon pullout because they undergo significant elongation under a sustained load. Several studies have conducted creep pullout tests on macro synthetic fibers [3,7,14,15,36] and concluded that much of the measured pullout was due to fiber deformation [3,14,15,79]. This was justified by imaging tests, such as microtomography [14,79] and scanning electron microscopy [79], where small displacements or no displacement at the fiber tip were observed, in addition to ensuring that the interface was apparently intact in some cases. The distribution of shear stresses at the interface is known to be nonlinear along the length embedded in the cement matrix [89]; the greater the modification of its surface and/or fiber geometry, the less uniform this distribution will be before extraction [38]. Therefore, the lack of tip slip does not exclude the existence of slip. Furthermore, forces are transferred from the fiber to the matrix relatively quickly, and the creep of the fiber is not reflected in the entire length but only in a small part.

Although it has been reported that a portion of the slip measured in pullout under sustained load is due to stretching of the fiber itself [3,14,15,79], the separation of the fiber and interface contributions to the pullout has not yet been realized. A possible way to separate these portions is through analytical models that investigate the fiber-matrix adhesion properties, most of which are based on the analysis of shear stresses at the interface [26,90–94]. However, applying a model implies greater knowledge of the fiber behavior.

The pullout behaviors of the three macro synthetic fibers for different loading percentages and inclination angles in relation to the loading direction are discussed in Chapters 3 and 4. This chapter seeks to experimentally study the macro synthetic fibers used in short- and long-term tensile tests, in addition to Fourier-transform infrared spectroscopy (FTIR) tests, and analytically through a simplified analytical model. In this model, the results obtained in the pullout and fiber tensile

tests were applied, and the crack opening was assumed for short- and long-term loads to compare the stiffness of the fiber-matrix interface. Despite the problem's complexity, the intention was to simplify the interface response during pullout under short- and long-term loads.

5.2. Experimental program

The short- and long-term pullout behaviors of cementitious matrices reinforced with polymeric macro fibers were studied with fibers aligned in the loading direction in Chapter 3 and with inclined fibers in Chapter 4. In this experimental program, only the pure fibers were examined through physical characterization and short- and long-term tensile tests.

5.2.1. Direct tensile test

To mechanically characterize the fibers and obtain their stress *versus* strain curves, direct tensile tests were performed according to the ASTM C1557-20 standard guidelines [95]. A modified version of the test arrangement was developed, and the option that presented the best results consisted of fixing the fiber with epoxy adhesive glue to a galvanized steel sheet, as shown in Figure 49-a. The tests were conducted using an *EMIC* mechanical testing machine with a load capacity of 30 kN, as shown in Figure 49-b. The test was controlled by the displacement at a rate of 2 mm/min and were performed in six samples for each fiber type. The free distance (outside the sheets) was 20 mm for all fibers. The specific deformation corresponded to the relationship between the vertical displacement measured by the machine and the initial length measured between the reference marks. The tensile strength was calculated from the maximum load obtained during the test using the cross-sectional area of the original fiber (before testing) determined from the optical microscopy images. The test progressed until the fibers ruptured.

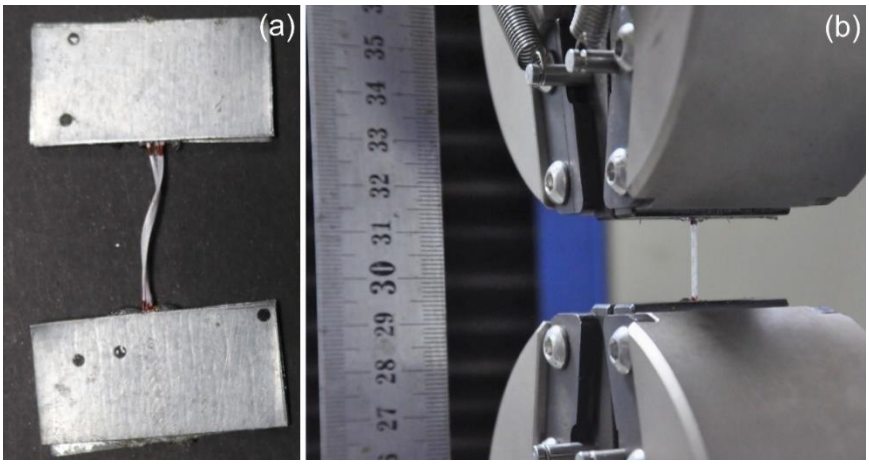

Figure 49. Experimental arrangement of the direct tensile test on fibers: (a) fiber glued to the sheet before being tested; (b) fiber positioned in the clamp to be tested.

5.2.2. Fourier Transform Infrared Spectroscopy (FTIR)

Fourier transform infrared spectroscopy (FTIR) was performed to identify the functional groups present in the three types of fibers, Fourier-Transform Infrared Spectroscopy (*FTIR*) tests were carried out. Characterization was carried out using an attenuated total reflectance (*ATR*) sensor in the spectral range of 4000–400 cm^{-1} with a resolution of 4 cm^{-1} and 32 scans. The tests were performed on a *Perkin-Elmer* FTIR-ATR spectrophotometer, model *Spectra-Two*, at the Laboratory of Synthesis and Laser Characterization of Nanomaterials (*NanoLaserLab*), Department of Physics, PUC-Rio.

This technique allows the quantitative analysis of organic compounds by identifying the vibrations that each group emits, causing the appearance of bands in the infrared spectrum, and is useful for identifying a compound or investigating its chemical composition. The intensity of the different bands can be explained by the difference in the amount of sample that passed through the infrared.

To compare the spectra, a sample of virgin polypropylene (PP) was used.

5.2.3. Single-fiber tensile creep test

The macro fibers used are synthetic polymers and, as such, suffer from the effect of creep over time. It is known that the creep pullout response of this type of fiber has a large portion owing to the creep of the fiber itself; therefore, its estimation is of great importance in an attempt to separate the fiber creep from the interface creep. The loading levels used were 50%, 40%, 30%, and 20% of the tensile strength and one sample were tested of each fiber and load level.

The experimental arrangement used in this test was designed for reuse in the direct tensile test, with two aluminum sheets glued to the ends of the analyzed fibers. In addition to these plates, two thicker aluminum claws were screwed into this initial arrangement: one end was fixed to a rigid gantry and the other was free, similar to a pendulum. A hole was opened at the free end of the claw and free weights were hung from the system. A rotational restriction was also inserted to reduce the effects of the pendulum arrangement. Figure 50 shows the experimental setup.

An angle bracket was screwed to the lower end of the fiber and an LVDT was positioned to obtain the displacements. The data acquisition system used was an HBM 1615, and the software used was Catman Easy at a frequency of 0.02 Hz. The displacement acquisition software is activated after the entire system is loaded. The weights were carefully and gradually placed to avoid dynamic effects during a 5-minute interval and then the acquisition system was activated. The tests were carried out in a room with controlled temperature and relative humidity of 20 ±1 °C and 50 ±5%, respectively. The samples were loaded for 10 days before unloading. Unfortunately, this setup could not efficiently measure the recovery after unloading owing to setup instability (pendulum behavior).

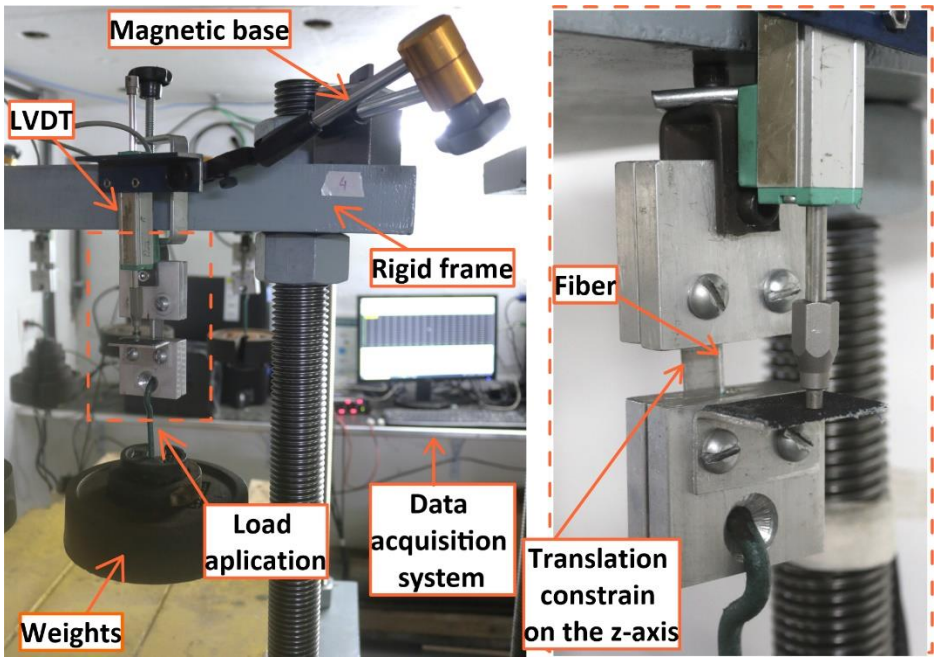

Figure 50. Proposed creep tensile setup test with details of its parts.

5.3. Experimental results and discussions

5.3.1. Direct tensile test

The average stress–strain curves for each type of fiber are shown in Figure 51. The properties obtained from the direct tensile test of the fibers, such as the maximum load, tensile strength, and modulus of elasticity, are presented in Table 13. The elastic modulus was calculated as the angular coefficient of the initial region of the curve, which was approximately 30% of the maximum stress.

The elastic modulus results were lower than those reported by the manufacturers at 46.1% for *BF*, 32.8% for *TF*, and 28.1% for *VF*. This reduction can be explained by the acquisition being made using the values of the testing machine itself, which incorporates all fiber accommodations and system deformations, in addition to the fact that the fibers were tested in their commercial sizes and not in filaments, what is still very surprising is the pronounced difference between the values obtained and those presented by the manufacturers. The mode of rupture of the fibers was defibrillation, as reported in [7,70].

It is observed that for the *VF* fiber, the slope of the curve changes in the range of less than 0.05 mm, which can be justified by the accommodation of the fiber itself (which is twisted) when being aligned during the tensile test. Otherwise (if the fiber were straight), it seems that there would not be much difference in relation to the modulus of elasticity of the *TF* fiber.

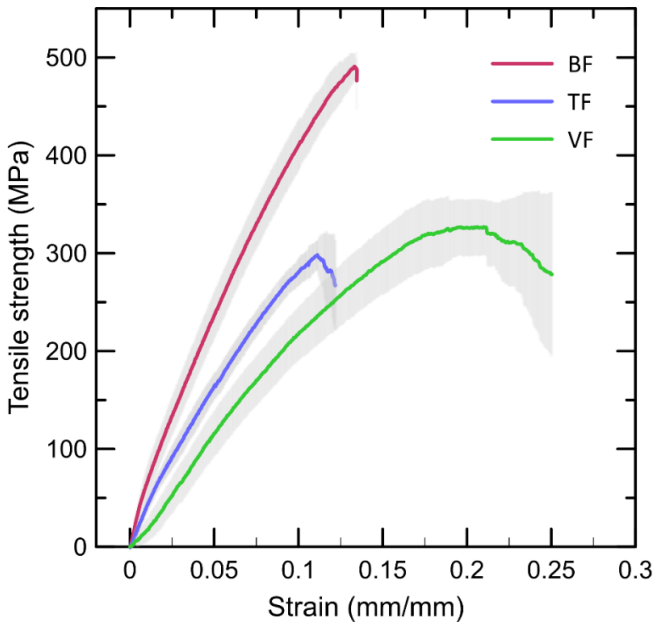

Figure 51. Stress *versus* strain curve of macro synthetic fibers obtained from the direct tensile test.

Table 13. Properties of the fibers.

Properties	*BF*	*TF*	*VF*
Maximum load (N)[a]	*286.1 ± 8.37*	*153.9 ± 9.56*	*163.6 ± 17.2*
Tensile strength (MPa)[a]	*490.8 ± 12.4*	*298.3 ± 13.7*	*326.9 ± 27.5*
Tensile strength (MPa) [b]	*640*	*540*	*600-650*
Modulus of elasticity (GPa) [a]	*5.53 ± 0.493*	*3.41 ± 0.404*	*2.67 ± 0.398*
Modulus of elasticity (GPa)[b]	*12*	10.4	*9.5*

[a] *obtained experimentally;* [b] *information provided by the manufacturer* [60–62].

5.3.2. Fourier Transform Infrared Spectroscopy (FTIR)

Figure 52 shows the IR spectra (enter 4000 – 600 cm^{-1}) of the three fibers and a virgin polypropylene (PP) pellet. Table 14 lists the spectra of the four materials. The characteristic peaks of the functional groups represented the polypropylene material, as indicated by the reference sample (PP). The same bands were identified in all the four samples; however, their intensities varied at some points. Because each type of covalent bond has a particular vibrational frequency, it can be assumed that these three samples have identical infrared absorption behaviors; therefore, they are samples of the same material. The three fibers exhibited identical spectra that did not exhibit resonances beyond those associated with the polypropylene (PP) structure, confirming that the additives were not present in significant quantities.

Therefore, it can be concluded that, although the fibers are classified as slightly different materials, they are essentially produced from polypropylene. Therefore, their main differences are not in the type of material and may be related to other characteristics such as shape, geometry and even the method of production.

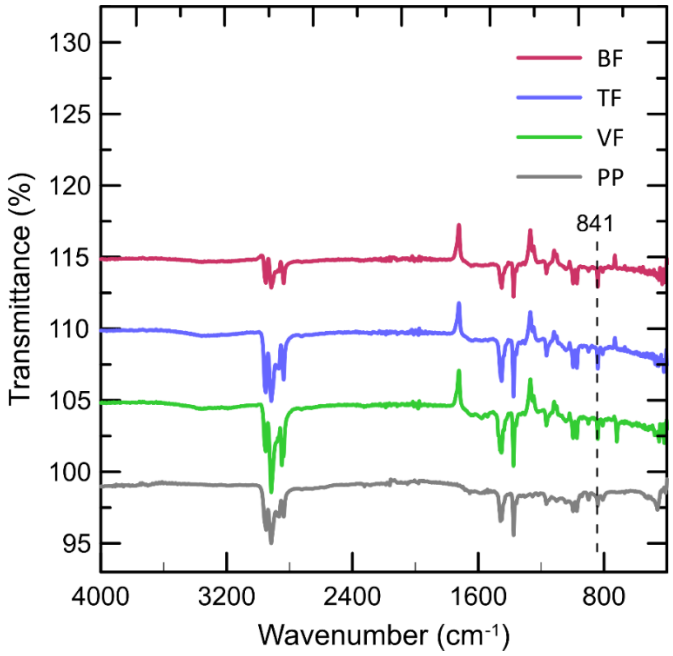

Figure 52. Spectrum of synthetic fibers.

Table 14. FTIR absorption of the samples used in this study and a virgin polypropylene sample, classified according to [96–100].

Assignment and vibration type	*Wavenumbers (cm^{-1})*			
	BF	*TF*	*VF*	*PP*
C–H stretching and CH_3 asymmetrical stretching	*2953*	*2951*	*2952*	*2949*
C–H stretching and CH_2 asymmetrical stretching	*2916*	*2917*	*2917*	*2917*
C–H stretching and CH_2 symmetrical stretching	*2838*	*2838*	*2839*	*2837*
CH_3 symmetrical bending	*1453*	*1454*	*1456*	*1459*
CH_3 symmetrical bending	*1379*	*1377*	*1376*	*1376*
C-H wagging and CH_3 rocking	*1169*	*1168*	*1167*	*1168*
C–C stretching and CH_3 asymmetrical rocking	*998*	*997*	*997*	*998*
C–C stretching and CH_3 rocking	*973*	*972*	*972*	*973*
C–C stretching, CH_2 rocking, and CH_3 rocking	*841*	*841*	*841*	*841*

5.3.1. Single-fiber tensile creep test

A single-fiber tensile creep test was performed to evaluate the performance of the fibers over time. Figure 53 to Figure 55 present the time (days) *versus* deformation (mm/mm) curves for all load levels analyzed. The curves in (a) show the results of a single sample tested for each load percentage, whereas those in (b) show the creep coefficient values for each load percentage. The creep coefficient, which is the relationship between the deformation at time (t) and the instantaneous deformation (δ_{inst}), is defined in Section 3.3.2, based on Equation (7). For ages of 3, 7, and 10 days, the parameters for the three fibers are summarized in Table 15.

The percentage of sustained loading to which the fibers were subjected represents the load levels experienced during service. All fibers showed an initial instantaneous deformation (δ_{inst}), followed by a rapid increase of strain at a decreasing rate (primary creep). Then, the creep rate stabilizes and the secondary creep phase is achieved. Regarding the initial instantaneous deformation, it was observed in all samples that the greater the load, the greater the initial deformation, which was mainly attributed to the elongation of the free length. The *BF* fiber was subjected to a greater load and still exhibited lower initial instantaneous deformations, which can be justified by its higher modulus of elasticity, although they could not be directly compared because they were subjected to completely different loads.

For samples loaded up to 40%, there was a tendency for fiber elongation to stabilize around the age of 10 days. However, for those loaded at a 50% load level, a pronounced increase in deformation could still be observed, especially for the *VF* fiber. At this 50% loading level, the most pronounced deformation was observed in the *VF* fibers, which also had the lowest modulus of elasticity. The values obtained for the *VF* fibers are in accordance with those reported by Lima *et al.* [7]. None of the fibers reached the tertiary creep phase at the evaluated ages. According to the FTIR analysis presented in Section 5.3.2, the fibers are made of polypropylene, so the differences in long-term elongation can be attributed to the manufacturing process, especially in the case of the *VF* fiber, which is a multifilament.

The strain (%) of the fibers over time ranged from 3-8% for the *BF* fibers, 7-12% for the *TF* fibers and 5-28% for the *VF* fibers. Babafemi *et al.* [38] found a strain of approximately 43% for an age of 4 days and 30% load, while MacKay and Trottier [75] stated that, for fibrillated synthetic fibers, this value can reach 40%.

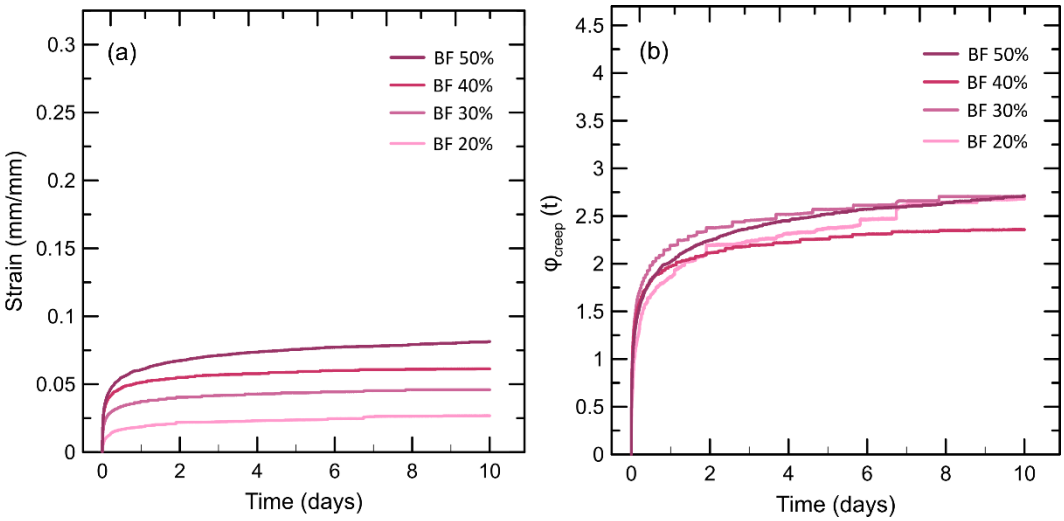

Figure 53. (a) Strain *versus* time curves for the *BF* fiber loaded with different percentages of the loads obtained in direct tensile tests; (b) creep coefficient ($\varphi_{creep}\ (t)$) over time for all loading levels tested.

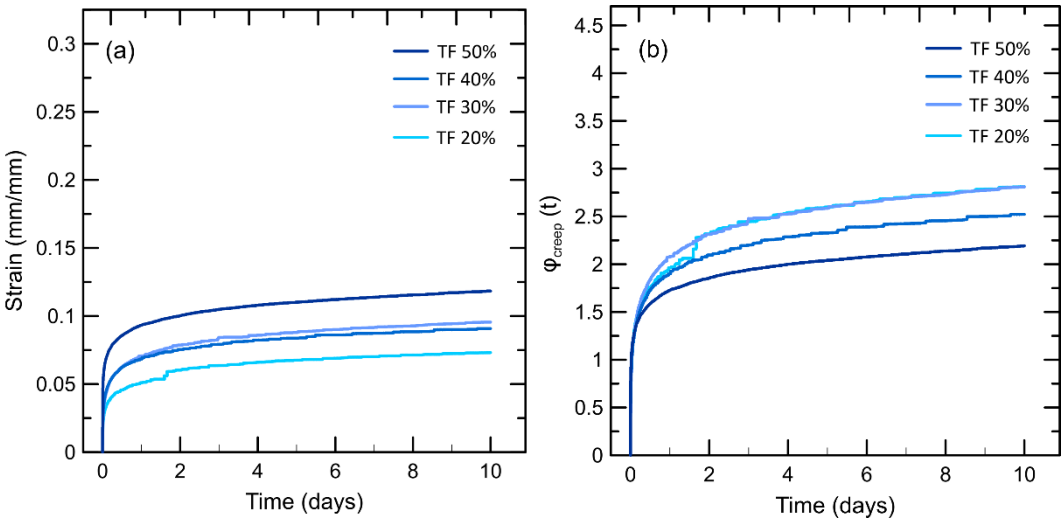

Figure 54. (a) Strain *versus* time curves for the *TF* fiber loaded with different percentages of the loads obtained in direct tensile tests; (b) creep coefficient ($\varphi_{creep}\ (t)$) over time for all loading levels tested.

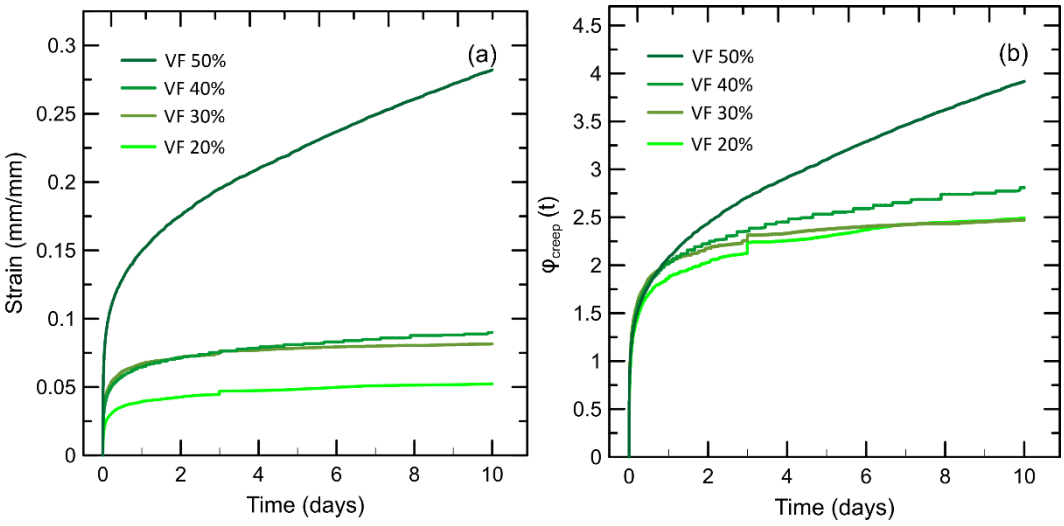

Figure 55. (a) Strain *versus* time curves for the *VF* fiber loaded with different percentages of the loads obtained in direct tensile tests; (b) creep coefficient ($\varphi_{creep}\ (t)$) over time for all loading levels tested.

Table 15. Summary of instantaneous displacements and creep coefficients at ages 3, 7 and 10 days for all samples tested.

Fiber type	δ_{inst} *(mm/mm)*	φ_{creep}		
		3 days	*7 days*	*10 days*
BF 20%	*0.01*	2.23	2.61	*2.68*
BF 30%	*0.017*	*2.45*	*2.66*	*2.7*
BF 40%	*0.026*	*2.18*	*2.34*	*2.36*
BF 50%	*0.03*	*2.37*	*2.6*	*2.71*
TF 20%	*0.026*	*2.45*	*2.7*	2.81
TF 30%	*0.034*	*2.47*	2.69	2.81
TF 40%	*0.036*	*2.2*	*2.42*	*2.52*
TF 50%	*0.054*	1.94	*2.11*	*2.19*
VF 20%	*0.021*	*2.24*	*2.43*	*2.49*
VF 30%	*0.033*	*2.32*	*2.42*	*2.47*
VF 40%	*0.032*	*2.35*	*2.65*	*2.81*
VF 50%	*0.072*	*2.71*	*3.46*	*3.92*

As in Chapters 3 and 4, the viscoelastic behavior of single fibers in tension under a sustained load was evaluated by applying the four-parameter rheological Burgers model described in Section 3.3.2 and equation (8). Table 16 presents the model parameters for all the three fibers at all sustained loading levels. The

correlation coefficient, R^2, was also reported for each analysis to prove the fit of the experimental curves. Correlation coefficients greater than 0.94 were obtained for all scenarios, demonstrating a good fit to the model. The R_1 parameter that regulates fiber stiffness was higher in the case of *BF* fibers (ranging between 15.3 and 20.7x20^3 MPa) and with relatively lower values for *TF* fibers (ranging between 22.2 and 47.7x20^2 MPa) and *VF* (ranging between 25.8 and 60×20^2 MPa), corroborating the results of the elastic modulus of the fibers. The parameter η_1, which is related to the secondary creep rate, remains consistent with the curves, presenting the lowest value for the *VF* fiber subjected to 50% load and which has a deformation progressively increasing with time, followed by the other load percentages of the same fiber.

Table 16. Burgers model parameters from fiber tensile creep tests

Fiber type	*Loading level*	*Burgers model parameters*				R^2
		R_1 *(MPa)*	R_2 *(MPa)*	η_1 *(MPa.s)*	η_2 *(MPa.s)*	
BF	50%	15.3x10^3	54.2x10^2	84.7x10^8	14.2x10^7	0.96
	40%	20.7x10^3	48x10^2	10.9x10^9	86x10^6	0.94
	30%	20.5x10^3	20.1x10^2	10x10^9	88.4x10^6	0.95
	20%	18.4x10^3	74.4x10^2	80.7x10^8	20.8x10^7	0.97
TF	50%	32.3x10^2	31.1x10^2	45.6x10^8	59.3x10^6	0.95
	40%	47.7x10^2	26.8x10^2	40.6x10^8	52.7x10^6	0.95
	30%	33.9x10^2	17.6x10^2	40x10^8	66.7x10^6	0.97
	20%	22.2x10^2	18x10^2	36.7x10^8	11.9x10^7	0.98
VF	50%	25.8x10^2	18.9x10^2	10.1x10^8	68.9x10^6	0.99
	40%	63x10^2	28.5x10^2	43.1x10^8	76.1x10^6	0.97
	30%	35.3x10^2	22.9x10^2	68.7x10^8	60.8x10^6	0.95
	20%	41.4x10^2	26x10^2	43.6x10^8	68.2x10^6	0.96

5.4. Description of the developed model

An analytical model based on the differential equation for bond-slip is proposed to analyze the contributions of the interface and fibers in the pullout response under long-term loading. The general behavior of a pullout curve

undergoes three stages: 1) perfect adhesion between the fiber and matrix, 2) gradual detachment of the fiber (loss of adhesion with the matrix), and 3) sliding owing to friction. However, to represent the creep behavior, it is not necessary to model all these steps because, under service conditions, the load does not reach its maximum value. Nonetheless, even for cases where detachment occurs, the equation may be used to obtain an apparent behavior.

The following assumptions are made:

- There is no detachment of the fiber; that is, perfect adhesion between the fiber and matrix was considered.
- The shear stress (τ) at the fiber-matrix interface increases proportionally with the increase in displacement (u) of the fiber, that is $\tau = k.u$ (where k is the adhesion modulus corresponding to the perfect adhesion phase).
- The fiber has a linear-elastic behavior.

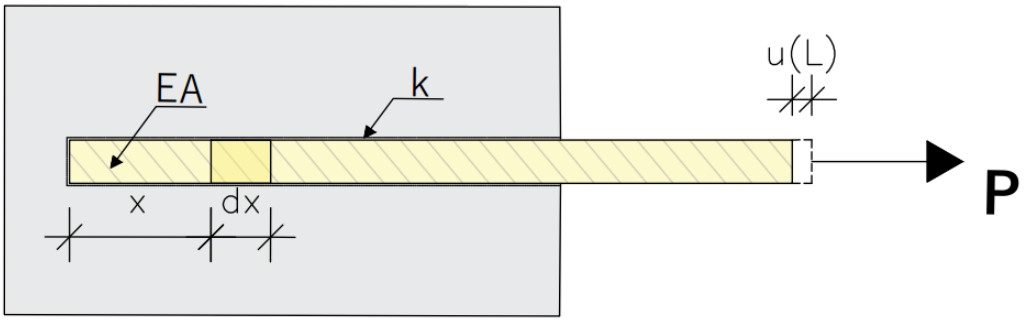

Figure 56. Model representation.

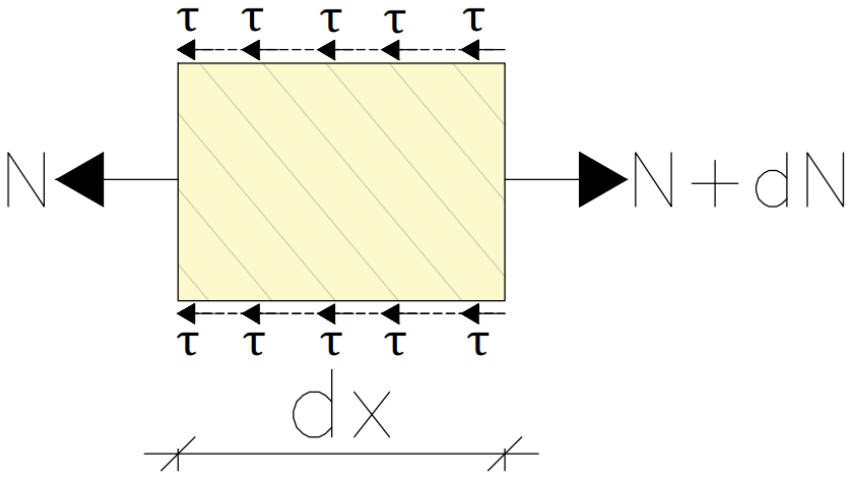

Figure 57. Equilibrium of the infinitesimal element *dx*.

The balance of forces in the infinitesimal element (Figure 57) in the horizontal direction results in:

$$\sum F_x = 0 \rightarrow N(x) + dN = N(x) + \tau(x)\pi\phi dx = 0 \quad (9)$$

Therefore,

$$\tau(x)\pi\phi = \frac{dN(x)}{dx} \quad (10)$$

where ϕ is the fiber diameter, $N(x)$ is the normal force (axial or longitudinal internal force) [F], and dx is the original length of an infinitesimal bar element [L].

The normal force is given by the product of the stress and cross-sectional area, as follows:

$$N(x) = E.\varepsilon(x).A \quad (11)$$

where E is the modulus of elasticity of the fiber and A is the cross-sectional area of the fiber given by $A = \frac{\pi\phi^2}{4}$. Replacing the shear stress (τ) with $\tau = k.u$ and equation (11) in equation (10), it is possible to obtain:

$$ku(x)\pi\phi = E\frac{\pi\phi^2}{4}\frac{d\varepsilon(x)}{dx} \quad (12)$$

The deformation $\varepsilon(x)$ is equal to the ratio between the variation in length of the infinitesimal element and its original length. Thus:

$$\varepsilon(x) = \frac{du(x)}{dx} \quad (13)$$

Equation (11) can be then be rewritten as:

$$4ku(x) = E\phi\frac{d^2u(x)}{dx^2} \quad (14)$$

where du denotes the internal relative axial (longitudinal) displacement of an infinitesimal bar element [L].

Rearranging the terms in Equation (14) yields the following differential equation:

$$\frac{d^2u}{dx^2} - \frac{4k}{E\phi}u = 0 \quad (15)$$

Which is a differential equation of the form:

$$\frac{d^2u}{dx^2} - \alpha^2 u = 0 \tag{16}$$

where α is a parameter that indicates the relative stiffness between the interface and the fiber, as follows:

$$\alpha = \sqrt{\frac{4k}{E\phi}} \tag{17}$$

Finally, the solution to the differential equation (16) is well-known and can be written for the displacement $u(x)$ and the strain $\varepsilon(x)$ as:

$$u(x) = C_1 e^{\alpha x} + C_2 e^{-\alpha x} \tag{18}$$

$$\varepsilon(x) = \frac{du(x)}{dx} = \alpha(C_1 e^{\alpha x} - C_2 e^{-\alpha x}) \tag{19}$$

The constants C_1 and C_2 can be obtained by applying the boundary conditions below:

- At the unloaded end of the embedded fiber, the fiber deformation is zero, i.e. $\varepsilon(0) = 0$;
- When $x = L$, the deformation in the fiber will be equal to the relationship between the applied force and the fiber stiffness, i.e., $\varepsilon(L) = \varepsilon_0 = \frac{P}{EA}$.

Finally, the displacement $u(x)$ and the fiber deformation $\varepsilon(x)$ are obtained:

$$u(x) = \frac{\varepsilon_0}{\alpha.\sinh(\alpha L)} \cosh(\alpha x) \tag{20}$$

$$\varepsilon(x) = \frac{\varepsilon_0}{\sinh(\alpha L)} \sinh(\alpha x) \tag{21}$$

For the pullout problem studied in Chapter 3, the fiber can be considered to be embedded with a length L_A on one side, L_B on the other side, and with a free length L_0, as shown in Figure 58. The opening of cracks (w) is represented by the sum of the displacements of the embedded portions with the free length, given by:

$$w = \frac{\varepsilon_0}{\alpha \ \sinh \alpha L_A} \cosh \alpha L_A \ + \frac{\varepsilon_0}{\alpha \ \sinh \alpha L_B} \cosh \alpha L_B + \varepsilon_0 L_0 \qquad (22)$$

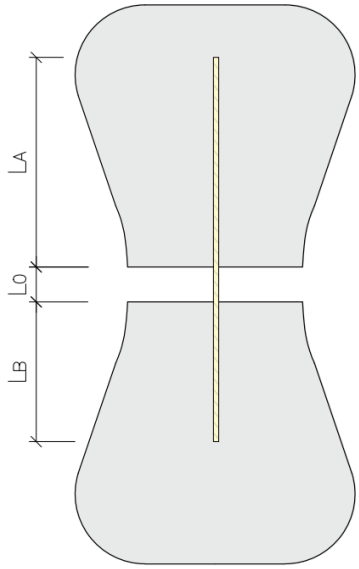

Figure 58. Pullout sample with description of embedded and free fiber lengths.

In the case of behavior over time, modeling is much more complex. However, a simplification is proposed, assuming that the modulus of elasticity of the fiber decreases over time (the deformation increases, and at each instant of time, the 'modulus' is different). Then, the parameter k needs to be adjusted over time as the modulus decreases (similar to the creep coefficient). The model can then be applied to different test times if different values of the modulus of elasticity are considered for the material. Thus, the equation for crack opening $w(t)$ over time can be written according to Eq. 23. If the fiber properties and the crack opening at each given time are known, the bond parameter k can be adjusted in the α parameter to satisfy Eq. 23. Therefore, a law describing the k parameter with time can be indirectly determined.

$$w(t) = \frac{\varepsilon_0(t)}{\alpha(t) \sinh \alpha(t) L_A} \cosh \alpha(t) L_A + \frac{\varepsilon_0(t)}{\alpha(t) \sinh \alpha(t) L_B} \cosh \alpha(t) L_B + \varepsilon_0(t) L_0 \ (23)$$

This development is valid for the case of fibers oriented perpendicular to the cracks, but will be applied to the case of inclined fibers, considering that the fiber is perpendicular to the crack surface, giving an equivalent response.

5.5. Analytical results

When applying the data obtained from the short- and long-term fiber pullout and tensile tests, small discrepancies were observed in the acquisition of short-term values for the pullout test. As the setup reproduced the configuration of a pendulum, two LVDTs should have been used, and their average would result in displacements due to pullout. However, only one LVDT was used, and although great care was taken to avoid this, small misalignments of the transducers with the fibers and small rotations of the sample may have caused the initial reading errors. To apply the model more efficiently, the initial values of w in the creep pullout curves were corrected to the initial values obtained in the short-term pullout tests, and the remainder of the curve was updated to this correction factor.

The loading level chosen was 50% to enable analysis at different inclination angles. Considering the linear regime of the pullout curve, the known data of the problem are: w, ε_0, L_A, L_B, L_0, ϕ and E. Indirectly, it is possible to determine the average value of the interface stiffness k. The k values for all fibers and inclination angles are shown in the Table 17 and Figure 59.

Table 17. Bond stiffness evaluated for different inclinations.

Fiber type	*Fiber orientation*	k *(MPa/mm)*			
		Short- term	*3 days*	*7 days*	*10 days*
BF	0°	5.45	2.22	1.95	1.83
	15°	22.7	18.7	17.2	16.7
	30°	10.6	9.85	9.44	9.07
	45°	2.65	5.58	5.51	5.47
TF	0°	4.17	3.31	2.89	1.55
	15°	23.1	20.8	17.7	15.97
	30°	7.33	6.99	5.96	5.24
	45°	2.72	5.41	5.11	5.04
VF	0°	1.85	0.97	0.47	0.34
	15°	1.57	0.49	0.33	0.21
	30°	3.45	0.59	0.54	0.35
	45°	1.37	1.26	1.02	0.93

Evaluating for the tests of short duration that at 0° the *BF* fiber presents the highest k value, followed by the *TF* and *VF* fibers. These results corroborate the pullout and tensile test results on the fiber, which demonstrate that, in addition to the fiber's greater stiffness and greater modulus of elasticity, it has better adhesion to the matrix (as shown in the image tests in Sections 3.3.3 and 3.3.4). A small reduction in the k value compared to that of the *BF* fiber was observed for the *TF* fiber. These similar values are, as already explained, justified by the surface corrugation of both fibers, leaving the *VF* fiber, which is smooth, at a disadvantage in terms of adhesion to the matrix. Increases in k can be observed for inclinations of 15° and 30°, possibly because of the snubbing effect (described in Chapter 4), which is drastically reduced at an angle of 45° owing to the increased probability of fiber rupture.

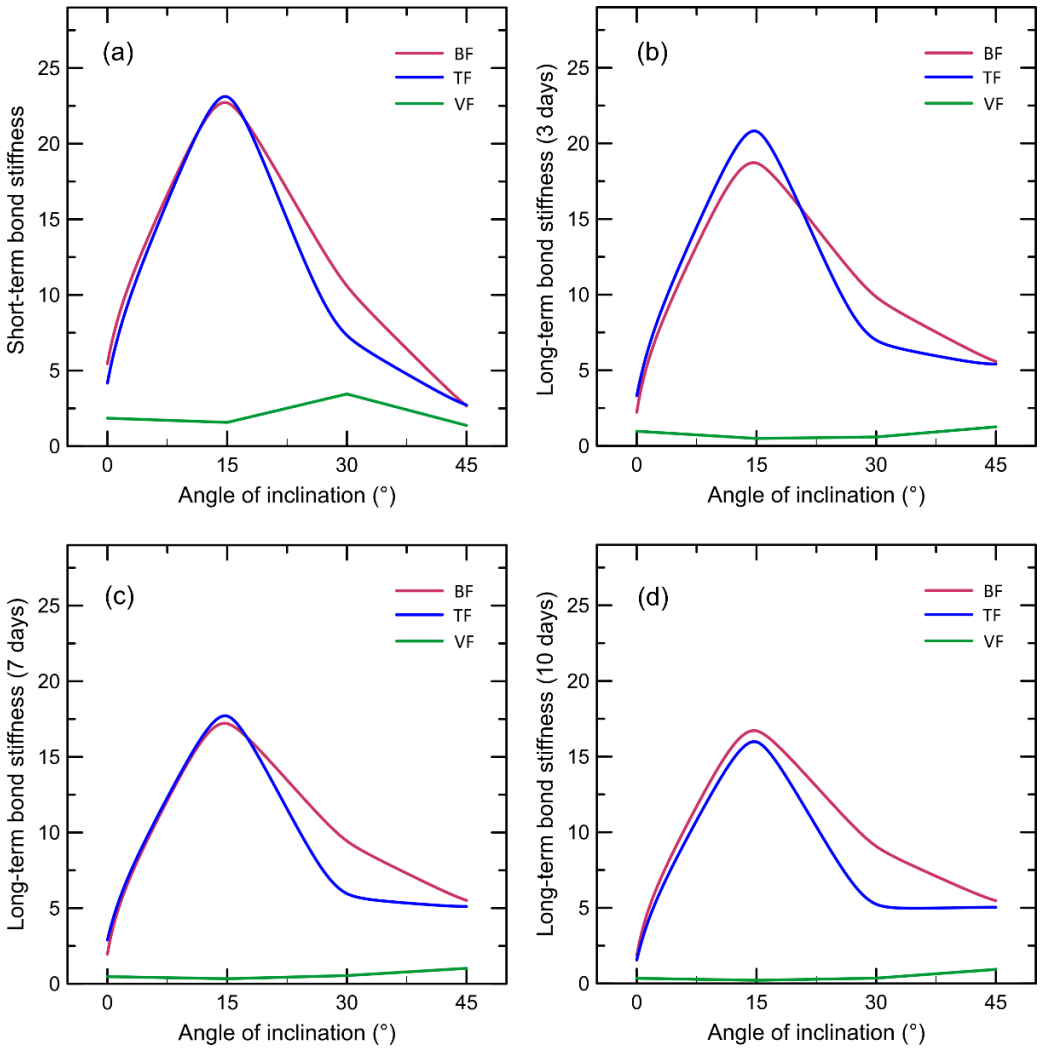

Figure 59. Bond stiffness evaluated for different inclinations at (a) short-term; (b) 3 days; (c) 7 days and (d) 10 days.

In long-term analysis, the data $w(t)$, $\varepsilon_0(t)$ and $E(t)$, are a function of time. At 0°, the interface stiffness k decreased with time, as did the modulus of elasticity. The reduction in k after 10 days of testing reached 64.2%, 62.8% for the *TF* fiber and 81.6% for the *BF*, TF, and *VF* fibers, respectively, with the greatest decay observed between 0 and 3 days. The same decay was observed at the other angles. The *BF* and *TF* fibers at an angle of 45° experienced an increase in k in the long-term results compared to the short-term results. This increase may be due to the more intensified damping mechanisms of these fibers, which are straight when inclined at this magnitude, as discussed in Chapter 4.

5.6. Conclusions

As a result, the following conclusions can be drawn:

1. Short-term fiber tensile tests showed that straight fibers with surface corrugation have greater tensile strength than deformed and smooth fibers.
2. Although technical reports indicate that the fibers have small differences in their composition, the Fourier transform infrared spectroscopy tests demonstrated practically identical spectra, indicating that the performance of the fibers is better due to their shape, surface corrugation, and manufacturing process than to the type of material used.
3. In tensile tests under a sustained load, fibers with a higher modulus had lower initial instantaneous deformations, which were attributed to the elongation of the free section. At different load levels, it was observed that for up to 40% of the load, the curves demonstrated a stabilization of the deformation at the age of 10 days, whereas for the 50% load level, the deformation appeared to grow progressively.
4. The developed analytical model presented interface stiffness results that corroborated other analyses conducted throughout this thesis.

6. GENERAL CONCLUSIONS

This thesis presents a study on the pullout behavior of macro synthetic fibers in short- and long-term tests. Three types of fibers were used (*BF*, *TF*, and *VF*), and the variables analyzed were the surface corrugation of the fiber (crimped and smooth), percentage of sustained loading (20%, 30%, 40%, and 50%), and inclination angles of the fibers. fibers with respect to the loading direction (15°, 30°, and 45°). In addition to the pullout tests, short and long tensile tests and fiber characterization using Fourier transform infrared spectroscopy were carried out.

Short-term tests found that for fibers aligned in the loading direction, the geometry and surface corrugation were decisive in the pullout response, as corroborated by microtomography (microCT) and scanning electron microscopy (SEM) images. When the fiber inclination angle was varied, there was a reduction in the bond tension as the angle increased. Surface degradation after the pullout of synthetic fibers is known to be a means of evaluating adhesion with the matrix. In this study, fibers aligned with surface corrugation and those with greater inclinations were shown to be more degraded, with a significant increase in the probability of rupture the greater the evaluated inclination angle.

In the long-term tests, micro-CT and SEM images helped to elaborate on the statement that the pullout creep is largely due to the creep of the fiber, which, being polymeric, suffers significantly from the effects of sustained load. In the aligned fibers, the SEM images show that the fibers with surface corrugation (*BF* and *TF*) were still able to maintain some adhesion with the matrix even after 10 days of testing at a loading percentage of 50%, which was not observed for the smooth fibers. (*VF*). When inclination angles were imposed on the fibers, the snubbing effect was significantly greater in straight fibers, which had a reduction in creep with increasing fiber inclination angle, with the measured slip being basically attributed to the creep experienced by the free section of the fiber.

The Burgers viscoelastic model was applied to all experimental curves of the creep tests, and because of the good fit found, parameter approximation functions were developed and implemented in the cementitious composite models to simulate their behavior.

A study on isolated fibers also showed that the major difference between them was probably in their manufacturing processes and surface corrugation, as Fourier transform infrared spectroscopy tests did not demonstrate a significant difference in their composition. In tensile tests under sustained loads, it was

observed that there was a progressive increase in deformation for fibers subjected to 50% load, whereas lower load levels seemed to stabilize at the age of 10 days. An analytical model is proposed, and the results based on the interface stiffness corroborate the analyses conducted.

The analyses aimed to contribute to the interpretation of the complex mechanism involved in the pulling-out process of macro synthetic fibers, especially under sustained loads, although some issues could not be resolved. Suggestions are presented in the following section.

6.1. Suggestions for future work

Based on the results presented here, suggestions for continuing this work are:

- Improve the experimental arrangement of the pullout test with a sustained load. Thus, it is feasible to use a pair of LVDTs and acquire more accurate results, given the sensitivity of the pendulum-shaped system.
- Produce composites with the three fibers studied and evaluate their behaviors through flexure and tensile tests under sustained loads.
- A deeper analysis of the fiber inclination angle in the proposed analytical model and insert a way to implement this variable.
- Implement adhesion equations in a model with a discrete representation of fibers and simulate characterization tests to obtain post-cracking parameters.

7. REFERENCES

[1] W.P. Boshoff, G.P.A.G. van Zijl, Time-dependent response of ECC: Characterisation of creep and rate dependence, Cem Concr Res 37 (2007) 725–734. https://doi.org/10.1016/j.cemconres.2007.02.001.

[2] W. Boshoff, Adendorff. C. J., Effect of sustained tensile loading on SHCC crack widths, Cem Concr Compos 37 (2013) 119–128.

[3] A.J. Babafemi, W.P. Boshoff, Tensile creep of macro-synthetic fibre reinforced concrete (MSFRC) under uni-axial tensile loading, Cem Concr Compos 55 (2015) 62–69. https://doi.org/10.1016/j.cemconcomp.2014.08.002.

[4] B. Bissonnette, M. Pigeo, A.M. Vaysburd, Tensile Creep of Concrete: Study of Its Sensitivityto Basic Parameters, ACI Mater J 104 (2007) 360–370.

[5] P.D. Nieuwoudt, A.J. Babafemi, W.P. Boshoff, The response of cracked steel fibre reinforced concrete under various sustained stress levels on both the macro and single fibre level, Constr Build Mater 156 (2017) 828–843.

[6] R. Zerbino, D.H. Monetti, G. Giaccio, Creep behaviour of cracked steel and macro-synthetic fibre reinforced concrete, Materials and Structures/Materiaux et Constructions 49 (2016) 3397–3410. https://doi.org/10.1617/s11527-015-0727-y.

[7] V. Nogueira Lima, D.C. Taissum Cardoso, F. de Andrade Silva, Creep Mechanisms in Precracked Polypropylene and Steel Fiber–Reinforced Concrete, Journal of Materials in Civil Engineering 33 (2021). https://doi.org/10.1061/(asce)mt.1943-5533.0003775.

[8] S. Kurtz, P. Balaguru, Postcrack creep of polymeric fiber-reinforced concrete in flexure, Cem Concr Res 30 (2000) 183–190.

[9] N. Buratti, C. Mazzotti, M. Savoia, Post-cracking behaviour of steel and macro-synthetic fibre-reinforced concretes, Constr Build Mater 25 (2011) 2713–2722. https://doi.org/10.1016/j.conbuildmat.2010.12.022.

[10] A.J. Babafemi, W.P. Boshoff, Testing and modelling the creep of cracked macro-synthetic fibre reinforced concrete (MSFRC) under flexural loading, Materials and Structures/Materiaux et Constructions 49 (2016) 4389–4400. https://doi.org/10.1617/s11527-016-0795-7.

[11] P. Pujadas, A. Blanco, S. Cavalaro, A. la Fuente, A. Aguado, The need to consider flexural post-cracking creep behavior of macro-synthetic fiber reinforced concrete, Constr Build Mater 149 (2017) 790–800.

[12] M.J. Wattsa, A. Amin, R.I. Gilbert, Time-dependent deformation and cracking behaviour of FRC beams, Eng Struct 268 (2022) 114741. https://doi.org/10.1016/j.engstiuct.2022.114741.

[13] W.S.A. Nana, H. V. Tran, T. Goubin, G. Kubisztal, A. Bennani, T.T. Bui, G. Cardia, A. Limam, Behaviour of macro-synthetic fibers reinforced concrete: Experimental, numerical and design code investigations, Structures 32 (2021) 1271–1286. https://doi.org/10.1016/j.istruc.2021.03.080.

[14] A.J. Babafemi, A. du Plessis, W.P. Boshoff, Pull-out creep mechanism of synthetic macro fibres under a sustained load, Constr Build Mater 174 (2018) 466–473. https://doi.org/10.1016/j.conbuildmat.2018.04.148.

[15] R. Vrijdaghs, M. di Prisco, L. Vandewalle, Short-term and creep pull-out behavior of polypropylene macrofibers at varying embedded lengths and angles from a concrete matrix, Constr Build Mater 147 (2017) 858–864. https://doi.org/10.1016/j.conbuildmat.2017.05.005.

[16] A.J. Babafemi, W.P. Boshoff, Tensile creep of macro-synthetic fibre reinforced concrete (MSFRC) under uni-axial tensile loading, Cem Concr Compos 55 (2015) 62–69. https://doi.org/10.1016/j.cemconcomp.2014.08.002.

[17] A.J. Babafemi, A. du Plessis, W.P. Boshoff, Pull-out creep mechanism of synthetic macro fibres under a sustained load, Constr Build Mater 174 (2018) 466–473. https://doi.org/10.1016/j.conbuildmat.2018.04.148.

[18] R. Vrijdaghs, M. di Prisco, L. Vandewalle, Short-term and creep pull-out behavior of polypropylene macrofibers at varying embedded lengths and angles from a concrete matrix, Constr Build Mater 147 (2017) 858–864. https://doi.org/10.1016/j.conbuildmat.2017.05.005.

[19] A.E. Naaman, A.S. Argon, F. Moavenzadeh, A FRACTURE MODEL FOR FIBER REINFORCED CEMENTITIOUS MATERIALS FRACTURE, THEORIES, FIBER COMPOSITES, CONCRETE, Pergamon Press, Inc, 1973.

[20] A. Sze-Tong Yam, S. Mindess, The effects of fibre reinforcement on crack propagation in concrete, 1982.

[21] U.N. Gokoz, A.E. Naaman, Effect of strain-rate on the pull-out behaviour of fibres in mortar, 1981.

[22] J.M. Alwan, A.E. Naaman, W. Hansen, Pull-Out Work of Steel Fibers From Cementitious Composites: Analytical Investigation, 1991.

[23] P. Robins, S. Austin, P. Jones, Pull-out behaviour of hooked steel fibres, 2002.

[24] A. Bentur, S. Mindess, Fibre reinforced cementitious composites, Second, Taylor & Francis, Milton Park, UK, 2007.

[25] N. Banthia, J.-F. Trottier, DEFORMED STEEL FIBER-CEMENTITIOUS MATRIX BOND UNDER IMPACT, 1991.

[26] A.E. Naaman, G. Namur, H. Najm, J.A. Sa, BOND MECHANISMS IN FIBER REINFORCED CEMENT-BASED COMPOSITES, 1989.

[27] F. Deng, X. Ding, Y. Chi, L. Xu, L. Wang, The pull-out behavior of straight and hooked-end steel fiber from hybrid fiber reinforced cementitious composite: Experimental study and analytical modelling, Compos Struct 206 (2018) 693–712. https://doi.org/10.1016/j.compstruct.2018.08.066.

[28] N. Banthia, A study of some factors affecting the fiber-matrix bond in steel fiber reinforced concrete, Can. J. Clv. Eng. 17 (1990) 610–620. www.nrcresearchpress.com.

[29] F. Isla, G. Ruano, B. Luccioni, Analysis of steel fibers pull-out. Experimental study, Constr Build Mater 100 (2015) 183–193. https://doi.org/10.1016/j.conbuildmat.2015.09.034.

[30] A. Bentur, S.T. Wu, N. Banthia, R. Baggott, W. Hansen, A. Katz, C.K.Y. Leung, V.C.L.B. Mobasher, A.E. Naaman, R. Robertson, P. Soroushian, H. Stang, L.R. Taerwe, Fiber-matrix interfaces, in: A.E. Naaman, H.W. Reinhardt (Eds.), High Performance Fiber Reinforced Cement Composites 2 (HPFRCC2), E & FN Spon, Ann Arbor, 1995: pp. 149–192.

[31] C. Ding, L. Guo, B. Chen, Orientation distribution of polyvinyl alcohol fibers and its influence on bridging capacity and mechanical performances for high ductility cementitious composites, Constr Build Mater 247 (2020). https://doi.org/10.1016/j.conbuildmat.2020.118491.

[32] Y. Lee, S.T. Kang, J.K. Kim, Pullout behavior of inclined steel fiber in an ultra-high strength cementitious matrix, Constr Build Mater 24 (2010) 2030–2041. https://doi.org/10.1016/j.conbuildmat.2010.03.009.

[33] Y.Y.Y. Cao, Q.L. Yu, Effect of inclination angle on hooked end steel fiber pullout behavior in ultra-high performance concrete, Compos Struct 201 (2018) 151–160. https://d0i.0rg/l0.1016/j.compstruct.2018.06.029.

[34] Y.-S. Taia, S. El -Tawilb, High loading-rate pullout behavior of inclined deformed steel fibers embedded in ultra-high performance concrete, Constr Build Mater 148 (2017) 204–218.

[35] W.D. Callister Jr., Ciência e Engenharia de Materiais: Uma introdução, 2002.

[36] Q. Zhao, J. Yu, G. Geng, J. Jiang, X. Liu, Effect of fiber types on creep behavior of concrete, Constr Build Mater 105 (2016) 416–422. https://doi.org/10.1016/j.conbuildmat.2015.12.149.

[37] R. Vrijdaghs, E. Verstrynge, L. Vandewalle, A two-phased and multi-scale finite element analysis of the tensile creep behavior of polypropylene fiber reinforced concrete, in: 857Computational Modelling of Concrete Structures – Meschke, Pichler & Rots (Eds, 2018: pp. 857–866.

[38] A.J. Babafemi, W.P. Boshoff, Pull-out response of macro synthetic fibre from concrete matrix: Effect of loading rate and embedment length, Constr Build Mater 135 (2017) 590–599. https://doi.org/10.1016/j.conbuildmat.2016.12.160.

[39] D. Guner, O. Golbasi, H. Ozturk, Generic creep behavior and creep modeling of an aged surface support liner under tension, Journal of Rock Mechanics and Geotechnical Engineering 14 (2022) 377–384. https://doi.org/10.1016/j.jrmge.2021.12.004.

[40] S. Sánchez-Beitia, D. Luengas-Carreño, M. Crespo de Antonio, The presence of secondary creep in historic masonry constructions: A hidden problem, Eng Fail Anal 82 (2017) 315–326. https://doi.org/10.1016/j.engfailanal.2017.04.033.

[41] N. Houhou, K. Benzarti, M. Quiertant, S. Chataigner, A. Fléty, C. Marty, Analysis of the nonlinear creep behavior of concrete/FRP-bonded assemblies, J Adhes Sci Technol 28 (2014) 1345–1366. https://doi.org/10.1080/01694243.2012.697387.

[42] M.H. Sabour, Creep, in: Encyclopedia of Tribology, Springer US, Boston, MA, 2013: pp. 618–627. https://doi.org/10.1007/978-0-387-92897-5_291.

[43] F. Mainardi, G. Spada, Creep, Relaxation and Viscosity Properties for Basic Fractional Models in Rheology, (2011). https://doi.org/10.1140/epjst/e2011-01387-1.

[44] M.A. Chowdhury, M.M. Alam, M.M. Rahman, M.A. Islam, Model-Based Study of Creep and Recovery of a Glassy Polymer, Advances in Polymer Technology 2022 (2022). https://doi.org/10.1155/2022/8032690.

[45] J.L. Yang, Z. Zhang, A.K. Schlarb, K. Friedrich, On the characterization of tensile creep resistance of polyamide 66 nanocomposites. Part II: Modeling and prediction of long-term performance, Polymer (Guildf) 47 (2006) 6745–6758. https://doi.org/10.1016/j.polymer.2006.07.060.

[46] R. Wang, L. Li, Burgers creep model used for describing and predicting the creep behaviour of a rock under uniaxial and triaxial compression test conditions, n.d.

[47] A. Sprince, A. Korjakins, L. Pakrastinsh, Time-dependent behavior of high performance fiber-reinforced concrete, in: Adv Mat Res, 2013: pp. 75–80. https://doi.org/10.4028/www.scientific.net/AMR.705.75.

[48] X. Hou, M. Abid, W. Zheng, R.R. Hussain, Effects of Temperature and Stress on Creep Behavior of PP and Hybrid Fiber Reinforced Reactive Powder Concrete, Int J Concr Struct Mater 13 (2019). https://doi.org/10.1186/s40069-019-0357-9.

[49] C. Del Prete, N. Buratti, C. Mazzotti, Experimental analysis of time dependent phenomena and temperature effects on macro-synthetic fibre reinforced concretes in different loading conditions, Constr Build Mater 326 (2022). https://doi.org/10.1016/j.conbuildmat.2022.126904.

[50] A.S. Drozdov, Creep rupture and viscoelastoplasticity of polypropylene, Engineerinf Fracture Mechanics 77 (2010) 2277–2293.

[51] F.R. Souza, V.N. Lima, D.C.T. Cardoso, F.A. Silva, Experimental Study of Polyvinyl Alcohol (PVA) Fiber Reinforced Concrete under Cyclic Loading, in: CILAMCE-PANACM-2021 Proceedings of the XLII Ibero-Latin-American Congress on Computational Methods in Engineering and III Pan-American Congress on Computational Mechanics, ABMEC-IACM, 2021.

[52] ABNT (Associação de Normas Técnicas), Agregados - Determinação da composição granulométrica - Método de ensaio. NBR 17054, Brazil, 2022.

[53] ASTM, Standard Test Method for Sieve Analysis of Fine and Coarse Aggregates 1, West Conshohocken, PA: ASTM., 2017. www.astm.org,.

[54] ABNT (Associação Brasileira de Normas Técnicas), Concreto - Determinação da consistência pelo abatimento do tronco de cone, São Paulo, SP, 2020.

[55] ASTM, Standard Test Method for Compressive Strength of Cylindrical Concrete Specimens, United States, 2021.

[56] ABNT (Associação Brasileira de Normas Técnicas), Cimento Portland - Determinação da resistência à compressão de corpos de prova cilíndricos, Brazil, 2019.

[57] ABNT (Associação Brasileira de Normas Técnicas), Concreto endurecido - Determinação dos módulos de elasticidade e de deformação - Parte 1: Módulos estáticos à compressão, Brazil, 2021.

[58] European Standard (EN), Testing hardened concrete Determination of secant modulus of elasticity in compression, United Kingdom, 2021.

[59] J. Schindelin, I. Arganda-Carreras, E. Frise, V. Kaynig, M. Longair, T. Pietzsch, S. Preibisch, C. Rueden, S. Saalfeld, B. Schmid, J.Y. Tinevez, D.J. White, V. Hartenstein,

K. Eliceiri, P. Tomancak, A. Cardona, Fiji: An open-source platform for biological-image analysis, Nat Methods 9 (2012) 676–682. https://doi.org/10.1038/nmeth.2019.

[60] Elasto Plastic Concrete®, "BarChip 54 – Concrete Fibre Reinforcement", PS54_2021_2 Product Data Sheet (PDS)., 2021. https://barchip.com/wp-content/uploads/2021/07/PDS_BarChip54_web.pdf (accessed April 1, 2023).

[61] Normet Construction Chemicals, "TamFib SP54 – Structural Polymer Macro Fibres for Reinforcing Concrete", V3WW18 – 2018.5.22, Technical Data Sheet., 2018. https://www.normet.com/wp-content/uploads/2019/11/TamFib-SP-TDS-Global-20180524.pdf (accessed April 1, 2023).

[62] Euclid Chemical, "TUF-STRAND™ SF", 03 24 00, Technical Data Sheet., 2023. https://www.euclidchemical.com/fileshare/ProductFiles/TDS/Tuf_Strand_SF.pdf (accessed April 1, 2023).

[63] ZEISS Group, Scout-and-Scan Instrument Control System [Computer program], version 14.0.14829, (2014). https://www.zeiss.com/microscopy/us/l/campaigns/scout-and-scan.html (accessed April 1, 2023).

[64] Object Research Systems (ORS) Inc, Dragonfly 2020.2 [Computer software], (2022). http://www.theobjects.com/dragonfly (accessed April 1, 2023).

[65] X. Wang, S. Shen, G. Shi, Y. Xu, P. Zhang, Iterative non-local means filter for salt and pepper noise removal, J Vis Commun Image Represent 38 (2016) 440–450. https://doi.org/10.1016/j.jvcir.2016.03.024.

[66] A. Bentur, A. Peled, D. Yankelevsky, ENHANCED BONDING OF LOW MODULUS POLYMER FIBERS-CEMENT MATRIX BY MEANS OF CRIMPED GEOMETRY, Cem Concr Res 27 (1997) 1099–1111.

[67] A. Peled, H. Guttman, A. Bentur, Treatments of Polypropylene Fibres to Optimize their Reinforcing Efficiency in Cement Composites, Cem Concr Compos 14 (1992) 277–285.

[68] S. Singh, A. Shukla, R. Brown, Pullout behavior of polypropylene fibers from cementitious matrix, Cement and Conrete Research 34 (2004) 1919–1925.

[69] V.C. Li, Y. Wang, S. Backer, Effect of inclining angle,bundling and surface treatment on synthetic fibre pull-out from a cement matrix, Composites 21 (1990) 132–140.

[70] R. de S. Castoldi, L.M.S. de Souza, F. de Andrade Silva, Comparative study on the mechanical behavior and durability of polypropylene and sisal fiber reinforced

concretes, Constr Build Mater 211 (2019). https://doi.org/10.1016/j.conbuildmat.2019.03.282.

[71] V.M.A. Monteiro, Comportamento Mecânico e Controle de Qualidade do Concreto Projetado com Fibras no Revestimento de Túneis da Mina Cuiabá, Master, Pontifícia Universidade Católica do Rio de Janeiro (PUC-Rio), 2020.

[72] D.Y. Yoo, S.T. Kang, Y.S. Yoon, Effect of fiber length and placement method on flexural behavior, tension-softening curve, and fiber distribution characteristics of UHPFRC, Constr Build Mater 64 (2014) 67–81. https://doi.org/10.1016/j.conbuildmat.2014.04.007.

[73] Z. Lin, V.C. Li, Crack bridging in fiber reinforced cementitious composites with slip-hardening interfaces, J. Mech. Phys. Solids 45 (1997) 763–787.

[74] P.A. Krahl, G. de Miranda Saleme Gidrão, R.B. Neto, R. Carrazedo, Effect of curing age on pullout behavior of aligned and inclined steel fibers embedded in UHPFRC, Constr Build Mater 266 (2021). https://doi.org/10.1016/j.conbuildmat.2020.121188.

[75] J. MacKay, J.F. Trottier, Post-crack creep behavior of steel and synthetic FRC under flexural loading, in: Shotcrete: More Engineering Developments, Taylor & Francis Group, London, 2004: pp. 183–192.

[76] P. Stähli, R. Custer, J.G.M. Van Mier, On flow properties, fibre distribution, fibre orientation and flexural behavior of FRC, Materials and Structures/Materiaux et Constructions 41 (2008) 189–196. https://doi.org/10.1617/s11527-007-9229-x.

[77] H.-C. Wu, V.C. Li, Snubbing and Bundling Effects on Multiple Crack Spacing of Discontinuous Random Fiber-Reinforced Brittle Matrix Composites, Journal of the America Ceramic Society 75 (1992) 3487–3489.

[78] N. Tošić, S. Aidarov, A. La Fuente, Systematic Review on the Creep of Fiber-Reinforced Concrete, Materials 13 (2020). https://doi.org/10.3390/ma13225098.

[79] T. da S. Rocha, D.C.T. Cardoso, L.A.G. Bitencourt, Macro synthetic fiber pullout behavior in short- and long-term tests, Constr Build Mater 384 (2023). https://doi.org/10.1016/j.conbuildmat.2023.131491.

[80] T. Kanda, V.C. Li, Interface property and apparent strength of high-strength hydrophilic fiber in cement matrix, J. Mater. Civ. Eng 10 (1998) 5–13.

[81] F. Deng, C. Cao, L. Xu, Y. Chi, Interfacial bond characteristics of polypropylene fiber in steel/polypropylene blended fiber reinforced cementitious composite, Constr Build Mater 341 (2022) 127897.

[82] P. Di Maida, E. Radi, C. Sciancalepore, F. Bondioli, Pullout behavior of polypropylene macro-synthetic fibers treated with nano-silica, Constr Build Mater 82 (2015) 39–44. https://doi.org/10.1016/j.conbuildmat.2015.02.047.

[83] P. Robins, S. Austin, P. Jones, Pull-out behavior of hooked steel fibres, Materials and Structures/Materiaux et Constructions 35 (2002) 434–442.

[84] Y. Lee, S.T. Kang, J.K. Kim, Pullout behavior of inclined steel fiber in an ultra-high strength cementitious matrix, Constr Build Mater 24 (2010) 2030–2041. https://doi.org/10.1016/j.conbuildmat.2010.03.009.

[85] Y.-S. Tai, S. El-Tawil, High loading-rate pullout behavior of inclined deformed steel fibers embedded in ultra-high performance concrete, Constr Build Mater 148 (2017) 204–218.

[86] Y.Y.Y. Cao, Q.L. Yu, Effect of inclination angle on hooked end steel fiber pullout behavior in ultra-high performance concrete, Compos Struct 201 (2018) 151–160. https://d0i.0rg/l0.1016/j.compstruct.2018.06.029.

[87] R. Zhang, X. Yan, L. Guo, Pullout damage analysis of steel fiber with various inclination angles and interface states in UHPC through acoustic emission and microscopic observation, Journal of Building Engineering 51 (2022). https://doi.org/10.1016/jjobe.2022.104271.

[88] A. Abrishambaf, J.A.O. Barros, V.M.C.F. Cunha, C. Frazão, Time dependent behavior of fibre pull-out in self-compacting concrete, Cem Concr Compos 77 (2017) 14–28. https://doi.org/10.1016/j.cemconcomp.2016.12.004.

[89] R.J. Gray, Experimental techniques for measuring fibre/matrix interfacial bond shear strength, 1983.

[90] A.E. Naaman, G.G. Namur, J.M. Alwan, H.S. Najm, Fiber Pullout and Bond Slip. I: Analytical Study, Journal of Structural Engineering 117 (1991) 2769–2790. https://doi.org/10.1061/(ASCE)0733-9445(1991)117:9(2769).

[91] H.L. Cox, The elasticity and strength of paper and other fibrous materials, British Journal of Applied Physics 3 (1952) 72–79. https://doi.org/10.1088/0508-3443/3/3/302.

[92] X.B. Zhang, H. Aljewifi, J. Li, Failure Mechanism Investigation of Continuous Fibre Reinforced Cementitious Composites by Pull-out Behaviour Analysis, Procedia Materials Science 3 (2014) 1377–1382. https://doi.org/10.1016/j.mspro.2014.06.222.

[93] X.B. Zhang, H. Aljewifib, J. Lic, Construction and Building Materials 47 (2013) 456-464 • • 3m Failure behaviour investigation of continuous yarn reinforced cementitious composites, 2013.

[94] V.C. Li, H. Stang, Interface Property Characterization and Strengthening Mechanisms in Fiber Reinforced Cement Based Composites, 1997.

[95] ASTM C1557-20, Standard Test Method for Tensile Strength and Young's Modulus of Fibers, (2020).

[96] A. Gopanna, R.N. Mandapati, S.P. Thomas, K. Rajan, M. Chavali, Fourier transform infrared spectroscopy (FTIR), Raman spectroscopy and wide-angle X-ray scattering (WAXS) of polypropylene (PP)/cyclic olefin copolymer (COC) blends for qualitative and quantitative analysis, Polymer Bulletin 76 (2019) 4259–4274. https://doi.org/10.1007/s00289-018-2599-0.

[97] R. Caban, FTIR-ATR spectroscopic, thermal and microstructural studies on polypropylene-glass fiber composites, J Mol Struct 1264 (2022).

[98] M.R. Jung, F.D. Horgen, S. V. Orski, V. Rodriguez C., K.L. Beers, G.H. Balazs, T.T. Jones, T.M. Work, K.C. Brignac, S.J. Royer, K.D. Hyrenbach, B.A. Jensen, J.M. Lynch, Validation of ATR FT-IR to identify polymers of plastic marine debris, including those ingested by marine organisms, Mar Pollut Bull 127 (2018) 704–716. https://doi.org/10.1016/j.marpolbul.2017.12.061.

[99] M.A. Peltzer, Catherine. Simoneau, Report of an inter-laboratory comparison from the European Reference Laboratory for Food Contact Materials : ILC 002 2013 : identification of polymeric materials., Publications Office, Italy, 2013.

[100] J. Fang, L. Zhang, D. Sutton, X. Wang, T. Lin, Needleless melt-electrospinning of polypropylene nanofibres, J Nanomater 2012 (2012). https://doi.org/10.1155/2012/382639.